ANIMAL CELL

thin section of a generalized animal cell

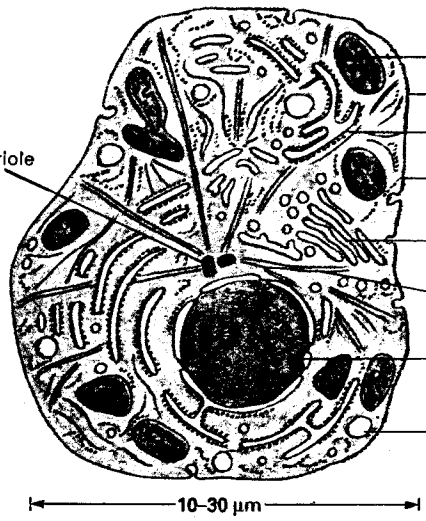

mitochondria
plasma membrane
endoplasmic reticulum
cytosol
Golgi apparatus
filamentous cytoskeleton
nucleus
lysosomes peroxisomes

10–30 μm

PLANT CELL

thin section of a generalized cell from a higher plant

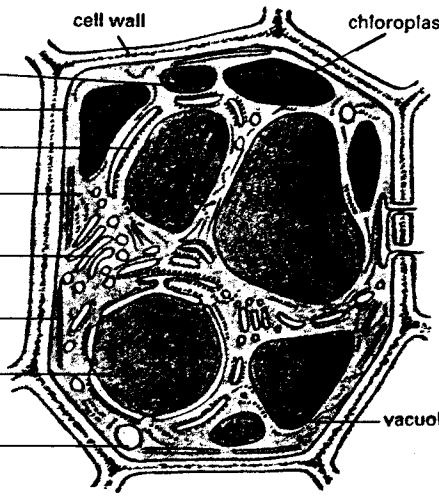

10–100 μm

THE MEMBRANE SYSTEM OF THE CELL

PLASMA MEMBRANE

The outer boundary of the cell is the plasma membrane, a continuous sheet of phospholipid molecules about 4–5 nm thick in which various proteins are embedded.

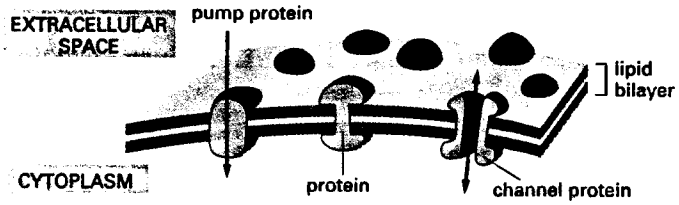

Some of these proteins serve as pumps and channels for transporting specific molecules into and out of the cell.

ENDOPLASMIC RETICULUM

Flattened sheets, sacs, and tubes of membrane extend throu the cytoplasm of eucaryotic cells, enclosing a large intracellu space. The ER membrane is in structural continuity with the outer membrane of the nuclear envelope, and it specializes i synthesis and transport of lipids and membrane proteins.

The rough endoplasmic reticulum (rough ER) generally occu flattened sheets and is studded on its outer face with riboso engaged in protein synthesis.

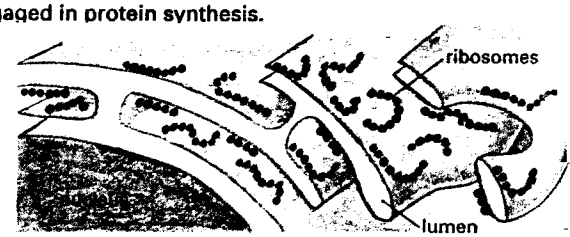

The smooth endoplasmic reticulum (smooth ER) is generally more tubular and lacks attached ribosomes. It has a major function in lipid metabolism.

GOLGI APPARATUS

A system of stacked, membrane-bounded, flattened sacs involved in modifying, sorting, and packaging macromolecules for secretion or for delivery to other organelles.

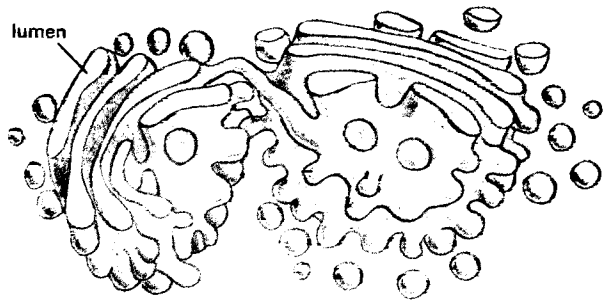

Around the Golgi apparatus are numerous small membrane-bounded vesicles (50 nm and larger) that carry material between the Golgi apparatus and different compartments of the cell.

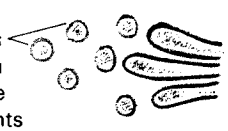

LYSOSOMES

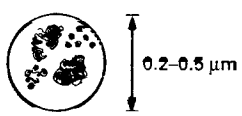

membrane-bounded vesicles that contain hydrolytic enzymes involved in intracellular digestions

PEROXISOMES

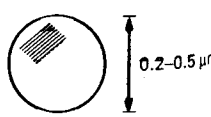

membrane-bounded vesicle containing oxidative enzym that generate and destroy hydrogen peroxide

18 Panel 1–1 Eucaryotic cells: a survey of their principal organelles.

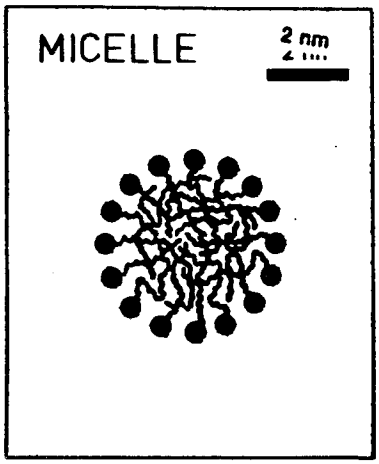
MICELLE
2 nm

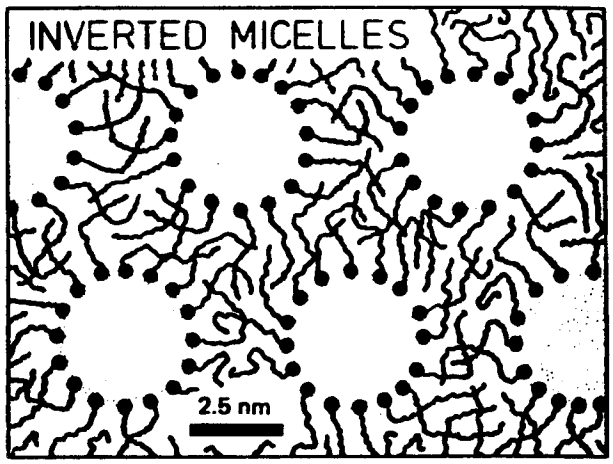
INVERTED MICELLES
2.5 nm

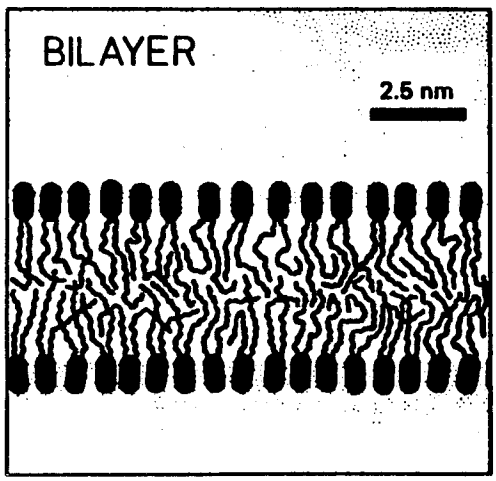
BILAYER
2.5 nm

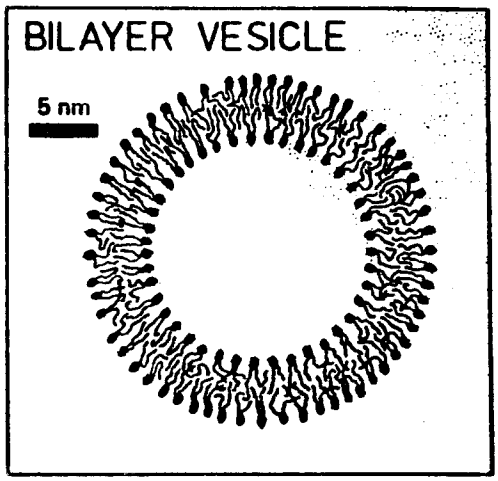
BILAYER VESICLE
5 nm

Energetics of Phospholipid Self-Assembly

Cylindrical Micelles

What is the driving force for phospholipid self-assembly?

! Spontaneous self-assembly is NOT driven by attraction between phospholipid molecules !

Energy Units

$k_B T_{room} = 1.38 \times 10^{-16}(300) = 4 \times 10^{-4}$ erg $= 4 \times 10^{-24}$ kJ

(physicist) (chemist)

$\therefore$ 1 kJ/mole $= 1.04 \times 10^{-2}$ eV/part $= 1.6 \times 10^{-14}$ erg $= 0.4 k_B T$

In these units

Covalent bonds	C-C	140 $k_B T$
	C=C	244 $k_B T$
VdW bond	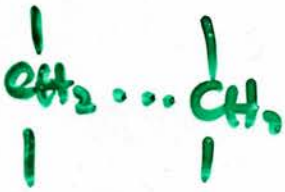	3 $k_B T$
trans/gauche		5 $k_B T$
hydrogen bond		8 - 11 $k_B T$

- water - water
- water - polar
- NOT water - hydrocarbon

local order in H_2O max. H-bonding contacts

Phospholipid self assembly → soft, flexible, fluid-like structures

Forces that hold amphiphilic molecules together

are NOT due to strong covalent
ionic bonds

but are due to much weaker

VdW
hydrophobic interactions
hydrogen-bonding
screened electrostatic interactions

Environmental changes

eg. pH
electrolyte conc

→ affect intermolecular forces b/w aggregates
→ Δ size, shape of assembly
→ Δ aggregate interactions

"Hydrophobic effect" as the Main Driving Force.

Let's look at the entropic contributions to the "hydrophobic effect"

$F = E - TS$ Obj: min free energy

Free energy can be min. in 2 ways:

① ↑ binding (↓ E)
typically dominates in solids

② ↑ accessible configs. (↑ S)
typically dominates in fluids

Entropic Picture:
When water sits next to an (interface) hydrophobic environment

→ partial freezing occurs due to immobilization
→ ↓ in entropy
→ incur free energy cost / area

* water structure @ heat interfaces
See Y.R. Shen; K. Eisenthal

Why is it more immobilizing to sit next to hydrocarbons than next to polar groups (heads)?

∃ more free energy cost for water/hydrocarbon than water/heads interface

When water sits against another material, the local order is reduced, compared that to the bulk,

→ less bonding

→ again incur energy cost/unit area

this is on top of the entropic effects!

$\sigma_{water/air} = 70 \, erg/cm^2 \sim 0.2 \, k_BT/Å^2$ (30°C)

$\sigma_{water/oil} \sim 30 \, erg/cm^2 \sim 0.07 \, k_BT/Å^2$

use this to do some back of the envelop calculations & get a few of the order of mag. of forces at hand

A single phospholipid molecule is very insoluble !

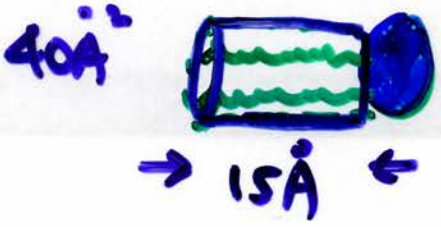

Hydrophobic area/molecule
$\simeq 300 Å^2$

Energy cost in exposing tail portion to water

$\sim 300 Å^2 (0.07 k_BT/Å^2)$

$\sim 21 k_BT$/molecule

i.e. expect factor $e^{-\Delta E/k_BT}$ in solubility

$\Rightarrow$ monomeric concentration of order

$e^{-21} \sim$ 10^{-10} M dan for typical phospholipid

This forces phospholipid in water to aggregate in such a way as to shield tails from hydrophobic exposure to water

One way to do this is to form a bilayer

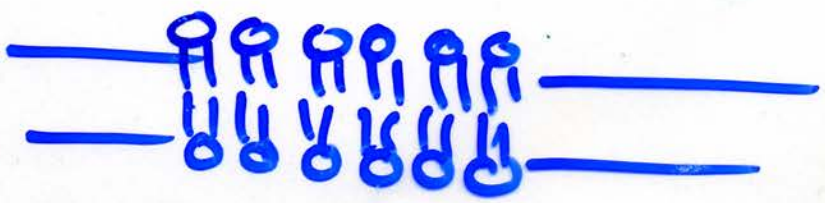

* will discuss the exact shape formed later & the constraints for diff. structures

Flip Flop

Once a bilayer is formed, it's very difficult to switch a phospholipid molecule from one side to the other (unless there are edges/pores)

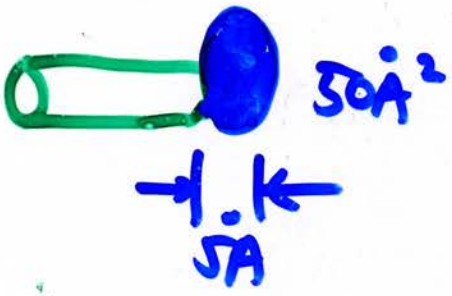

Area of head group
$\sim 175 Å^2$

Energy cost in exposing head group to hydrocarbon
$\sim 175 Å^2 (0.07\ k_BT/Å^2)$
$\sim 12\ k_BT$

By contrast, the energy cost of putting a single water molecule into the bilayer interior is roughly

$$A \sim 4\pi (1Å)^2 \sim 12 Å^2$$

$$\Delta E \sim 12 Å^2 (0.07\ k_BT/Å^2) \sim k_BT$$

∴ water passes readily thru' membrane

Cholesterol can also flip flop quite freely

Edges of bilayer cost hydrophobic energy

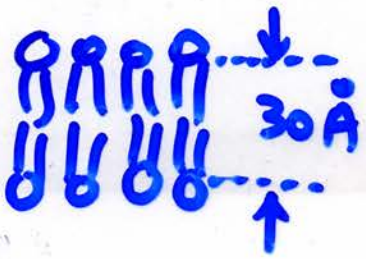

Edge Energy / length

= 30Å (0.07 kBT/Å²)

≈ 2 kBT/Å

$$\lambda_{edge} = 8 \times 10^{-6} \text{ erg/cm}$$

This provides the "force" which acts to make bilayer sheets assemble into closed or vesicular type of structures.

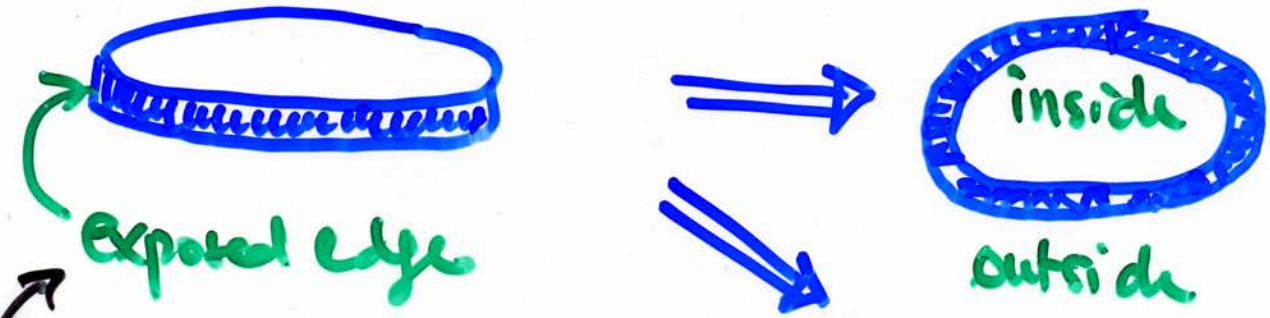

other topologies

* However, if you can stabilize the edge with other surfactant

→ can form stable bicelle structures

→ used in NMR as a lipid mimicking environment.

What happens when you start w/ pure water and slowly add lipid into it?

WATER-AMPHIPHILE AGGREGATION PHENOMENA

"Lyotropic Phases"

Generic Amphiphile-water structures

Single molecule

- only @ low conc. 10^{-10} M

Small n complexes

- anything which shields hydrocarbons from exp. to aqueous environment

micelles

- may or may not be spherical
- relative size of head/tail
- new length scale

micellar colloidal

- micellar crystals
- micellar liquid crystals

hexagonal (H) other liner phases

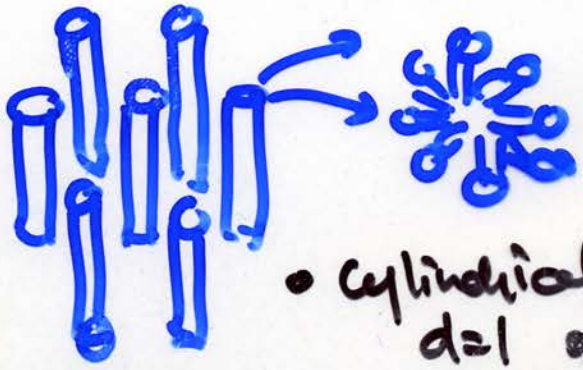

- cylindrical micelle dal objects

lamellar (L)

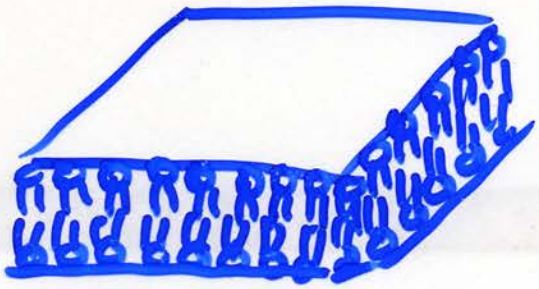

- d = 2 objects

Cubic (Q)

- hex or lamellar
- d = 3 crystalline structure
- Plumber's nightmare

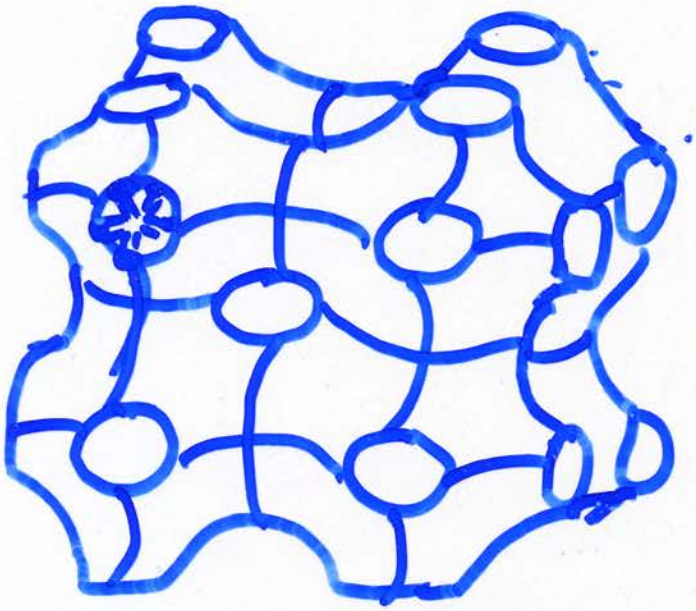

"monolayer"
"micellar"
"linear"

tubes must be narrow for monolayer phases

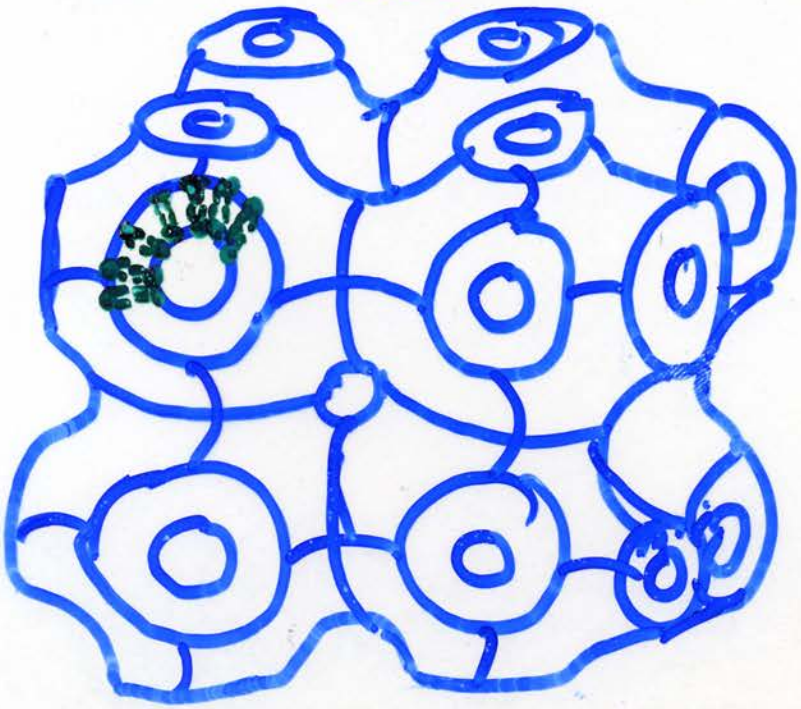

"bilayer"
"bicontinuous"

some cubic (bicontinuous) phases have been seen in biology

Plus:

- inverted versions of all the above

micelles → inverted micelles

hexagonal (H) → inverted hexagonal (H_2)

- disordered versions of all the above

hex → spaghetti

lamellar cubic → sponge

micellar crystal → micellar fluid

* Read more about cubic phases

see Sol Gruner's work

Phase Diagrams

Phospholipid phase diagrams remain incompletely known

Basic sequences of phases determined by geometrically packing constraints
preferred monolayer curvature

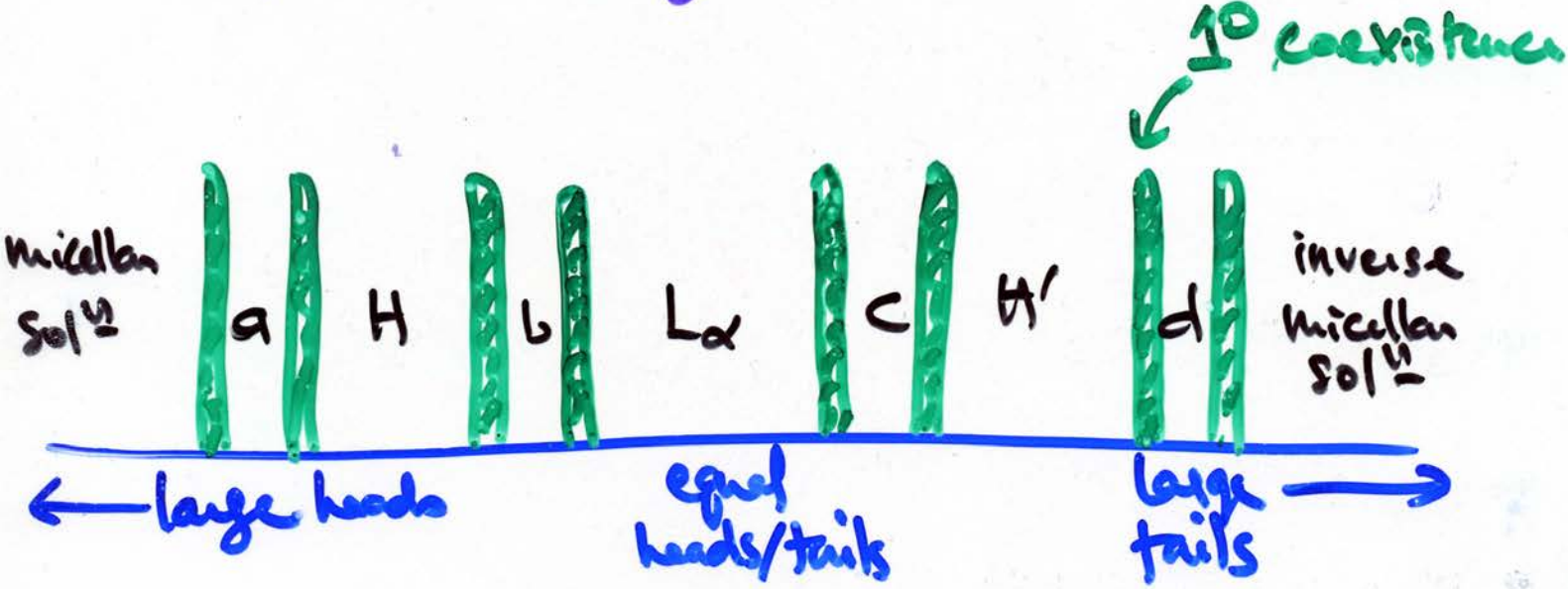

The intermediate phases a, b, c, d are typically (but not always) cubic

a = packed micelles (or monolayer cubic)

b, c = bilayer cubic, bicontinuous, sponge

d = packed inverse micelles (or monolayer cubic)

These geometrical sequences show up in phase diagrams but are often cut off

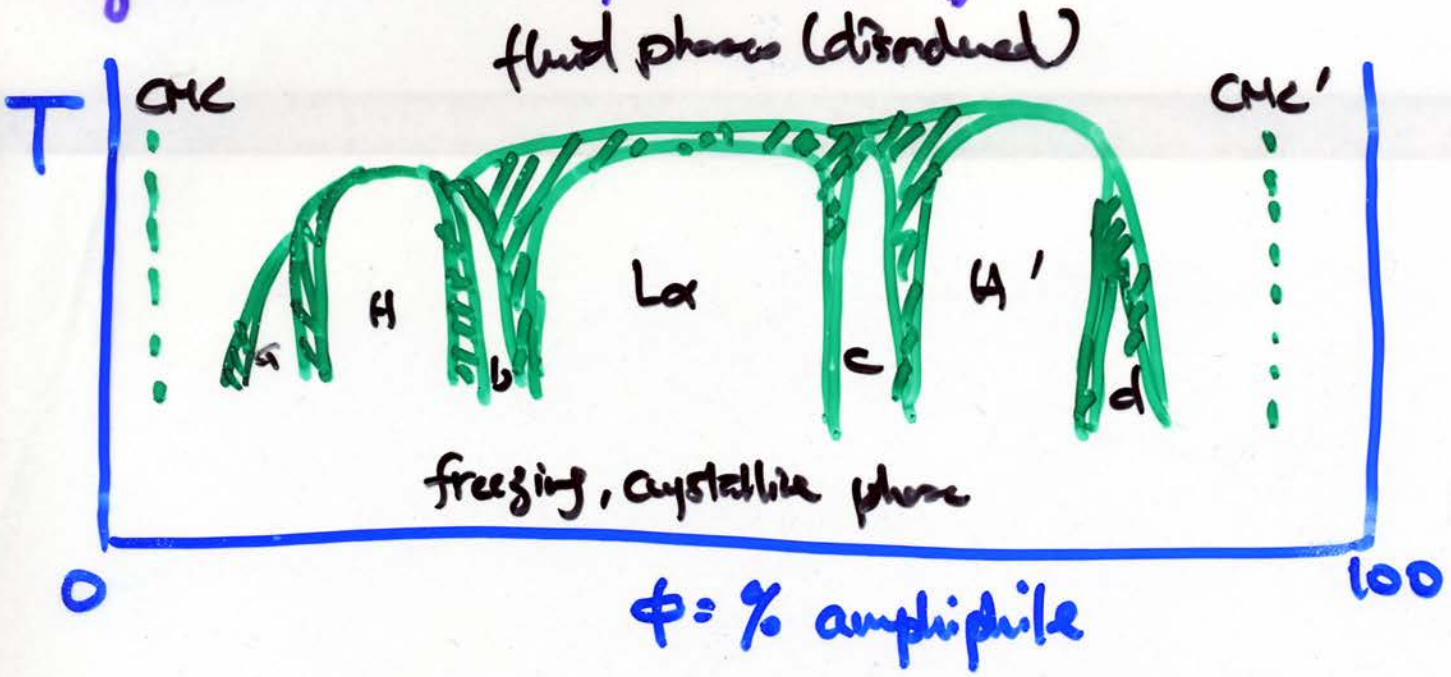

- CMC = critical micelle conc.
  when do micelles first form?
  (not a sharp line)
  10^{-10} M for phospholipids
- 1° coexistence (almost always)
  but it may be narrow
- Bulk amphiphile phase may be lamellar
- Phase separation % water-rich & amphiphile-rich may be found
- Knowledge on phase diagram → rather poor active area of research

* Phospholipids Handbook, ed. Cevc (Dekker, NY, 93)
* Chem & Physics of Lipids 57 (1990) special issue
57

Thermodynamics of Self-Assembly

Tanford C. (1973, 1980) The Hydrophobic Effect
Wiley, NY

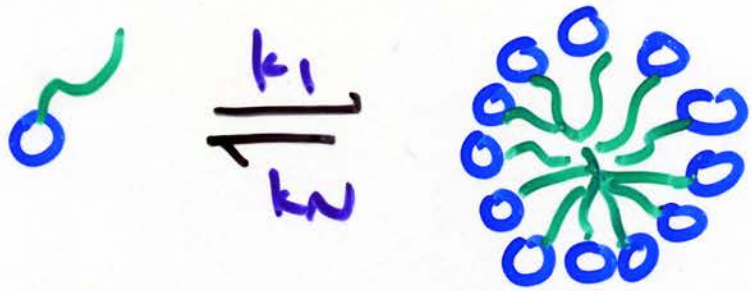

Number	N=1	N
Activity	X_1	X_N
Chemical potential	μ_1	μ_N

μ for all identical molecules in diff aggs. have to be the same @ equil

$$\mu = \mu_1 = \mu_1^\circ + kT \log X_1 \quad \text{monomer}$$

$$= \mu_2 = \mu_2^\circ + \frac{kT}{2} \log \frac{X_2}{2} \quad \text{dimer}$$

$$= \mu_3 = \mu_3^\circ + \frac{kT}{3} \log \frac{X_3}{3} \quad \text{trimer}$$

$$\vdots$$

$$= \mu_N = \mu_N^\circ + \frac{kT}{N} \log \frac{X_N}{N} \quad \text{N-mer}$$

mean chem. potential → μ_N

μ_N° mean intrinsic free energy per molecule

Rate of association $= k_1 X_1^N$

Rate of dissociation $= k_N \left(\frac{X_N}{N}\right)$

At equil,

Rate of associate = Rate of dissociation

$$k_1 X_1^N = k_N \left(\frac{X_N}{N}\right)$$

∴ Equil const.

$$K = \frac{k_1}{k_N}$$

$$= \left(\frac{X_N}{N}\right) \frac{1}{X_1^N}$$

But $X_N = N \exp\left[\frac{N}{kT}(\mu - \mu_N^\circ)\right]$

$$X_1 = \exp\left[\frac{1}{kT}(\mu - \mu_1^\circ)\right]$$

$$\therefore K = \frac{\exp[N(\mu - \mu_N^\circ)/kT]}{\exp[N(\mu - \mu_1^\circ)/kT]}$$

$$= \exp[-N(\mu_N^\circ - \mu_1^\circ)/kT]$$

For an M- and N-aggregates, we can write down their chem. potential @ equil

$$\mu_M^\circ + \frac{kT}{M}\log\frac{x_M}{M} = \mu_N^\circ + \frac{kT}{N}\log\frac{x_N}{N}$$

$$M\mu_M^\circ + kT\log\frac{x_M}{M} = M\mu_N^\circ + \frac{M}{N}kT\log\frac{x_N}{N}$$

$$M(\mu_M^\circ - \mu_N^\circ) + kT\log\frac{x_M}{M} = \frac{M}{N}kT\log\frac{x_N}{N}$$

$$\frac{x_M}{M}\exp[M(\mu_M^\circ - \mu_N^\circ)/kT] = \left(\frac{x_N}{N}\right)^{\frac{M}{N}}$$

$$\therefore x_N = N\left\{\frac{x_M}{M}\exp[M(\mu_M^\circ - \mu_N^\circ)/kT]\right\}^{\frac{N}{M}}$$

For $M=1$

$$x_N = N\{x_1\exp[(\mu_1^\circ - \mu_N^\circ)/kT]\}^N$$

Conservation of materials

$$C = x_1 + x_2 + \ldots = \sum_{N=1}^{\infty} x_N$$

Together, these eq^{n}s completely define the sys.

Note:

C – conc. } dimensionless
X_N – activity } vol fraction or mol fraction

Neither can be greater than 1

Dilute limit – interaggregate interactions ignored

Conditions Necessary for the Formation of Aggregates

- $\exists$ a diff. in cohesive energies b/w molecules in agg. & monomer state
- If molecule in diff-sized agg. experiences the same interaction

$$X_N = N X_1^N \quad \text{for } \mu_1^\circ = \mu_2^\circ = \cdots = \mu_N^\circ$$

since $X_1 < 1$, $X_N \ll 1$ } This implies most will stay as monomers.

For aggregation to take place

$$\boxed{\mu_N^\circ < \mu_1^\circ}$$

Possibilities:
① $\mu_N^\circ \downarrow$ as $N \uparrow$
② μ_N° has a min.

Variation of μ_N° with N for Diff. Geometries

① 1-D aggregates (rods)

bond energy $= \alpha kT$

For a N-mer, total interaction energy

$$N\mu_N^\circ = -(N-1)\alpha kT$$

$$\mu_N^\circ = -\left(1-\frac{1}{N}\right)\alpha kT$$

$$= -\alpha kT + \alpha kT/N$$

$$\boxed{\mu_N^\circ = +\mu_\infty^\circ + \frac{\alpha kT}{N}}$$

μ_∞°: bulk energy in an infinite aggregate

$\lim_{N\to\infty} \mu_N^\circ = \mu_\infty^\circ$

Similar expression can be obtained for rod-like micelle

② 2-D aggregates (discs, sheets)

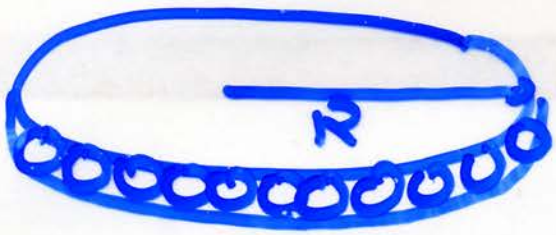

$N \propto \pi R^2$

unbound molecules @ rim

$\propto 2\pi R$

$\propto N^{1/2}$

$$\therefore \mu_N^\circ = \mu_\infty^\circ + \frac{\alpha kT}{N^{1/2}}$$

③ 3-D aggregates (spheres)

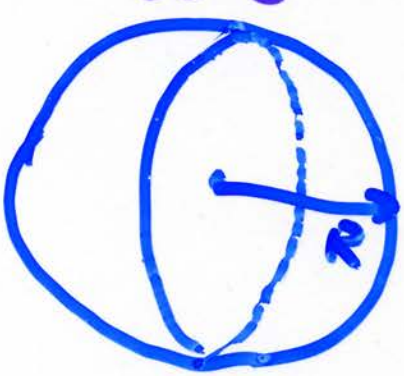

$N \propto \frac{4}{3}\pi R^3$

unbound molecules @ surface

$\propto 4\pi R^2$

$\propto N^{2/3}$

$$\therefore \mu_N^\circ = \mu_\infty^\circ + \frac{\alpha kT}{N^{1/3}}$$

For a spherical aggregate of radius R made up of monomers of volume V

e.g. alkanes in H_2O

$$N = \left(\frac{4}{3}\pi R^3\right)\left(\frac{1}{V}\right)$$

Free energy $= N\mu_\infty^\circ + 4\pi R^2\sigma$

σ ↑ interfacial tension energy / area

$$\therefore \mu_N^\circ = \mu_\infty^\circ + \frac{4\pi R^2\sigma}{N}$$

$$= \mu_\infty^\circ + \frac{4\pi\sigma\left(N\frac{3V}{4\pi}\right)^{2/3}}{N}$$

$$= \mu_\infty^\circ + \frac{4\pi\sigma\left(3V/4\pi\right)^{2/3}}{N^{1/3}}$$

$$= \mu_\infty^\circ + \frac{\alpha kT}{N^{1/3}}$$

$$\alpha kT = 4\pi\sigma\left(\frac{3V}{4\pi}\right)^{2/3}$$

$$\alpha = \frac{4\pi\sigma\left(3V/4\pi\right)^{2/3}}{kT}$$

$$\boxed{\alpha = \frac{4\pi r^2\sigma}{kT}}$$

$r = \left(\frac{3V}{4\pi}\right)^{1/3}$ = effective radius

$\alpha > 0$

dep. on the strength of the intermolecular interaction

In general, the interaction energy of the molecule for the simple structure

$$\mu_N^0 = \mu_\infty^0 + \frac{\alpha kT}{NP}$$

P – dep. on the shape or dimensionality of the aggregates

?? What determines when aggregates form ??

Critical Micelle Concentration (CMC)

$$X_N = N\{X_1 \exp[(\mu_1^\circ - \mu_N^\circ)/kT]\}^N$$

$$= N\{X_1 \exp[(\alpha kT - \frac{\alpha kT}{N^p})/kT]\}^N$$

$$= N\{X_1 \exp[(1 - \frac{1}{N^p})\alpha]\}^N$$

$$\cong N[X_1 e^\alpha]^N$$

For low conc X_1 s.t. $X_1 e^\alpha << 1$

$X_1 > X_2 > X_3$ for all α

→ isolated monomers : the preferred state

→ $X_1 \cong C$

As $X_1 e^\alpha \longrightarrow 1$ or $X_1 \longrightarrow e^{-\alpha}$

it cannot ↑ anymore !! X_N has to be < 1

$(X_1)_{crit}$ = critical micelle conc.

= critical aggregation conc.

$X_1 > (X_1)_{crit.}$ → micelles formation.

$$CMC = \exp[-(\mu_1^\circ - \mu_N^\circ)/kT] = e^{-\alpha} \text{ for all } p$$

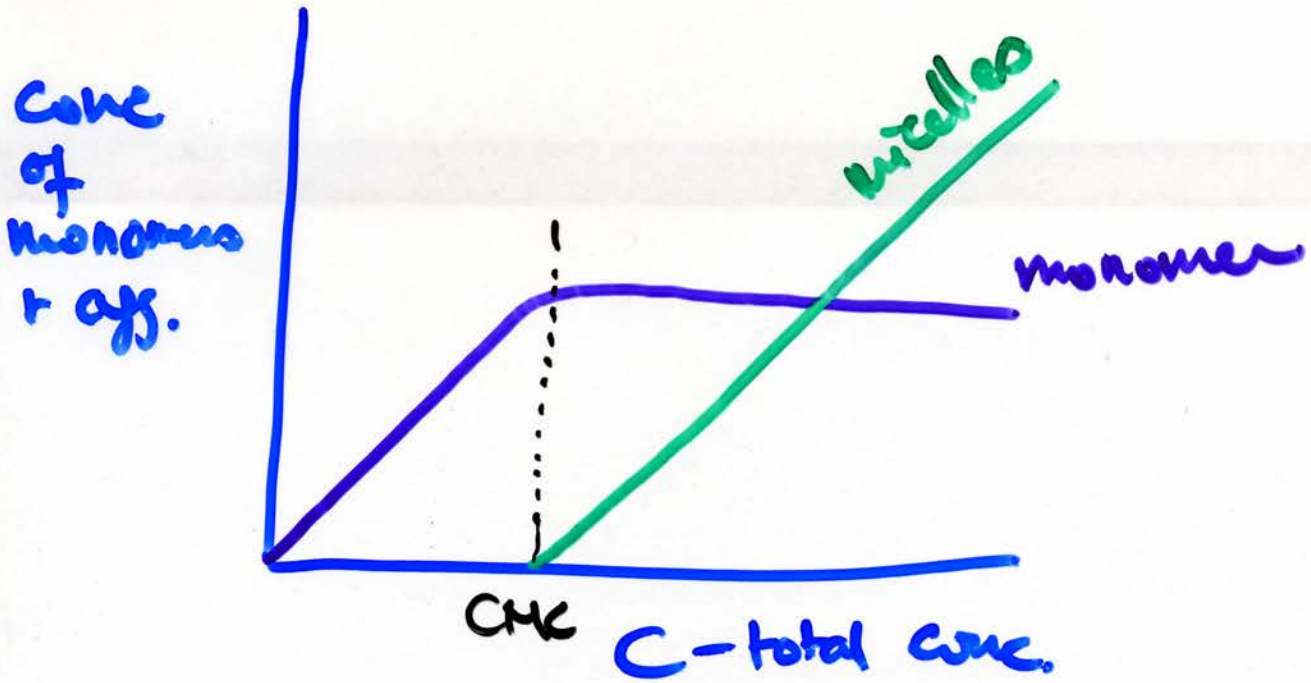

How many monomers in a micelle?

Exact # dep. on length of hydrocarbon chain

$RN(CH_3)_2^+ CH_2COO^-$

# of C in R	N in aggregate
8	24
⋮	⋮
15	130

Geometric Packing Considerations

Depends on

① Optimal area, a_o

② Vol. of hydrocarbon chains, V

③ max effective chain length, l_c
(for fluid, incomp. state)

l_c

$$l_c \leq l_{max}$$

$$\simeq (0.154 + 0.126\,n)\ nm$$

V

$$V \simeq (27.4 + 26.9\,n) \times 10^{-3}\ nm^3$$

For large n

$$\frac{V}{l_c} \simeq 0.21\ nm^2$$

$\simeq$ min X-sectional area of a hydrocarbon chain

If ①, ② & ③ are known, structure formed can be determined.

For same a°, μ_i roughly the same for diff. structures

Entropy will favor the structure ∋ smallest agg. # (N=M)

Larger structure → entropically unfavorable

Smaller structure → force $a > a_o$
energetically unfavorable

Packing parameter a Shape factor.

$$\frac{V}{a_o l_c}$$

determines the structure formed

Spherical Micelles

$$M = \frac{4\pi R^2}{a_0}$$

but $V = \frac{a_0 R}{3}$

$$M = \frac{4\pi R^3}{3V}$$

$$\frac{4\pi R^2}{a_0} \cdot \frac{3V}{4\pi R^3} = 1 \quad \text{max.}$$

$$\therefore \frac{V}{a_0 R} = \frac{1}{3}$$

$$\therefore \boxed{\frac{V}{a_0 l_c} < \frac{1}{3}} \qquad l_c < R$$

eg. Sodium dodecyl sulphate (SDS)

exp. $M = 74$; $n = 12$

$\therefore V = (27.4 + 26.9 \times 12) \times 10^{-3} = 0.3502\ nm^3$

$a_0 = 0.57\ nm^3$

$R = 1.84\ nm.$

But $l_c = 1.67\ nm$

$\rightarrow \frac{V}{a_0 l_c} \leq 0.37 \rightarrow$ non-spherical micelles.

Cylindrical Micelles

$$\frac{1}{3} < \frac{v}{a_0 l_c} < \frac{1}{2}$$

eg. addⁿ of salt, screening headgroup repulsion (or w/ smaller headgroups)

Already shown ($p=1$)

* large
* polydisperse
* agg # $\propto \sqrt{C}$

Special prop. due to 'end effects'

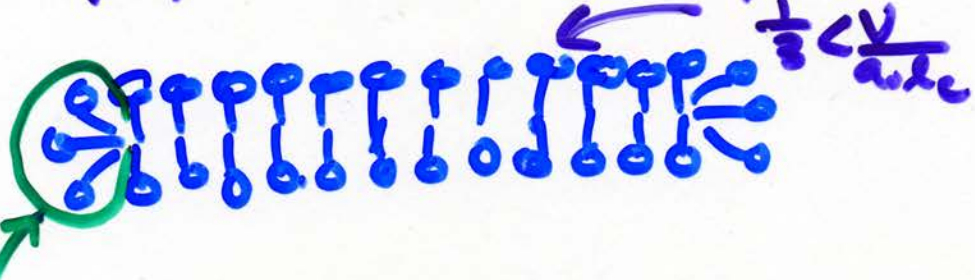

$\frac{v}{a_0 l_c} = \frac{1}{3} \rightarrow a_{cap} > a_0$

unfavorable cap configuration

determines mag. of interaction param α

eg. $\alpha \uparrow$ as $a_0 \downarrow$

Recall $\langle N \rangle = 2\sqrt{Ce^{\alpha}}$

Changes w T, pH, ionic strength

eg. SDS in 0.6 M NaCl agg # ~ 1000

in water agg # ~ 60

Bilayers

$$\frac{V}{a_0 l_c} \sim 1$$

Same a_0 & l_c, V has to double for this requirement to hold

→ bilayers usu. formed w/ lipids that have 2 tails.

Chain doubling affects agg. properties, both static & dynamic

① ↓ CMC (∵ ↑ hydrophobicity)

Micelles $10^{-2} \sim 10^{-5}$ M

Bilayers $10^{-6} - 10^{-10}$ M

② ↑ residence time, τ_R, of in agg.

related to activation energy, ΔE, for molecules to escape from agg. to bulk.

with $\tau_0 \equiv$ collision time

$$\text{Prob} \propto e^{-\Delta E/kT}$$

$$\tau_R = \frac{\tau_0}{e^{-\Delta E/kT}} \qquad \Delta E = (\mu_i^0 - \mu_{\infty}^0)$$

$$\simeq \tau_0 \frac{kT}{CMC}$$

90 τ_R(micelle) ~ 10^{-4} s ; τ_R(bilayers) ~ 10^{+4} s

CMC des ↓ chain length.

exchange rate for each addit^{n} of 2 CH_2 groups (to double tail) → ↓ 4-10 ×

③ Flip-flip - diffusive exchange

$$\tau_{ff} \sim 10^{2} - 10^{5}\ s$$

Vesicles

Formation of closed spherical structures

① eliminates edge energy for disk-like structures

② Entropically favorable

finite vs. infinite agg. #

As long as min area can be maintained

→ vesicles are the preferred structure

$$\frac{1}{2} < \frac{V}{a_0 l_c} < 1$$

Formation of a curved surface leads to truncated cone geometry

Critical radius

$$R_c \simeq l_c \left[\frac{3 + \sqrt{3(4V/a_0 l_c - 1)}}{6(1 - V/a_0 l_c)} \right]$$

$$\simeq \frac{l_c}{(1 - V/a_0 l_c)}$$

Smallest radius of curvature forcing headgroup area a in outer monolayer to exceed a_0

$R < R_c$ outer $a > a_0$

$R > R_c$ entropically unfavorable

At R_c

$$\text{bilayer thickness} \simeq \frac{2V}{a_0} = t$$

$$\text{agg. \# } N \simeq 4\pi [R_c^2 + (R_c - t)^2]/a_0$$

Reg. agg Pc $a_0 \simeq 0.717\,nm^2$

$V \simeq 1.063\,nm^3$

$l_c \simeq 1.75\,nm$

$R_c \simeq 11\,nm$

$N \simeq 3000$

$t \simeq 3.0\,nm$

$\therefore \frac{V}{a_0 l_c} \simeq 0.85 \rightarrow$ vesicle

Inverted Structures

$$\frac{v}{a_0 l_c} > 1$$

small optimal area

bulky polyunsaturated chains (large v, small l_c)

$$K_c \simeq \frac{l_c}{1 - v/a_0 l_c}$$

$$< 0$$

inverted structures resulted.

Factors Affecting Changes from One Structure to Another

① Headgroup

Small head → large vesicle
less-curved bilayers
inverted micellar

↓ effective head size (anions) → Ca^{2+}
pH ↓

② Chains

branching → ↓ lc, ↑ V
→ large vesicles
inverted structures

③ Temperature

T↑ → trans-gauche isomerizat^{n}.
↓ lc
→ ↑ V/a$_o$lc

T↑ → can Δ a$_o$ too
Usu. a$_o$↑ (more hydrophilic heads)
→ ↓ V/a$_o$lc

Nonionic micelles → grow
Ionic " → shrink
Zwitterion " → × Δ ε T.

TABLE 17.2 Mean (dynamic) packing shapes of lipids and the structures they form

Lipid	Critical packing parameter $v/a_0 l_c$	Critical packing shape	Structures formed
Single-chained lipids (surfactants) with large head-group areas: *SDS in low salt*	< 1/3	Cone 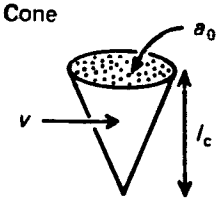	Spherical micelles 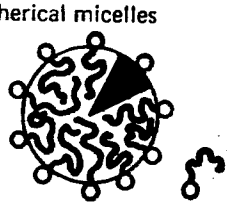
Single-chained lipids with small head-group areas: *SDS and CTAB in high salt, nonionic lipids*	1/3-1/2	Truncated cone 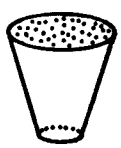	Cylindrical micelles 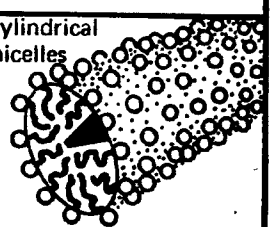
Double-chained lipids with large head-group areas, fluid chains: *Phosphatidyl choline (lecithin), phosphatidyl serine, phosphatidyl glycerol, phosphatidyl inositol, phosphatidic acid, sphingomyelin, DGDG[a], dihexadecyl phosphate, dialkyl dimethyl ammonium salts*	1/2-1	Truncated cone 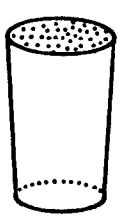	Flexible bilayers, vesicles 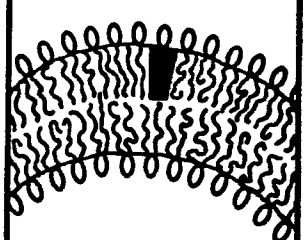
Double-chained lipids with small head-group areas, anionic lipids in high salt, saturated frozen chains: *phosphatidyl ethanolamine, phosphatidyl serine + Ca^{2+}*	~1	Cylinder 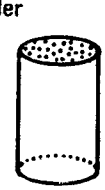	Planar bilayers 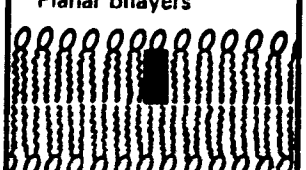
Double-chained lipids with small head-group areas, nonionic lipids, poly *(cis)* unsaturated chains, high T: *unsat. phosphatidyl ethanolamine, cardiolipin + Ca^{2+} phosphatidic acid + Ca^{2+} cholesterol, MGDG[b]*	> 1	Inverted truncated cone or wedge 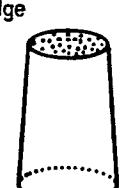	Inverted micelles 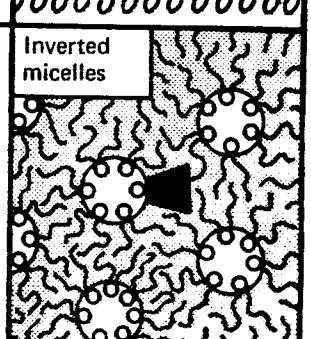

[a] DGDG, digalactosyl diglyceride, diglucosyl diglyceride.
[b] MGDG, monogalactosyl diglyceride, monoglucosyl diglyceride.

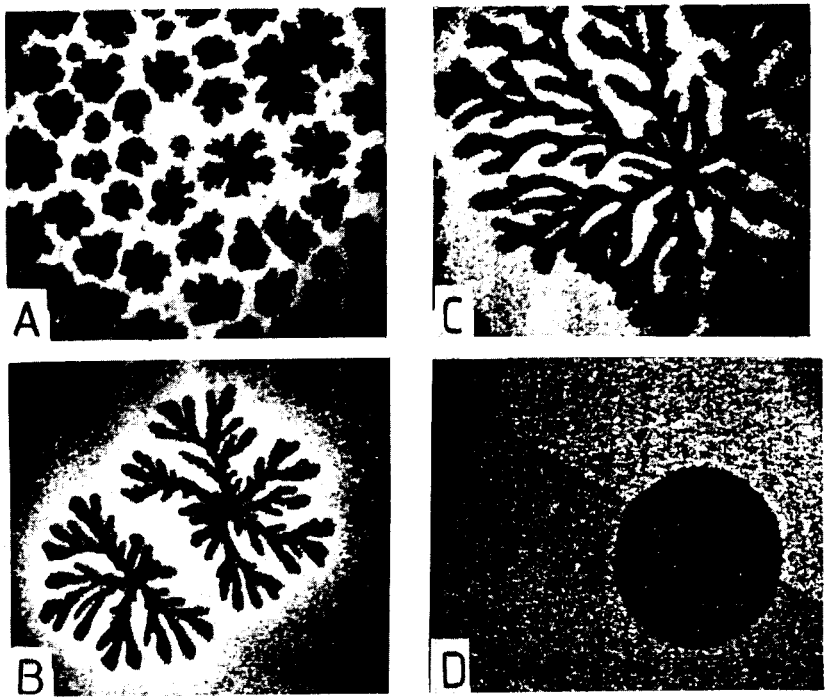

Fig. IV-38. Morphology of crystalline L-α-dimyristoylphosphatidylethanolamine domains following a π-jump to the plateau region of the π–σ plot: (*a*) after 2 sec; (*b*) after 1 min; (*c* after 20 min; (*d*) following a second pressure jump after condition (*c*). (From Ref. 281.)

Remarkable, chiral patterns are seen if about 2% cholesterol is present in a monolayer of *S*-dipalmitoylphosphatidylchlorine and the film is compressed to the plateau region (e.g., as in Fig. IV-37). One such pattern is shown in Fig. IV-39 (284). The behavior has been modeled theoretically in terms of a line tension between the crystalline and liquid phases (284).

Other lipid-containing systems that have been studied include mixed films of dioleylphosphatidylcholine with retinal (285) and with cytochrome *c* (including surface potential and ellipsometric measurements) (286) and of lipid films with porphyrins (fluorescence studies) (287). Monolayer studies have also been reported on other membrane constituents such as valine–gramiciden A and Valinomycin (288). Finally, a bridged porphyrin, mesoporphyrin II, a somewhat spherical molecule, showed monolayer π–σ behavior surprisingly like that of the long-chain fatty acids (289).

C. Films at the Oil–Water Interface

As has been noted, much of the interest in films of proteins, steroids, lipids, and so on, has a biological background. While studies at the air–water

Fig. IV-39. Epifluorescence photomicrograph of crystalline domains of a dipalmitoylphosphatidylcholine monolayer containing 2% cholesterol and co pressed to the plateau region. From H. M. McConnell, D. Keller, and H. Gaub. *Phys. Chem.*, **90**, 1717 (1986) (Ref. 284). Copyright 1986, American Chemical Sc ety.

interface have been instructive, the natural systems approximate mo closely to a water–oil interface. A fair amount of work has therefore be reported for such interfaces in spite of the greater experimental difficulti

Protein monolayers tend to be expanded relative to those at the air–wa interface (290). Davies (291) studied hemoglobin, serum albumin, gliad and synthetic polypeptide polymers at the water–petroleum ether interf with the view of determining the behavior of the biologically important NH_2 groups and concluded that on compression they were forced into the phase.

The π–σ data for such films still fit Eq. IV-61, but with a larger *z* val indicating more flexibility in the chain. Presumably this is because the pr ence of the oil phase reduces cohesion between the hydrophobic side cha of the protein molecule.

Stigter and Dill (292) studied phospholipid monolayers at the *n*-hepta water interface and were able to treat the second and third virial coefficie (see Eq. IV-60) in terms of electrostatic, including dipole, interactions. higher film pressures, Pethica and co-workers (292a) observed quasi-fi order phase transitions, that is, a much flatter plateau region than show

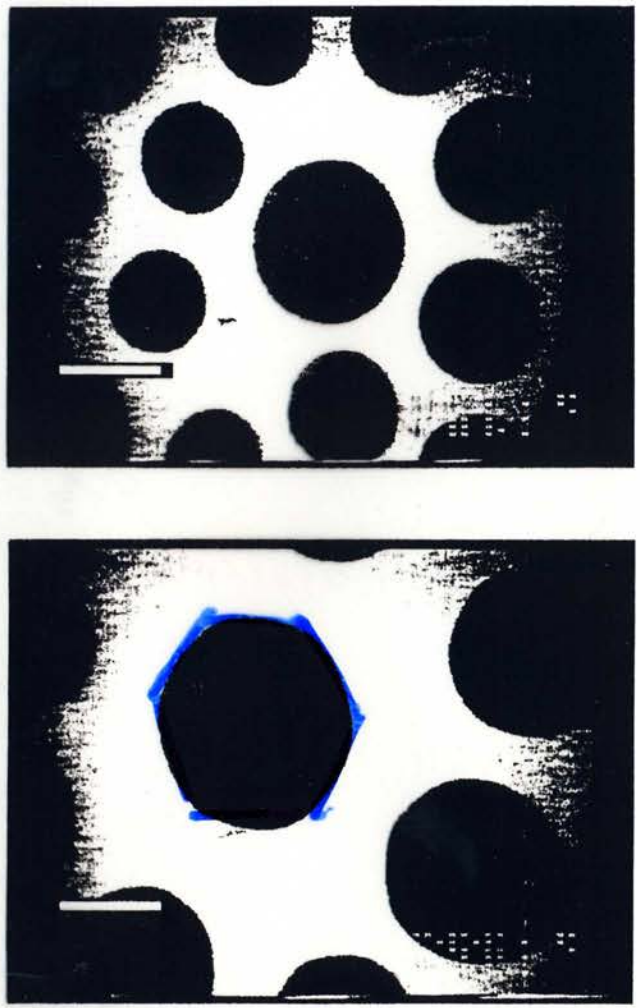

Figure 3 Fluorescence microscope images of methyl hexadecanoate along the LE–LC phase boundary. (*a*) 28 C, (*b*) 20 C. The bars represent 100 μm. Note the sixfold changes in curvature that appear at 27 C.

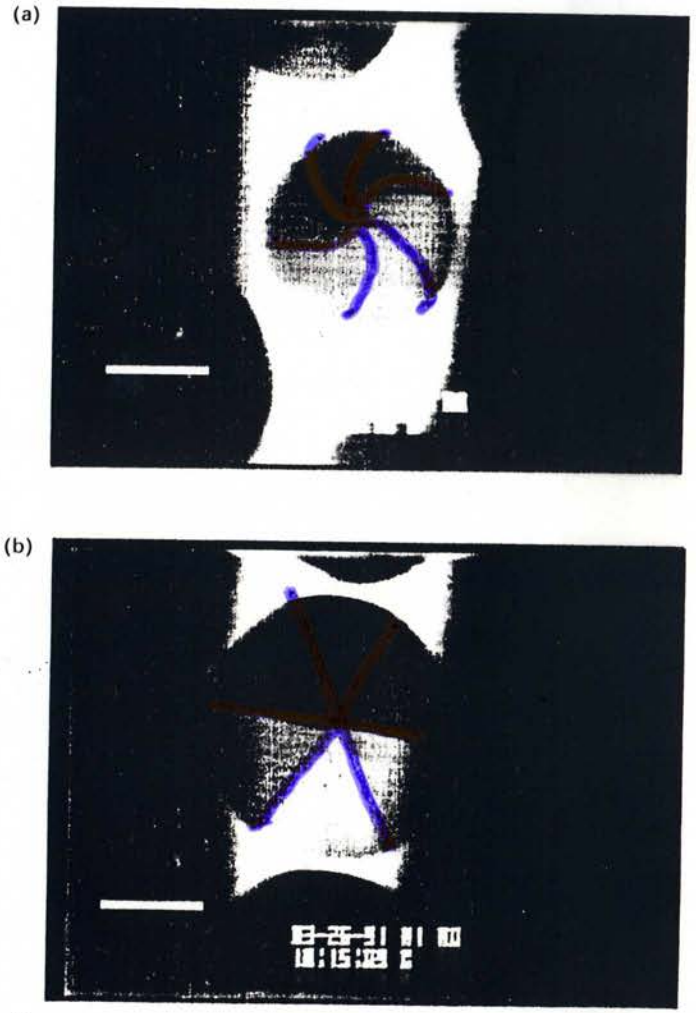

Figure 4 Fluorescence microscope images with polarized excitation. The bars represent 100 μm. (*a*) Methyl octadecanoate at 31 C; (*b*) methyl eicosanoate at 20 C. The octadecanoate domains are chiral; those in the eicosanoate are achiral.

PRE 50 (94) 413-428

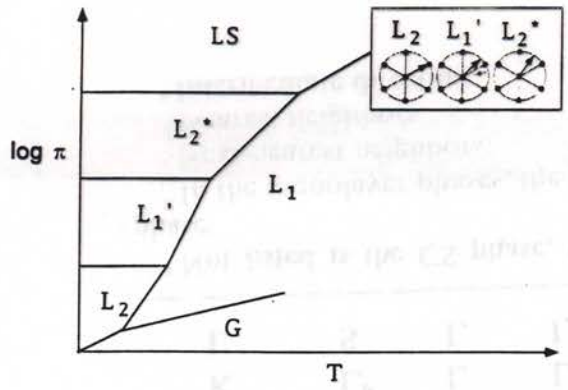

FIG. 1. Schematic pressure-temperature (π-T) phase diagram showing several of the monolayer phases that have been identified in fatty acids and their esters. The relative locations of the gas (G), liquid-expanded (L_1), and superliquid phases (LS) are much the same for many substances. The locations of the other phases and the positions of the boundaries between them are more variable and less well known. The inset shows the orientation of the molecular tilt azimuth with respect to the local sixfold structure of the head groups that exists in the three tilted hexatic phase L_1', L_2, and L_2^*.

director points toward nearest neighbors in the L_2 phase, toward next-nearest neighbors in the L_2^* phase, and along an intermediate direction in the L_1' phase. In the language of smectic liquid crystals, the tilted LC phases are the analogs of, respectively, the smectic-I, -F, and -L phases (we will use this latter notation). The fact that the surfactant liquid crystals appear to be hexatics is somewhat surprising since tilted hexatics are less common in the phase behavior of $D=3$ liquid crystals. On the other hand, the nematic phase, which is quite common in $D=3$ liquid crystals, appears to be absent in the surfactant films studied to date.

Liquid crystals in $D=3$ are birefringent and can be characterized visually by their striking multicolored *textures* when viewed between polarizers; the textures reflect the spatial variation of the local optical axis of the material. This spatial variation may be due to metastable "defects," which for topological reasons cannot decay, or, for finite systems, it may be imposed by boundary conditions at the sample boundary. Textures are also very useful as a quick diagnostic for the type of liquid crystal involved. Recent studies of monolayers by polarized fluorescence [7] and Brewster-angle reflection [8,9] have shown that the spatial variation of the c director can be observed and demonstrated that LC phases of surfactant monolayers also exhibit textures; see Fig. 2.

At first sight, it would appear natural to expect that LC-phase textures should be similar to those of the analogous $D=3$ smectic phases for achiral molecules (the surfactant molecules used were generally achiral). The most striking texture of the $D=3$ phases is a fivefold star-shaped object [2]. The appearance of stars in tilted hexatics can be readily explained by allowing the c director to couple to the local orientation of the six hexatic crystallographic axes (see below). LC phases have indeed been found to exhibit star textures very similar to those of the free-standing tilted smectic hexatic films, but a large variety of other textures has been found as well. For example, the "ground state" of the LC phase for some fatty acids is a stripe texture consisting of straight or kinked defect lines [10]. The mesoscopic studies thus suggest that the analogy between surfactant monolayers and the $D=3$ tilted-hexatic liquid crystals may not be complete since in the latter the ground state is believed to be uniform.

B. Droplet textures

The spatial variation of the optical axis of a texture reflects an inhomogeneous structure of the underlying order parameter. The order parameter of an LC phase is rather complex: it is a combination of the c director and

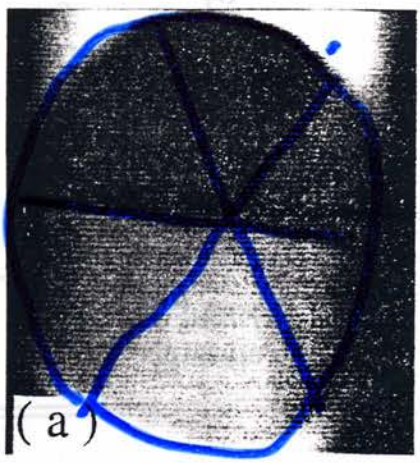

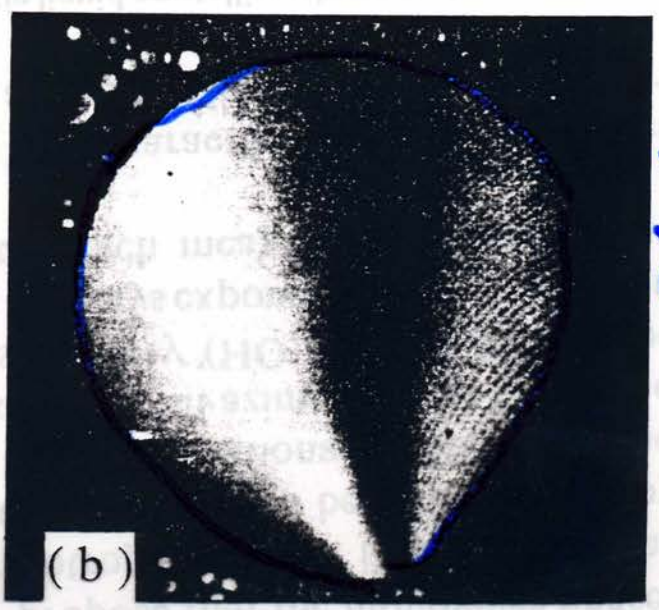

FIG. 2. Images of droplet textures. The droplets are surrounded by the liquid expanded phase, which is isotropic. (a) Polarized fluorescence microscope image of a star defect in a monolayer of methyl octadecanoate. (b) Brewster-angle microscope image of a boojum in a monolayer of pentdecanoic acid (courtesy J. Meunier).

the hexatic order parameter. We characterize the hexatic order by the angle θ made by the six crystallographic axes with a fixed axis, say, the x axis (see Fig. 3). This "bond-angle" field $\theta(\mathbf{x})$ can, like $\hat{\mathbf{c}}(\mathbf{x})$, vary across the sample. Obviously, $\theta(\mathbf{x})$ is defined only modulo 60° so the LC free energy must be invariant under rotations by multiples of 60°. It is the experience in $D=3$ systems that complex order parameters produce complex textural patterns and, as mentioned, a bewildering variety of textures has indeed been observed in monolayers. The question now is whether we can hope to carry out a program of texture classification in surfactant monolayers in the same way as has been done for $D=3$ liquid crystals [11]. In this paper we will address this issue only for the simplest possible case, namely, that of a $D=2$ LC droplet inside a LE matrix. In such a confined geometry, the number of allowed textures should be severely reduced by the boundary constraints imposed on both the $\hat{\mathbf{c}}(\mathbf{x})$ and $\theta(\mathbf{x})$ fields at the LE-LC interface because they raise the energy cost of adding metastable topological defects. Electrostatic repulsions inhibit the coalescence of LC droplets and their sizes are therefore generally only of order 100 μm; their shapes usually vary between circular to (rounded) hexagonal.

Coexistence droplets in ester monolayers show a range of textures; some common ones are shown in Fig. 4. As one moves along the LE-LC coexistence curve, reversible changes are observed in both the texture and the droplet shape. On the basis of these relaxation processes, it is reasonable to assume that the observed textures represent a local equilibrium of the free energy rather than a frozen, or pinned, configuration determined entirely by the preparation history of the drops. The fluorescence data on the esters also reveal that $\hat{\mathbf{c}}(\mathbf{x})$ is fairly strongly anchored along the normal to the LE-LC interface. The boundary condition on the bond-angle field (if any) is not known since the $\theta(\mathbf{x})$ field cannot be visualized by the fluorescence studies. The observed textures are often based on the sixfold hexagonal "basic motif" shown in Fig. 4(a). The origin of the basic motif is easily understood if we assume that the hexatic degree of freedom is

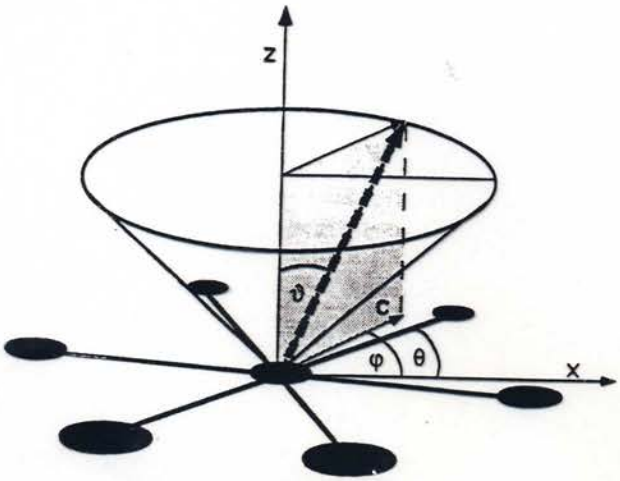

FIG. 3. Definition of the bond angle θ, the tilt angle ϑ, the tilt azimuth φ, and the director c.

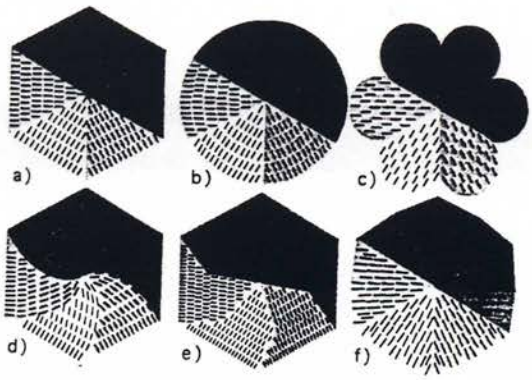

FIG. 4. Droplet textures for hexatic phases. The lines indicate the orientation of the molecular tilt azimuth within each domain and the shading gives an impression of the contrast that would be observed in an image obtained by polarized fluorescence microscopy.

relatively stiff and thus spatially uniform across the drop. In each of the six sectors of the hexagon, the in-plane director is also uniform and locked to the bond-angle field with the relative angle between them assuming the equilibrium value appropriate for the LC phase in question. At the boundary between adjacent sectors, $\hat{\mathbf{c}}(\mathbf{x})$ makes a rapid rotation of 60° to flip from one of the six hexatic directions to the next ("60° wall"). On the other hand, coexistence droplets of fatty acid monolayers have textures with no sharp boundaries but rather a smoothly varying c director. Understanding the origin of the different phenomenology of ester surfactants and fatty acid surfactants is important for learning how to interpret the observed textures.

If the droplet shape is a perfect hexagon, then the basic motif naturally satisfies normal boundary conditions for the c director at the LE-LC interface. In this view, hexagonal droplet shapes would be a consequence of the normal boundary conditions on the molecular tail rather than the direct influence of the hexatic order on the LE-LC interface. This is confirmed by the fact that in the high-pressure LS phase, where the molecules are perpendicular to the air-water interface, the droplets are *not* hexagonal even though the phase is believed to be hexatic [7]. It is important for the following to note that the strength of the boundary conditions on the c director is, in reality, limited. As shown in Fig. 4(b), experiments also show the existence of circular drops with a hexagonal interior structure, which could only satisfy normal boundary conditions by distorting the textural uniformity inside the six sectors, which does not appear to be the case. As will be discussed below, a circular shape is actually a natural variation of the basic motif if we allow for an increase of the LE-LC line tension with respect to that of a 60° wall.

The basic motif is closely related to the five-armed star-shaped defects observed both in the LC phase of materials such as pentadecanoic acid away from the coexistence line as well as in freely suspended films of tilted smectic hexatics. We can crudely think of the basic motif as a stable star-type defect imposed by the LE-LC phase boundary. The differences between the

Textures in a chiral smectic liquid-crystal film

Stephen A. Langer and James P. Sethna
Laboratory of Atomic and Solid State Physics, Cornell University, Ithaca, New York 14853
(Received 10 March 1986)

Freely suspended liquid-crystal films of the smectic-*I* phase of HOBACPC [*R*(−) hexyloxybenzylidene *p'*-amino-2-chloropropyl cinnamate] display distinctive stripe and droplet textures. We derive these patterns from a Landau expansion of the free energy using a vector order parameter. Strong pinning boundary conditions lead to boojums in the droplets and stable defect lines between the stripes. The boojum is a two-dimensional version of its namesake in superfluid ^{3}He-*A*. The surface defect in the boojum is expelled from the smectic-*I* droplet in order to lower the internal gradient energy, leaving a defect-free texture. The expulsion distance and the width of the stripes are calculated in terms of the elastic constants.

I. INTRODUCTION

Smectic liquid crystals, in which the molecules arrange themselves in parallel layers, can be drawn into stable freely suspended films only a few molecular layers thick.[1–4] In the tilted smectic phases, such as Sm*C* and Sm*I*, the molecular optical axis $\hat{\mathbf{n}}$ lies at an angle to the layer normal (see Fig. 1). The direction of the projection $\hat{\mathbf{c}}$ of the molecular axis in the plane of the film can be observed by polarized reflection microscopy. Basically, if the direction of polarization of incident light is parallel or perpendicular to $\hat{\mathbf{c}}$, then the polarization is unchanged upon reflection, whereas if the direction of polarization of the incident beam is at some other angle, the polarization is rotated. When viewed through crossed polarizers, those regions of the film with $\hat{\mathbf{c}}$ parallel to either of the polarizers appear dark. These dark fringes are known as *schlieren* lines.[5] Defects in the liquid crystal show up as discontinuities or points of convergence of *schlieren* lines.

Distinctive *schlieren* patterns have been observed by Clark, Van Winkle, and Muzny[6] in freely suspended films of HOBACPC [*R*(−) hexyloxybenzylidene *p'*-amino-2-chloropropyl cinnamate], a chiral liquid crystal which forms ferroelectric phases of Sm*C* and Sm*I*. Both Sm*C* and Sm*I* are tilted phases; while the nature of the ordering in these phases is still under investigation,[7] Sm*C* is known to have only short-range positional order within layers, while Sm*I* has a more pronounced hexagonal order and more translational order than does Sm*C*. In both cases there exists orientational order between layers. On cooling a Sm*C* film through 55 C small roughly circular domains of Sm*I* nucleate. The Sm*I* droplets drift away from their nucleation sites and grow into the Sm*C*. The droplets are characterized by from one to three straight *schlieren* lines which appear to originate at a point off the edge of the droplet. (See Fig. 2.) The *schlieren* lines lie at 45° to one another. In circular droplets, relatively free from the distortions caused by contact with neighboring

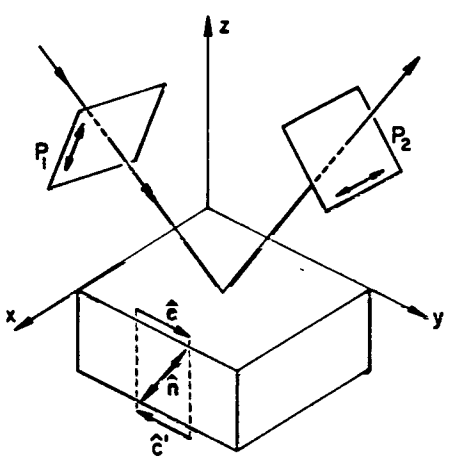

FIG. 1. Schematic of the experiment. The smectic film lies in the x-y plane. The film is viewed by reflection between crossed polarizers P_1 and P_2. The molecular optical axis is $\hat{\mathbf{n}}$—the molecule shown lies in the y-z plane. The order parameter $\hat{\mathbf{c}}$ points towards the tops of the tilted molecules, and lies in the x-y plane. Consequently, when the film is viewed from below, the order parameter $\hat{\mathbf{c}}'$ is the reverse of $\hat{\mathbf{c}}$.

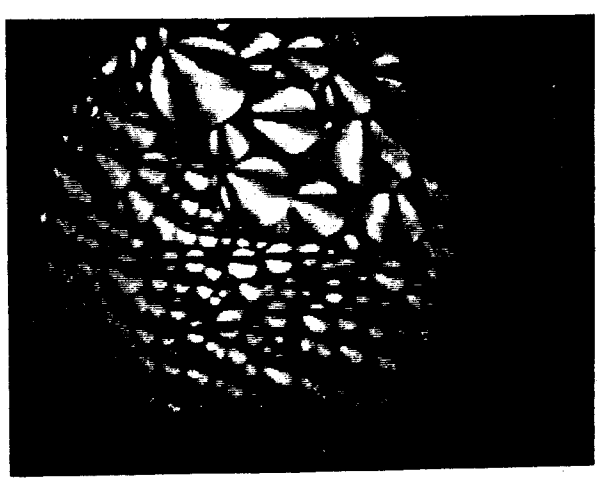

FIG. 2. Polarized reflection micrograph of the droplet texture. The polarization axes are parallel to the edges of the picture. The diameter of the illuminated region is roughly 0.24 cm. Photo courtesy of N. A. Clark, D. H. Van Winkle, and C. Muzny.

tures.

A. Conclusions

We describe the smectic film by a unit vector order parameter $\hat{c}$. There are two contributions to the free energy of the film—bulk terms involving integrals of gradients of $\hat{c}$ over the area of the system, and surface terms involving line integrals around the boundary of the system. In a system of size R the gradients of the order parameter scale as $1/R$. Since the bulk free-energy density is quadratic in the gradients, the total bulk free energy (integrated

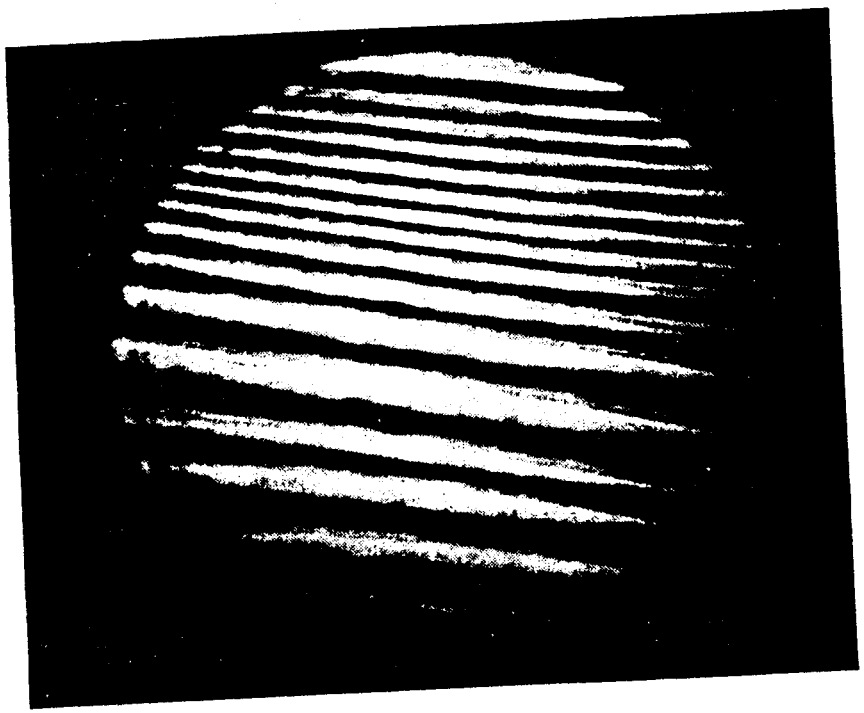

FIG. 3. Polarized reflection micrograph of the stripe texture. Photo courtesy of N. A. Clark, D. H. Van Winkle, and C. Muzny.

indeed a minimum of the free energy and calcu
far the defect is expelled from the droplet.

The strong boundary conditions are also responsibl
the presence of stripes in the film. Each defect-line
carries a positive free energy J_0 per unit length, bu
cause the boundary condition can be satisfied along
sides of the defect lines, the net free energy of the
may be negative. A negative defect energy does not
to an infinite density of defect lines, however. In orc
satisfy the boundary condition at both sides of a s
the order parameter must rotate through 180° betwe
fect lines, so narrow stripes entail large gradient ene
The balance between gradient energies, surface ene
and defect core energies leads to a finite nonzero
width. This width is calculated in Sec. III A.

II. FORM OF THE FREE ENERGY

A. The order parameter

Let the smectic film lie in the x-y plane. At each
(x,y) in the film denote the local molecular axis of
anisotropy by $\hat{n}$, averaged over thermal motions a
depth of the film. It is convenient to visualize $\hat{n}$
long axis of the molecules, although this does not
sarily coincide with the optical anisotropy axis.
ing that the molecules are effectively symmetrical
tail, there is no distinction between $\hat{n}$ and $-\hat{n}$, so
director rather than a vector. We will describe the
a unit-vector order parameter $\hat{c}(x,y)$, or, equivale
an angle $\phi(x,y)$, where $\hat{c}=\hat{x}\cos\phi+\hat{y}\sin\phi$. $\hat{c}$ point
the projection of $\hat{n}$ in the x-y plane, as shown in

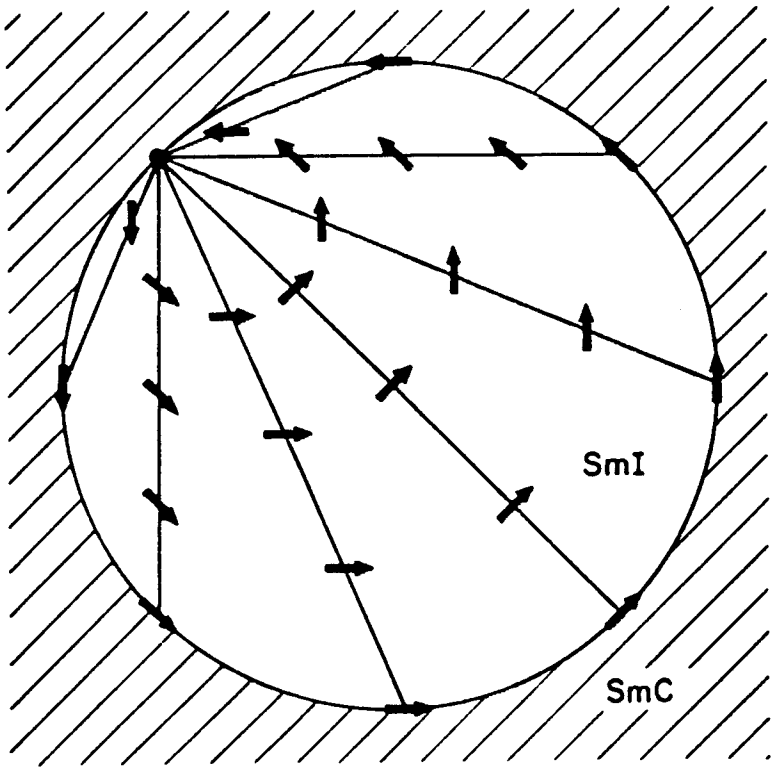

(a)

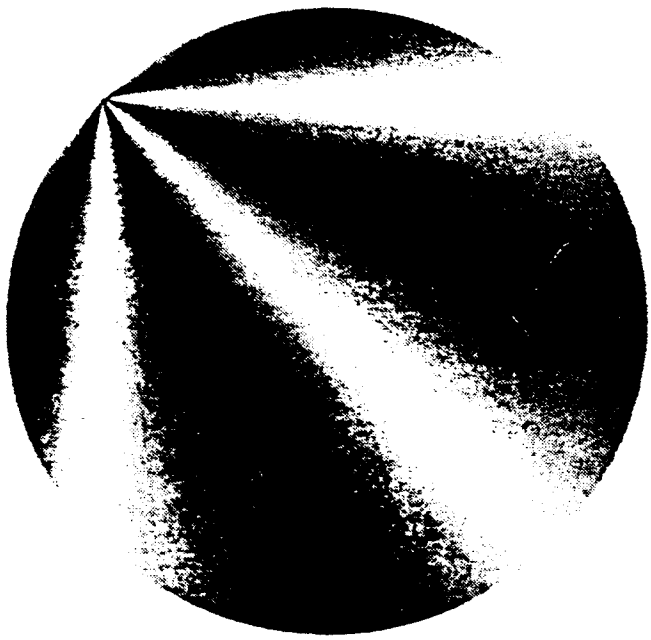

(b)

HOBACPC has ferro
leads to nonlocal terms
found experimentally th
dipole interactions
benzylidene-p'-amino-2-
al similar to HOBACPC
ionic impurities. Alth
HOBACPC is stronger t
also neglect these long-ra

B. Symmetr

The free energy of the

$$\mathcal{F}[\hat{\mathbf{c}}]=\int\int dx\,dyF$$

where $\mathcal{F}_{\text{defect}}$ is the free
energy density F is a s
dients, and must be
transformations which l
include rotations about t
the $\hat{\mathbf{x}}$ or $\hat{\mathbf{y}}$ axes, and tra
Chiral molecules are no
and only if the liquid cr
ant under reflections thr

The free-energy densit
and surface terms.[9] Bu
free energy over the wh
divergences and other
boundaries and defects.

1.

The bulk gradient fr
those terms in a Landa
divergences and are co
the system. A simple
series may be truncated
of $\hat{\mathbf{c}}$. Consider an nth-c
order R^{-n}, where R is
in (1) contributes a fac
term has the dimensions

DMPC / DChol

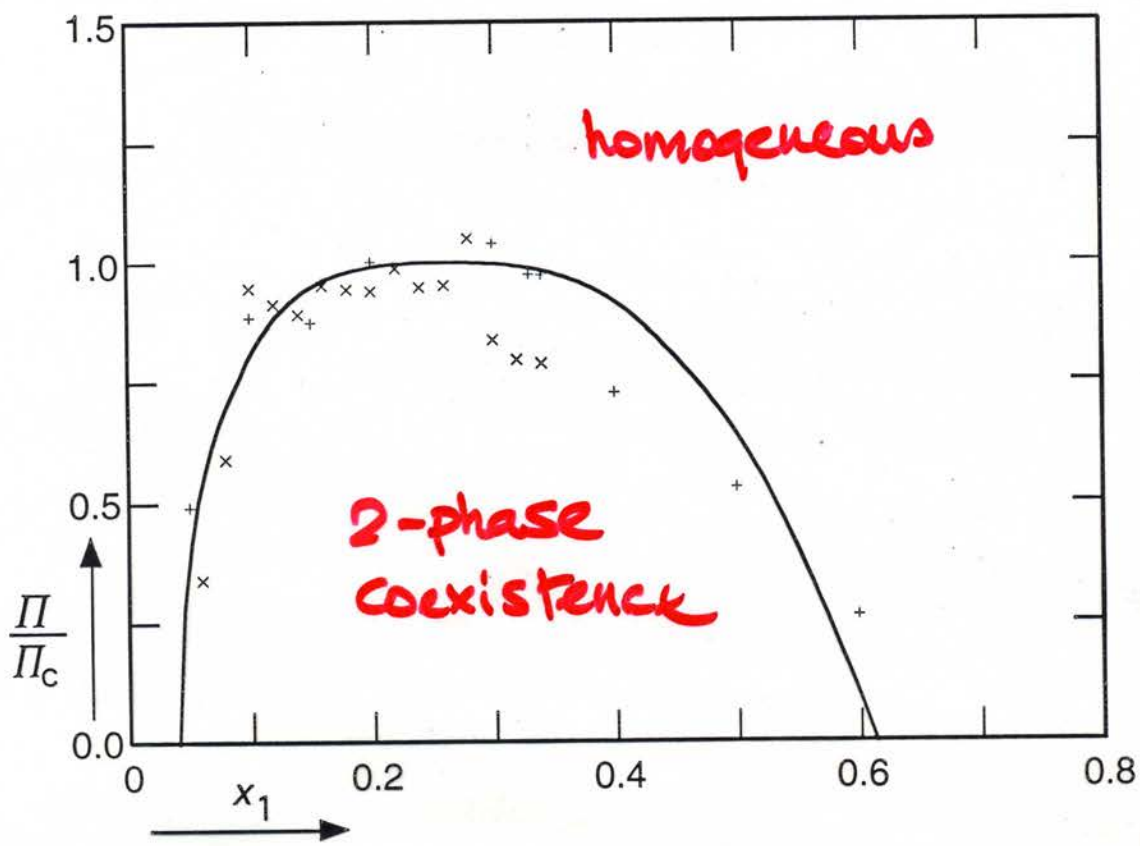

Paper3: Figure 1

CIRCLE -> LABYRINTHINE TRANSITION

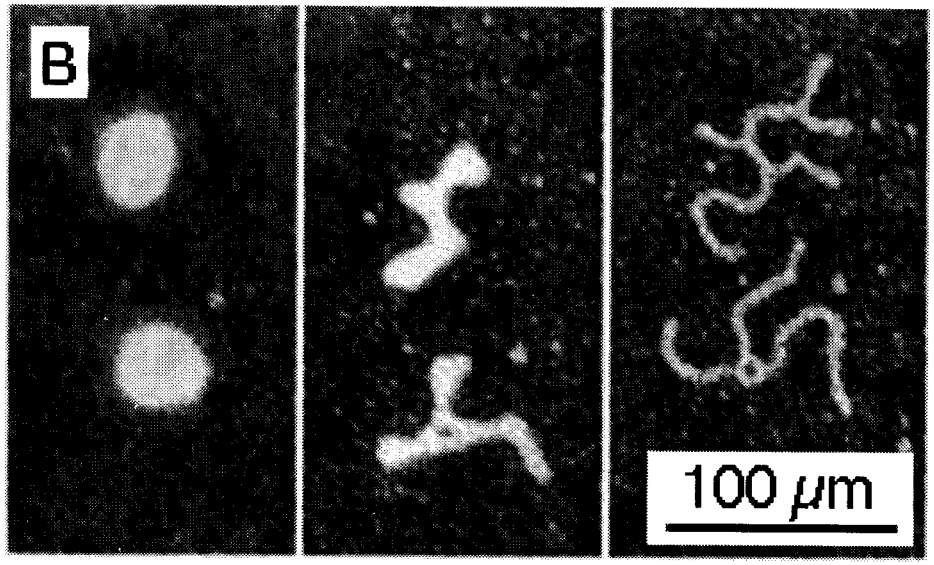

PA + 20 wt% SP-B 1-25 at zero surface pressure

Presence of Stripe Phases in both PA/SP-B 1-25 and Fluorescein SP-B 1-25 Films

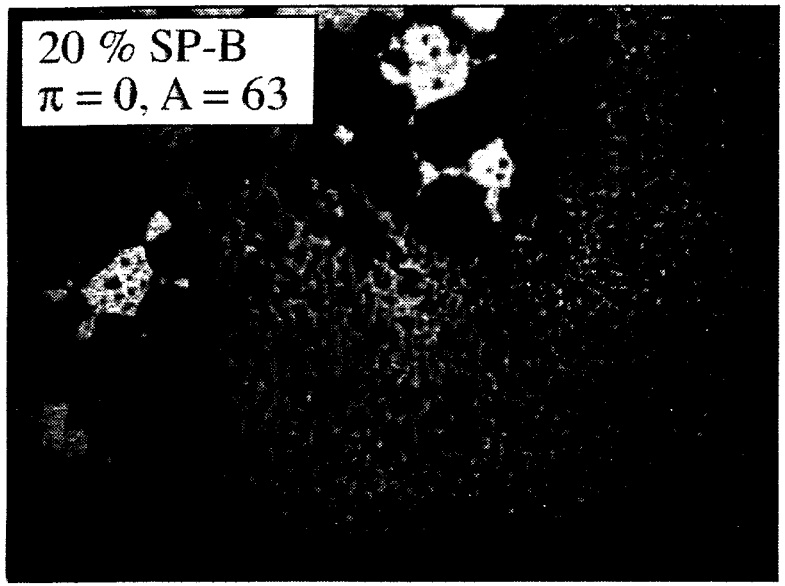

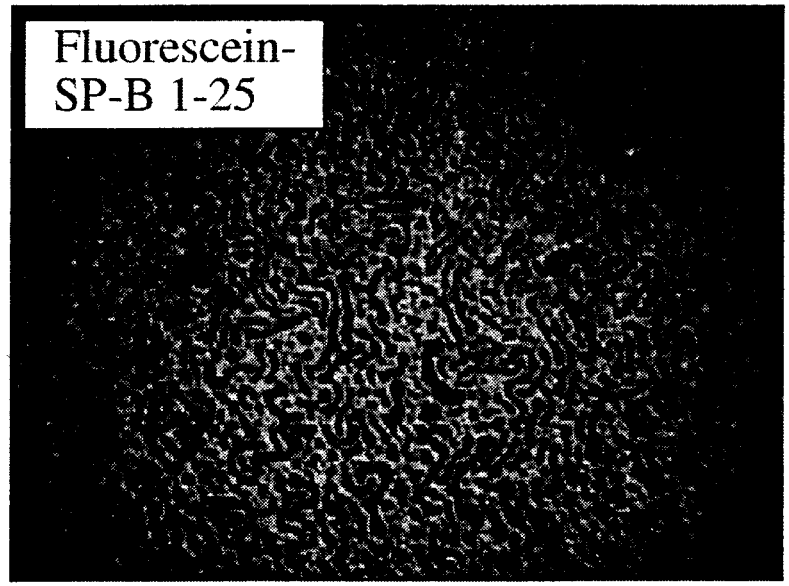

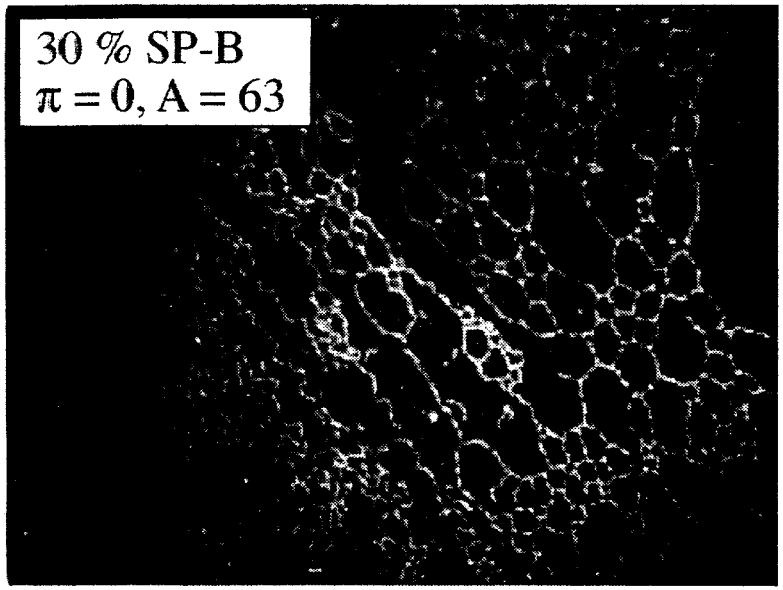

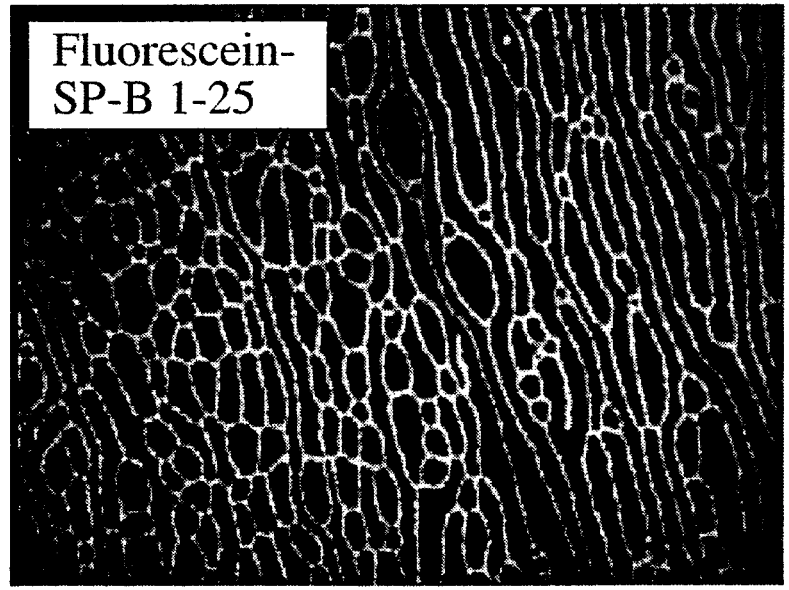

PATTERN FORMATION

- diverse set of physical, chemical, and biological systems exhibits macroscopic pattern and texture

  e.g. thin films of type I superconductors, ferrofluids, ferromagnetic garnets, chemical reaction-diffusion systems ...

- two partially incompatible species

- common structural features

- characteristic widths

- modulated by external parameters

"Pattern Formation by Interacting Chemical Fronts"

Lee, McCormick, Ouyang & Swinney Science 261, 192 (93)

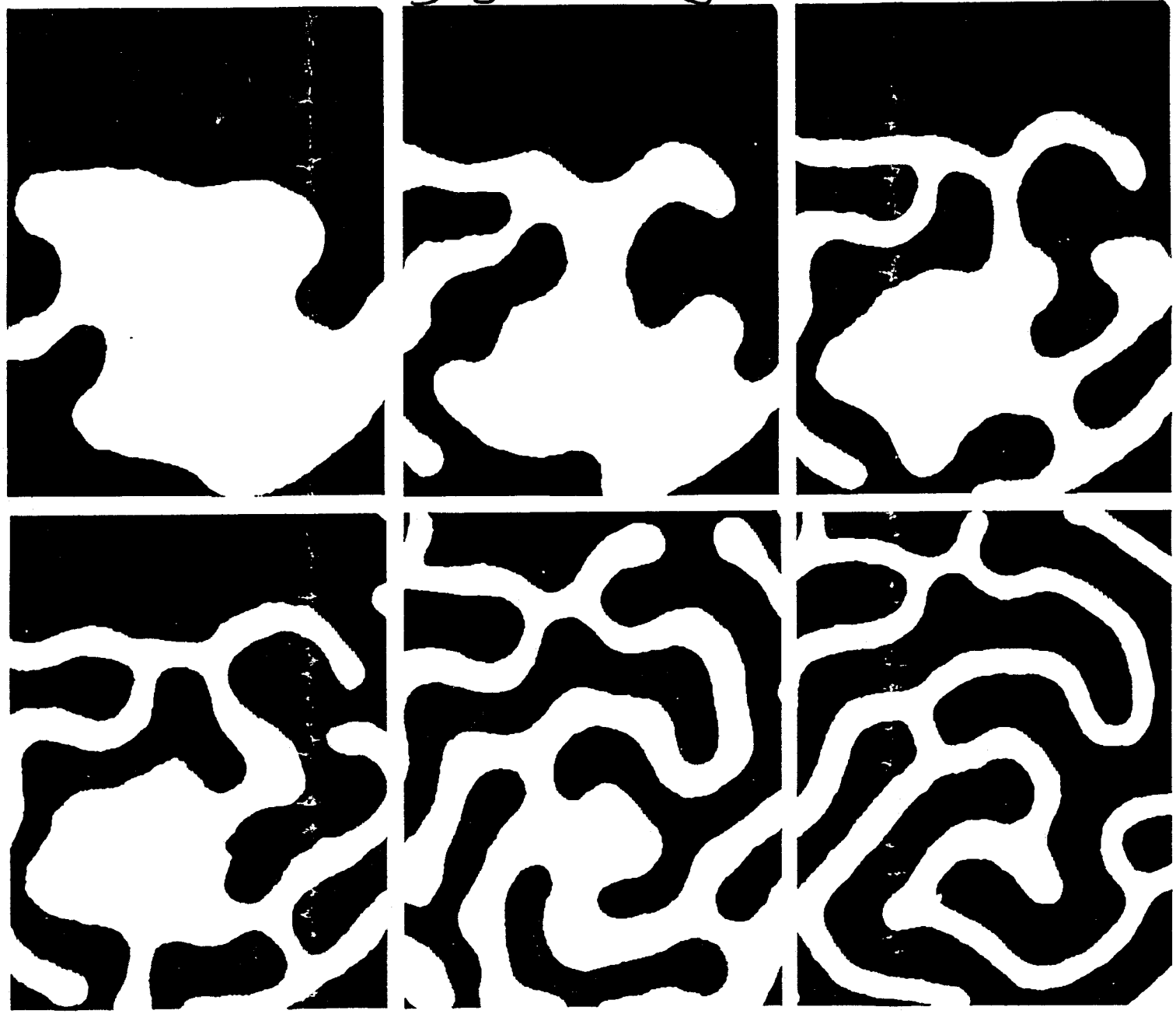

ate - ferrocyanate - sulphite bistable chem. react^{n}
large osc. in pH in stirred flow reactor

"Labyrinthine Pattern Formation in Magnetic Fluids"

Dickstein. Erramilli. Goldstein. Jackson. Langer Science 261. 1012 (93)

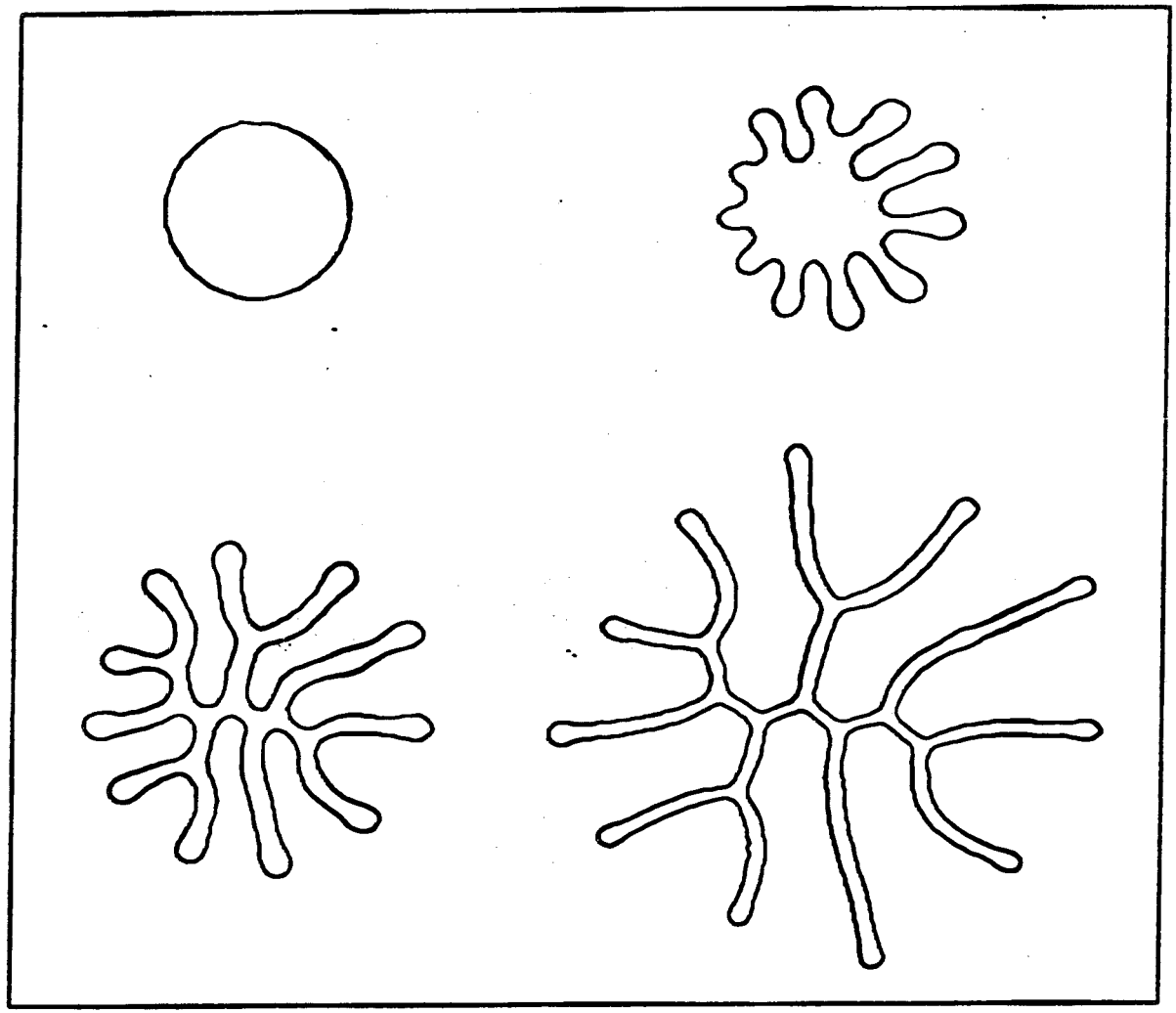

MOTIVATION

Circular liquid monolayer domain

Stripe pattern

- Circular domains become unstable –

  under what conditions?

  turn into what shapes?

  any route?

- Quantitative understanding –

  model based on competing interactions?

- Experimentally observable?

LINE TENSION VS ELECTROSTATICS

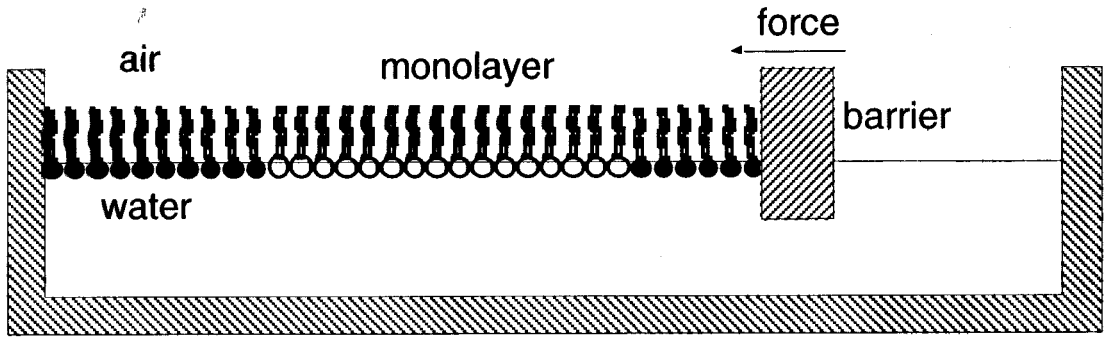

idealization:
2 dimensional sheet
of mobile dipoles

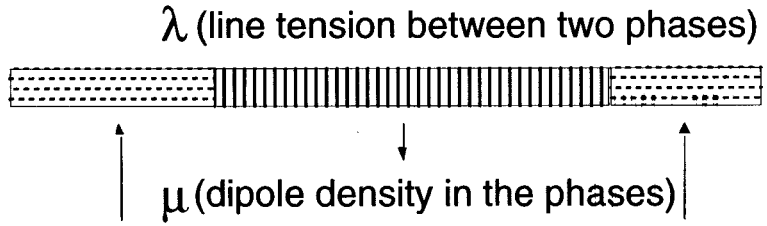

Equilibrium shapes: depend only on electrostatic and interfacial effects

Dynamics: affected by viscous coupling to sub- and super-phase.

Energetics of Lipid Domains

$F = F_{el} + F_\lambda$ ← line tension energy

↑ domain shape-dep. electrostatic energy

Energy of dipole-dipole interaction in a 2D domain of area A

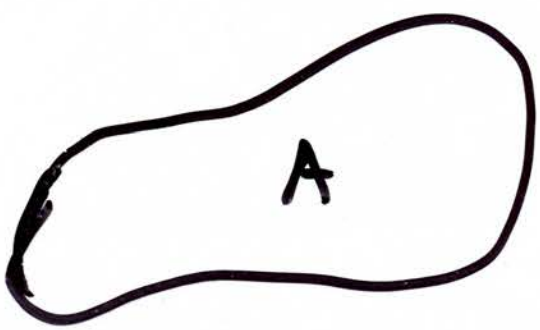

For two elements of area dA & dA'

Energy of interact^n $= \dfrac{\mu^2 dA\, dA'}{\rho^3}$

$|\vec{r} - \vec{r}'|$ = dist. b/w elements.

$\rho^2 = |\vec{r} - \vec{r}'|^2 + \Delta^2$

↑ cutoff

≈ dist. x molecular

Energy of dipolar interaction

$$E_A = \frac{1}{2} \iint \frac{\mu^2 \, dA \, dA'}{\rho^3}$$

↑ avoid double counting

Another way to look at it

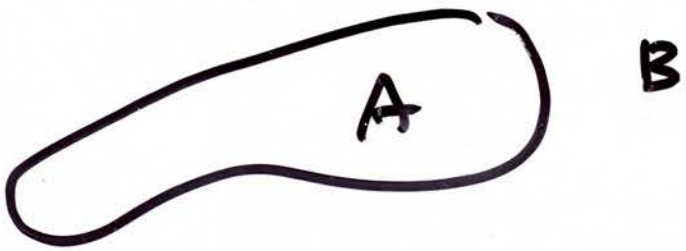

Imagine A is surrounded by domain B

that extends out to ∞

Let Σ be the energy per unit area of an int.

2-D system (domain A plus B)

A be the area of A

B be " " " B

Total energy (infinite)

$$\Sigma A + \Sigma B = E_A + E_B + \frac{\mu^2}{2} \iint \frac{dA \, dB}{\rho^3} \uparrow$$

$$+ \frac{\mu^2}{2} \iint \frac{dB \, dA}{\rho^3} \leftarrow \text{total interaction}$$

$P = Q = \frac{1}{\rho^n}$

$$\frac{\partial^2 P}{\partial x' \partial x} + \frac{\partial^2 P}{\partial y' \partial y} = \frac{\partial^2 P}{\partial \rho^2}\left(\frac{\partial \rho}{\partial x'}\frac{\partial \rho}{\partial x} + \frac{\partial \rho}{\partial y'}\frac{\partial \rho}{\partial y}\right) + \frac{\partial P}{\partial \rho}\left(\frac{\partial^2 \rho}{\partial x' \partial x} + \frac{\partial^2 \rho}{\partial y' \partial y}\right)$$

$$\frac{\partial^2 \rho}{\partial x \partial x'} + \frac{\partial^2 \rho}{\partial y \partial y'} = -\frac{1}{\rho} - \frac{\Delta^2}{\rho^3}$$

$$\left(\frac{\partial \rho}{\partial x'}\right)\left(\frac{\partial \rho}{\partial x}\right) + \left(\frac{\partial \rho}{\partial y}\right)\left(\frac{\partial \rho}{\partial y}\right) = -1 + \frac{\Delta^2}{\rho^2}$$

$$\frac{\partial^2 P}{\partial \rho^2} = n(n+1)\frac{1}{\rho^{n+2}}$$

$$\therefore \frac{\partial^2 P}{\partial x \partial x'} + \frac{\partial^2 P}{\partial y \partial y'} = -n^2 \frac{1}{\rho^{n+2}} + n(n+2)\frac{\Delta^2}{\rho^{n+4}}$$

$$\int_A \int_{B'} \frac{1}{\rho^{n+2}} dA\, dB' = -n^{-2} \iint \frac{1}{\rho^n}\, d\vec{r} \cdot d\vec{r}\,'$$

$$+ \frac{(n+2)}{n} \Delta^2 \int_A \int_{B'} \frac{1}{\rho^{n+4}}\, dA\, dB'$$

Green's Eqⁿ

$$\iint_{A\,B'} \frac{1}{\rho^3}\, dA\, dB' = -\oint_{A\,B'} \frac{1}{\rho}\, d\vec{r} \cdot d\vec{r}\,' + C$$

Line integral around outer ∞ perimeter of B B then neglected

$$\frac{1}{\rho} \to 0$$

When inner perimeter of B' is brought into contact w/ domain A

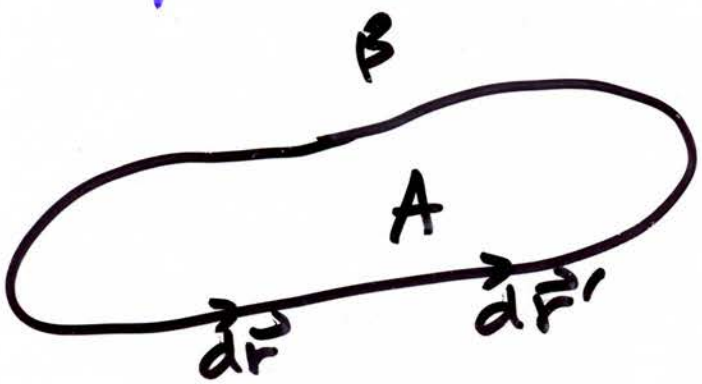

By convention the double line integrals from Green's Theorem are in opp. dir.
When B' is brought to A, it's convenient to let the 2 line integrals be in the same dir.

$$\therefore \mathcal{E}_A = \mathcal{E}A - \frac{\mu^2}{2} \int\int \frac{d\vec{r} \cdot d\vec{r}'}{\rho}$$

Related to ferromagnetic fluid circuits

What is the energy of domain A in the absence of B?

$$E_A = \varepsilon A - \frac{M^2}{2}\iint \frac{dA\,dB}{\rho^3}$$

→ evaluate using Green's Theorem

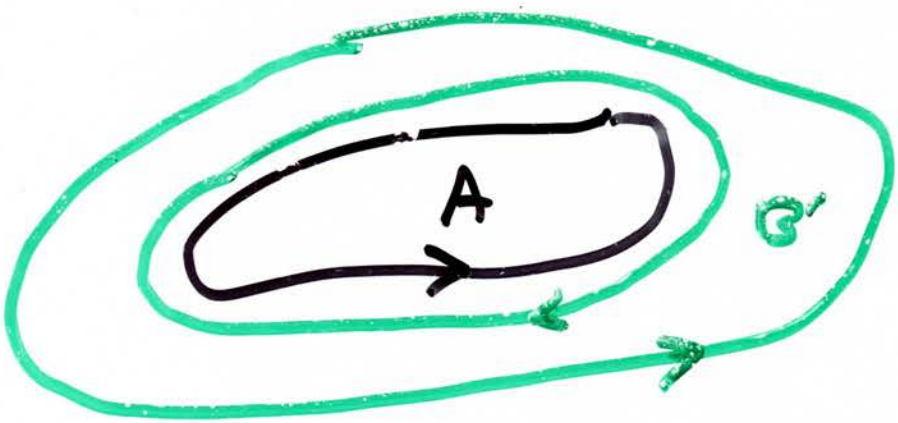

A(x,y) ; B(x',y') ; P & Q are f(x,y)

For closed curve def. A

$$\iint_A \left(\frac{\partial Q}{\partial x} + \frac{\partial P}{\partial y}\right) dx\,dy = \int P\,dx + Q\,dy$$

if P, Q are f(x, x', y, y')

$$\int_{B'}\int_{A'} \left(\frac{\partial^2 Q}{\partial x\,\partial x'} + \frac{\partial^2 P}{\partial y\,\partial y'}\right) dx\,dx'\,dy\,dy'$$

$$= \iint P\,dx\,dx' + Q\,dy\,dy'$$

MODEL: LINE TENSION VS ELECTROSTATIC REPULSION

Free Energy $$F = F_{el} + F_{\lambda}$$

$$F_{el} = \frac{\mu^2}{2}\iint \frac{dA \cdot dA'}{\rho^3} = -\frac{\mu^2}{2}\oint\oint \frac{d\vec{r} \cdot d\vec{r}'}{\rho} + C$$

$$F_{\lambda} = \oint \lambda d\vec{r} \qquad \rho^2 = |\vec{r} - \vec{r}'|^2 + \Delta^2$$

Circular domain of radius R

$$F = 2\pi R\left(\lambda - \mu^2 \ln\frac{e^2\Delta}{8R}\right)$$

Equilibrium radius

$$R_{eq} = \frac{e^3\Delta}{8}\exp\left(\frac{\lambda}{\mu^2}\right)$$

INSTABILITY OF A CIRCULAR DOMAIN

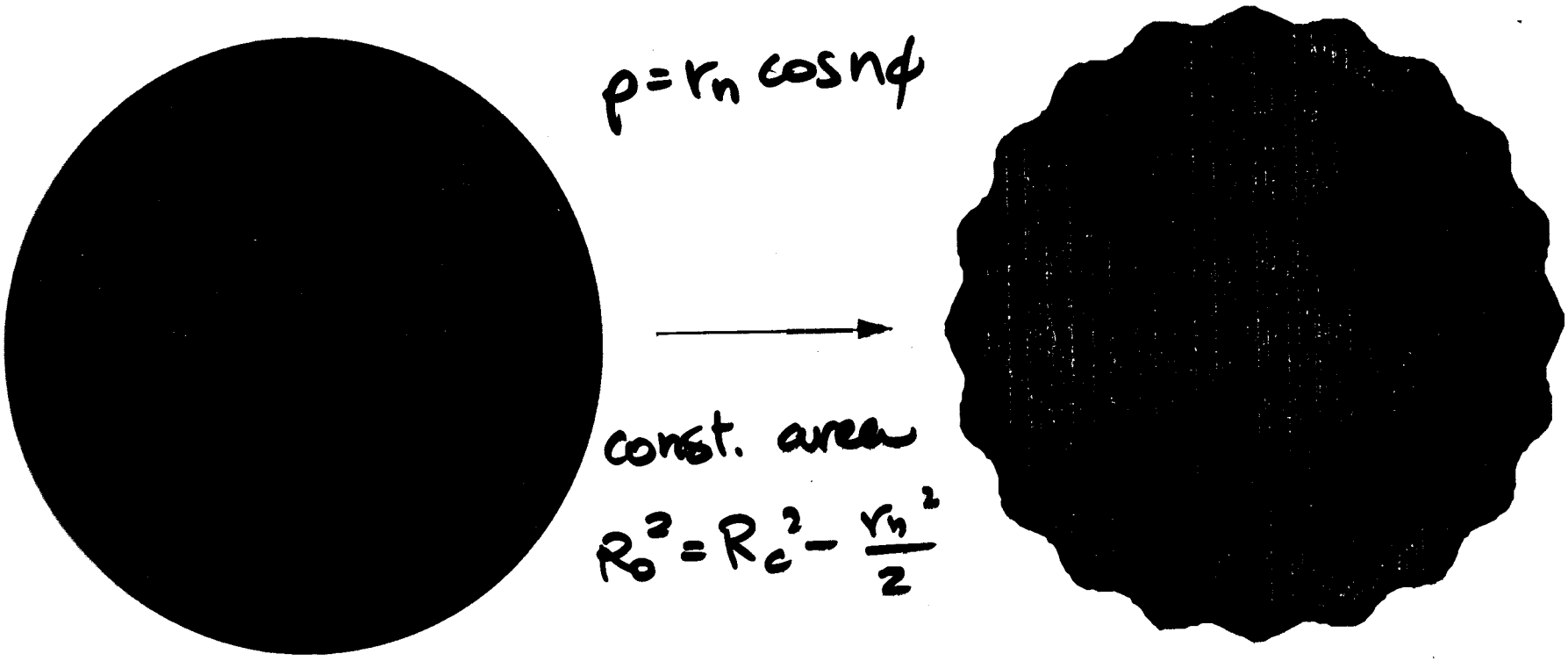

Energy associated with a circular domain with *n*-fold distortion

$$F_n = -\frac{\pi\mu^2 r_n^2}{2R_c}\left[n^2 + \sum_{q=1}^{n+1} a_q L_q + \frac{n^2-1}{2}V(x)\right] + \frac{\pi\lambda r_n^2}{2R_c}\left(n^2-1\right)$$

HARMONIC SHAPE TRANSITIONS

$$R_n = \frac{\Delta}{8} e^{Z_n} \exp\left(\frac{\lambda}{\mu^2}\right) = e^{(Z_n - 3)} R_{eq}$$

$$Z_n = -\left[n^2 + \sum_{q=1}^{n+1} a_q L_q \right] \Big/ \left[n^2 - 1 \right]$$

$$L_{n+1} = \frac{1}{2n+1} \left[4nL_n - (2n-1)L_{n-1} \right]$$

$$a_q(n) = \begin{cases} 0.75 + (n-q) \\ n - q \\ -0.5\left[n(n-1) + 0.25 \right] + 1 \\ 0.5 \\ -0.5\left[(n+1)n + 0.25 \right] \end{cases} \qquad \text{for } q = \begin{cases} 1 \\ 2..n-2 \\ n-1 \\ n \\ n+1 \end{cases}$$

HARMONIC SHAPE TRANSITIONS

$$R_n = \frac{\Delta}{8} e^{Z_n} \exp\left(\frac{\lambda}{\mu^2}\right) = e^{(Z_n - 3)} R_{eq}$$

$$Z_n = -\left[n^2 + \sum_{q=1}^{n+1} a_q L_q \right] \Big/ \left[n^2 - 1 \right]$$

$$L_{n+1} = \frac{1}{2n+1} \left[4nL_n - (2n-1)L_{n-1} \right]$$

$$a_q(n) = \begin{cases} 0.75 + (n-q) \\ n - q \\ -0.5\left[n(n-1) + 0.25 \right] + 1 \\ 0.5 \\ -0.5\left[(n+1)n + 0.25 \right] \end{cases} \qquad \text{for } q = \begin{cases} 1 \\ 2..n-2 \\ n-1 \\ n \\ n+1 \end{cases}$$

STABILITY ANALYSIS

$$R_n = \frac{e^{z_n}\Delta}{8} e^{1/\mu^2} \qquad z_n = -\left[n^2 + \sum_{q=1}^{n+1} a_q [q]\right]/[n^2-1]$$

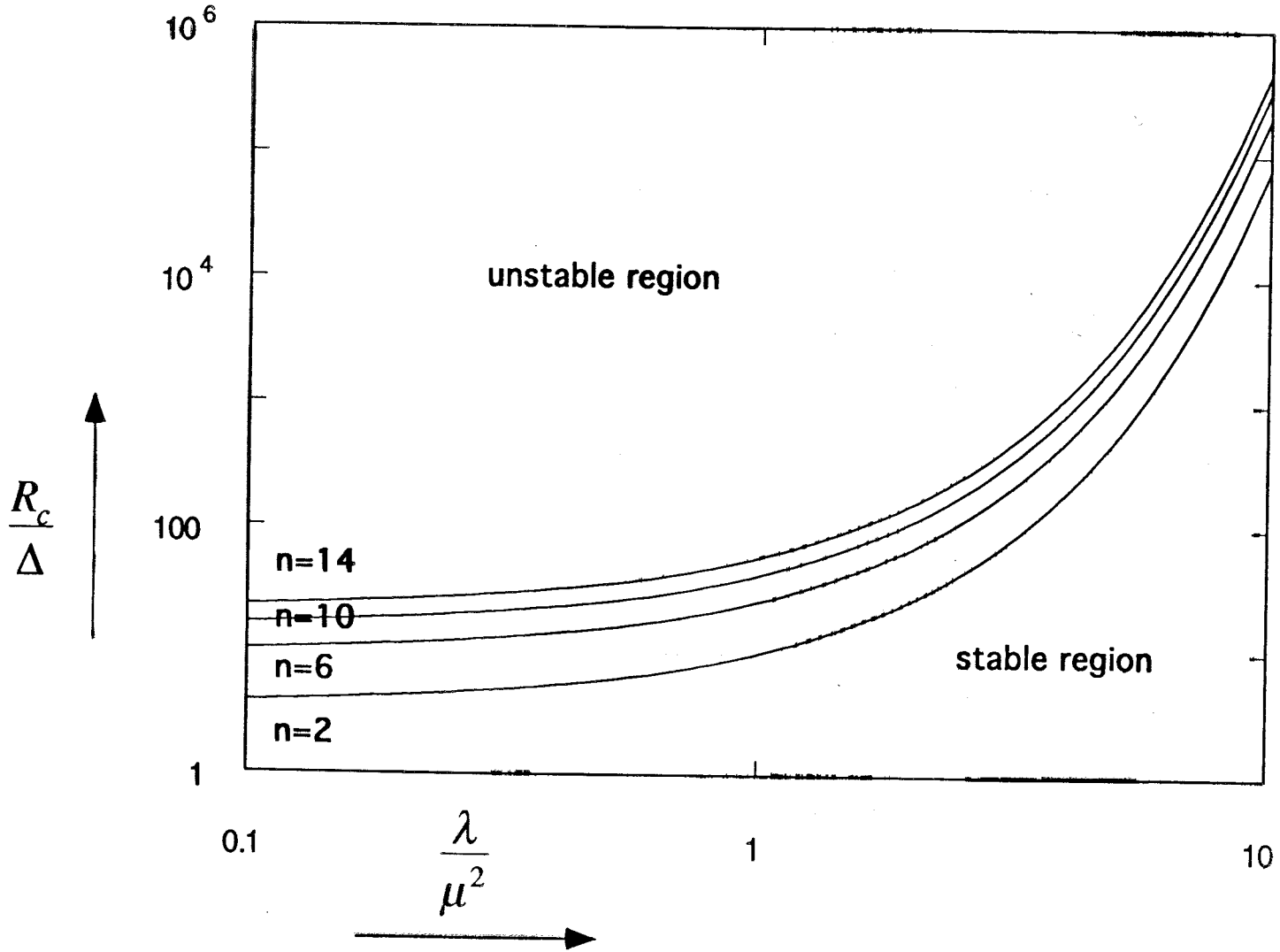

KINETICS OF INSTABILITY

-D shear
upled to
allow vector
to phase via γ

Potential flow in monolayer $\quad \vec{\nabla} \bullet \vec{v} = \nabla^2 \varphi = 0$

$$\varphi = -\frac{vR_c}{n}\left(\frac{r}{R_c}\right)^n \cos n\theta \qquad \text{for } r \le R_c$$

$$\varphi = -\frac{vR_c}{n}\left(\frac{R_c}{r}\right)^n \cos n\theta \qquad \text{for } r > R_c$$

Viscous drag from subphase: Drag ~ velocity • area

ite & ① Energy loss for circular domain shape: $\frac{1}{2\pi}\left(2r_n \frac{dr_n}{dt}\right)\left(\frac{\partial}{\partial r_n^2} F_n\right)$

② Energy loss from viscous drag:

$$\frac{2n}{2\pi}\left(\int_0^{R_c} r\,dr + \int_{R_c}^{\infty} r\,dr\right)\int_0^{\pi/n} d\theta\,\gamma(\nabla\phi)^2 = \gamma\left(\frac{dr_n}{dt}\right)^2 R_c^2\left(\frac{1}{2n}+\frac{1}{2n}\right)$$

$$\boxed{r_n = A\exp\left[-\frac{nF_n}{\gamma\pi R_c^2 r_n^2}t\right]}$$

set b.c. each → 0 @ ∞ + (0,y) $\qquad \partial r_n/\partial t = -\frac{\partial \phi}{\partial r}$

MOST RAPIDLY GROWING MODE

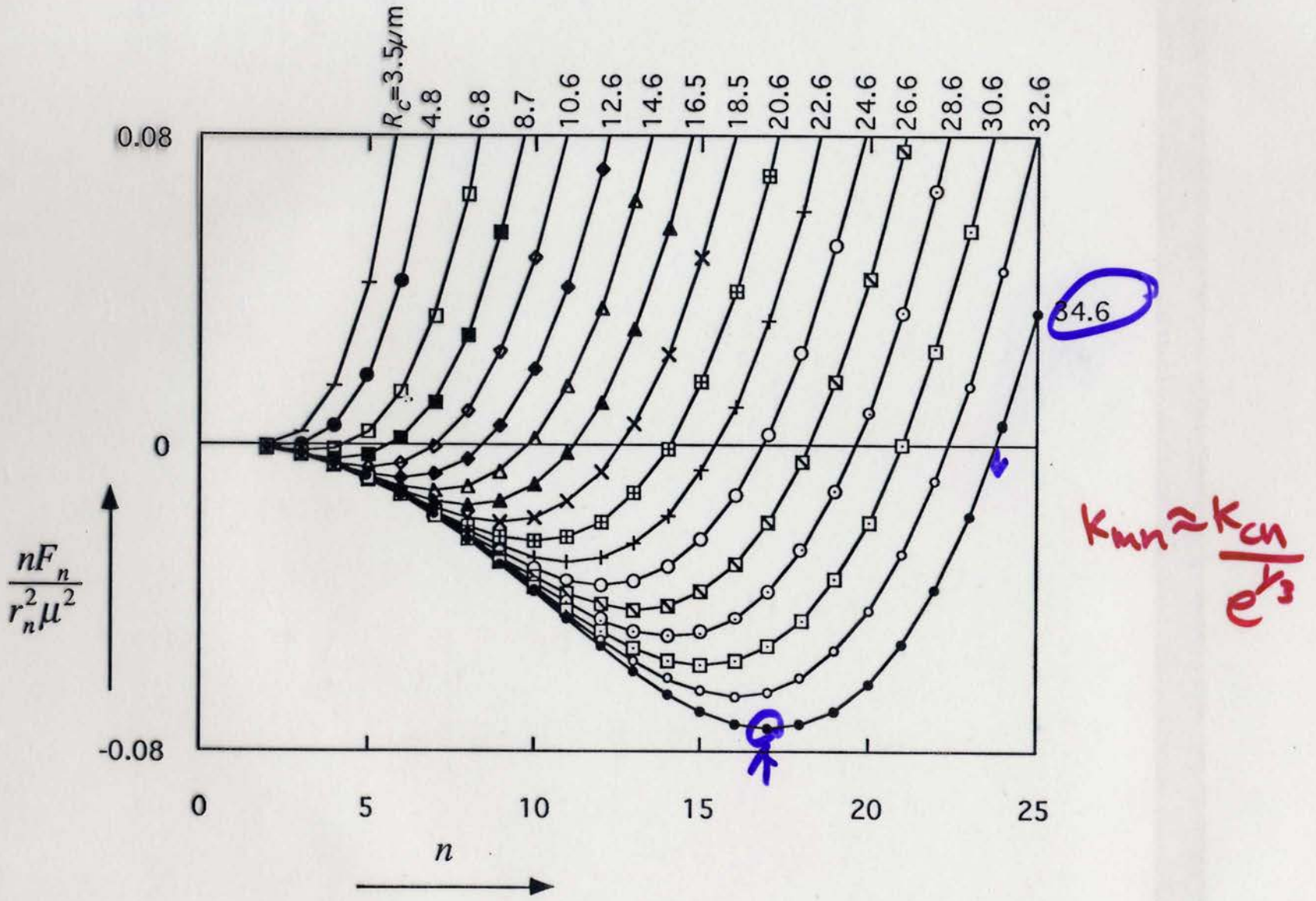

$k_{mn} \approx \frac{k_{cn}}{e^{1/3}}$

CRITICAL...FASTEST GROWING...LOWEST ENERGY

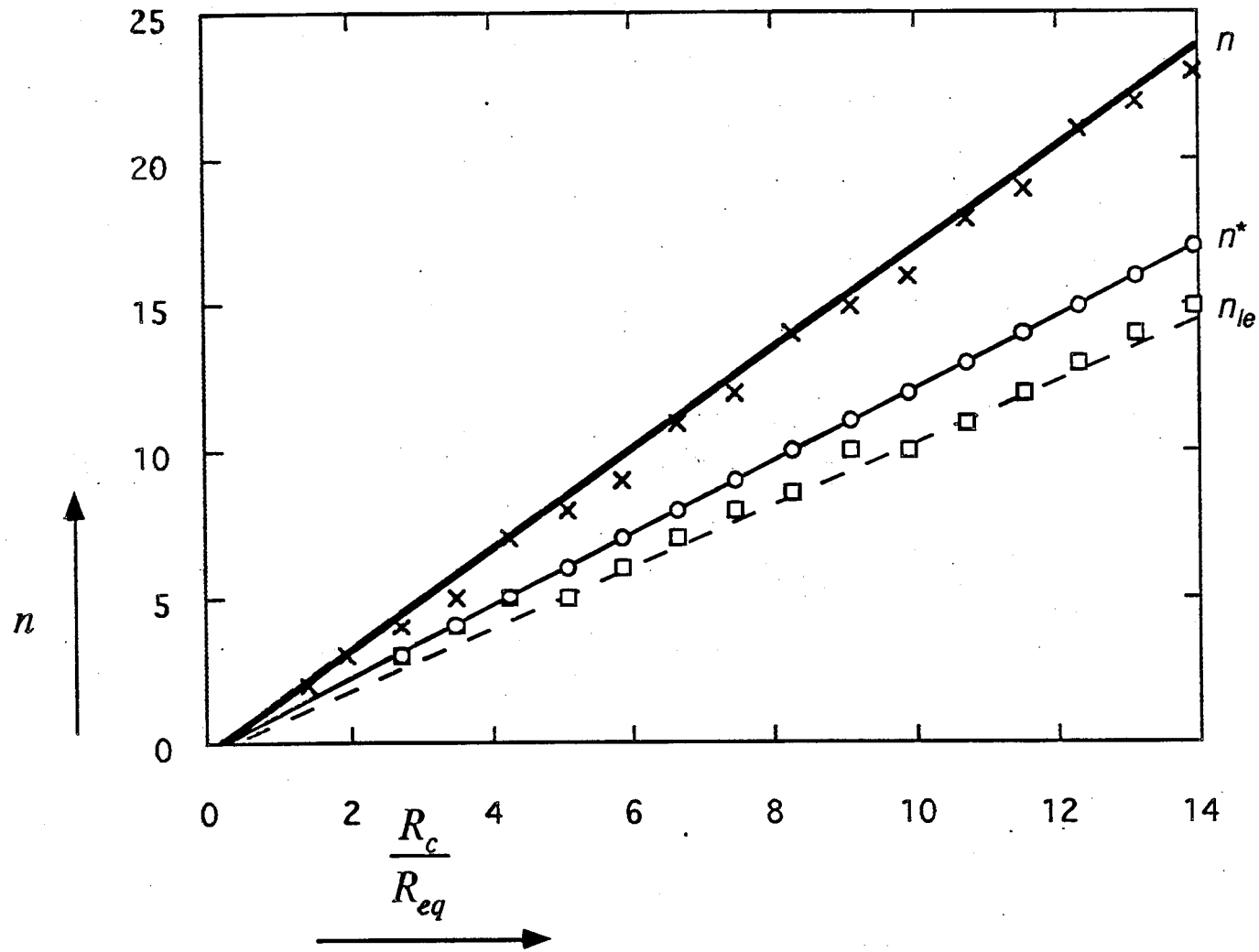

ROUTE TO SHAPE TRANSITIONS

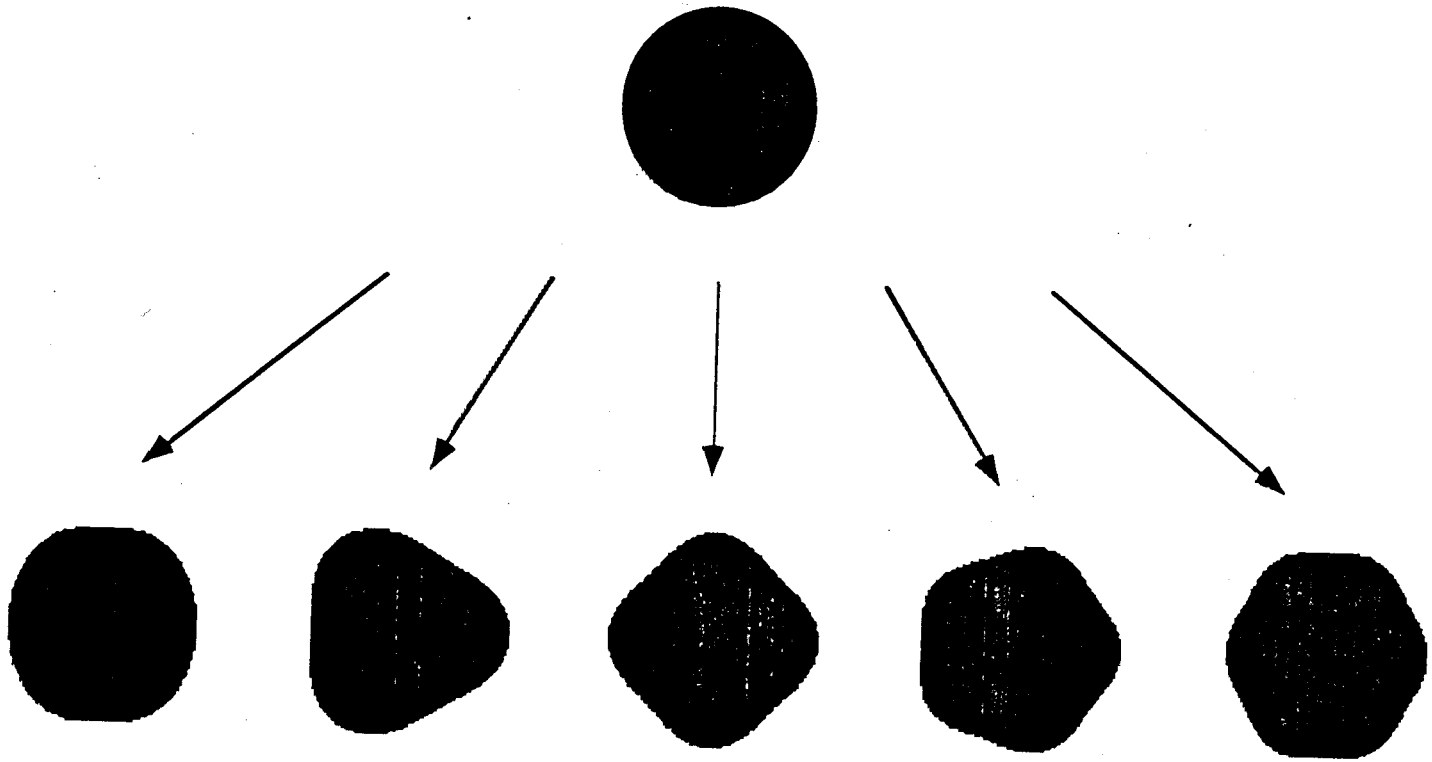

EXPERIMENTAL SETUP

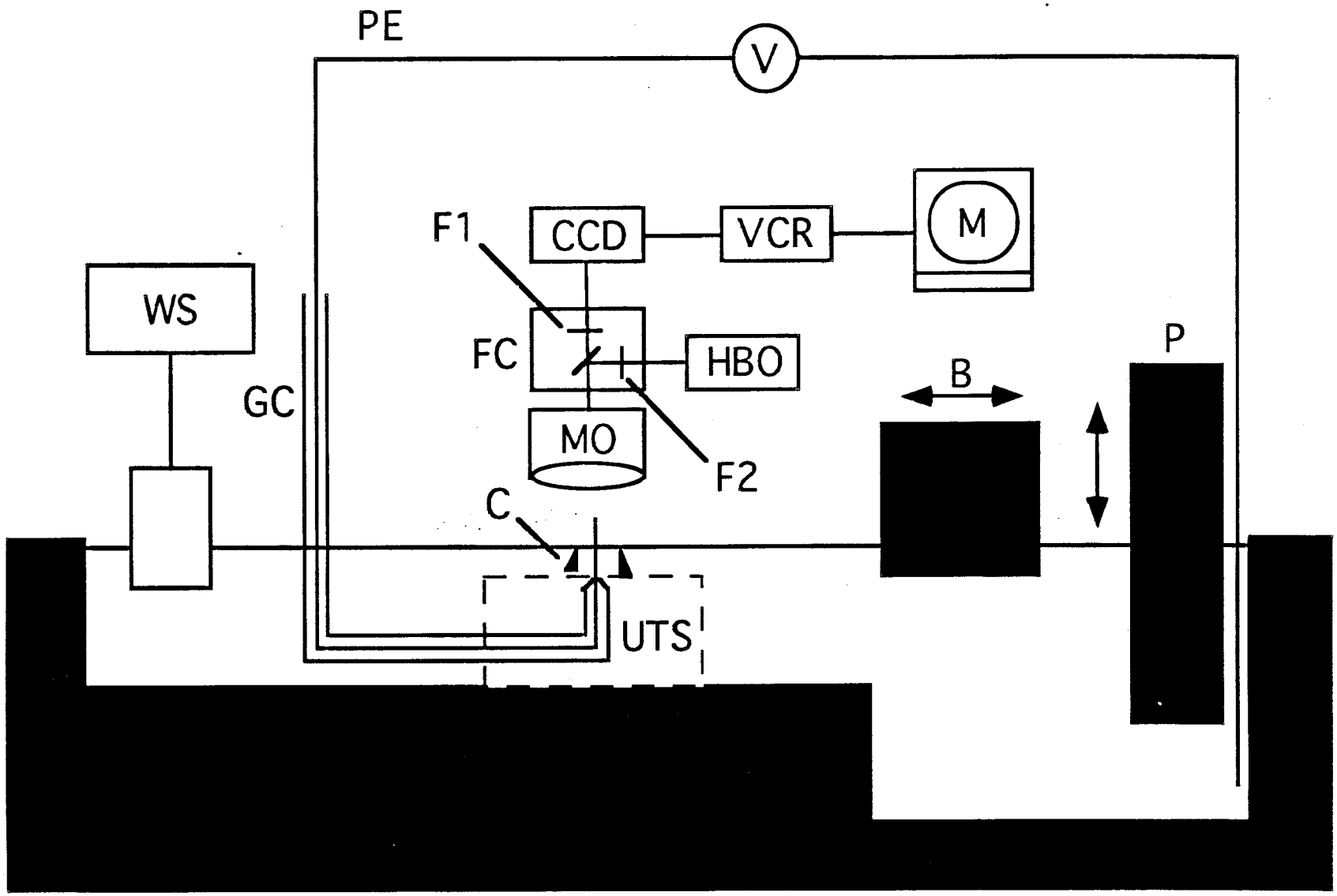

FORMATION OF LARGE DOMAINS

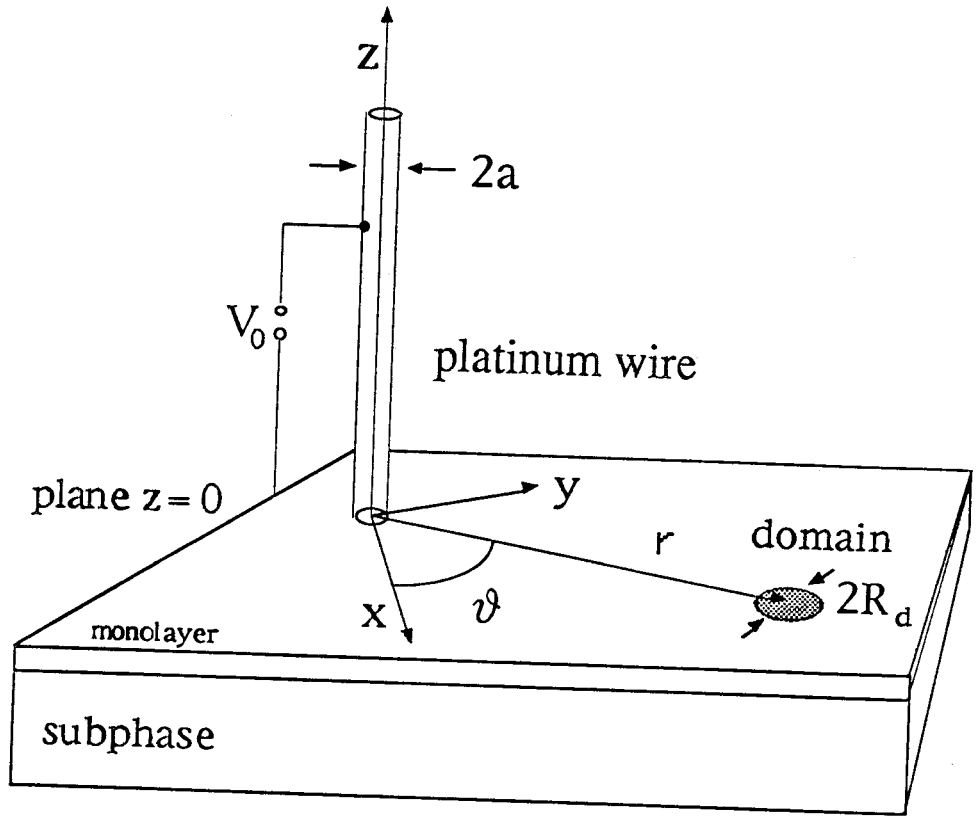

- Lipid domains in a drift-free environment exposed to an electric field
- –ve polarity: attraction of DChol-rich domains –> fusion
- +ve polarity: repulsion of large domain formed

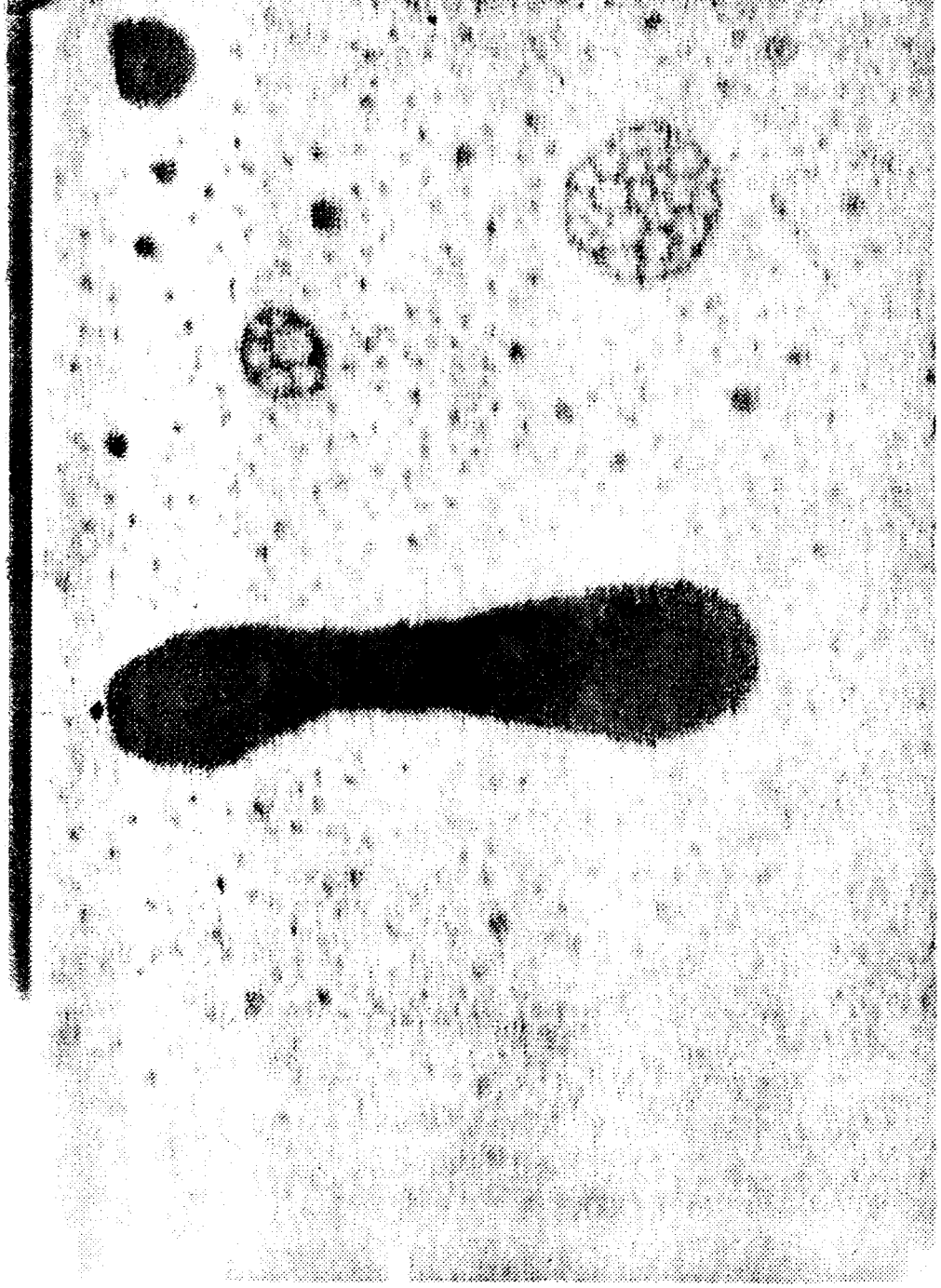

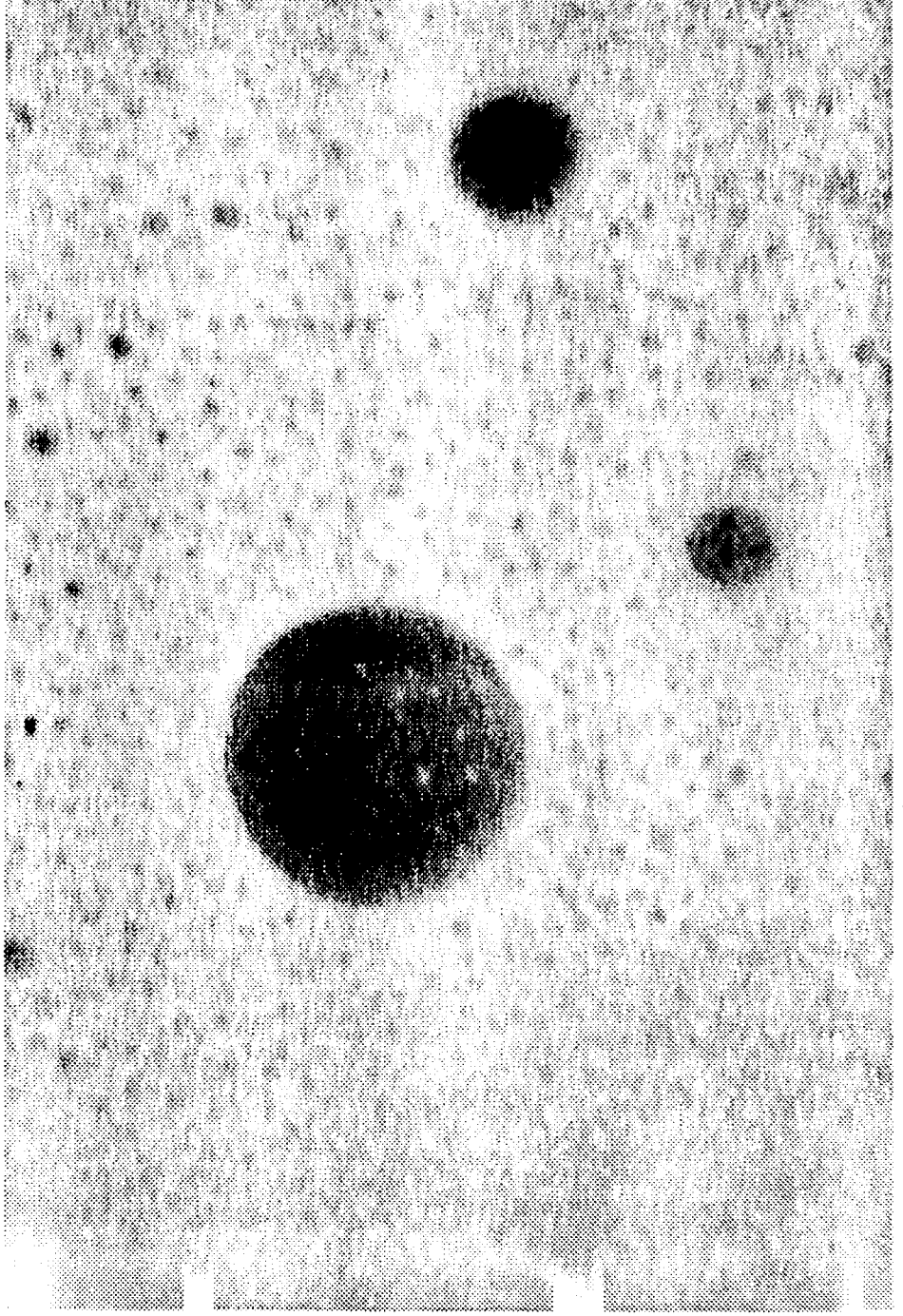

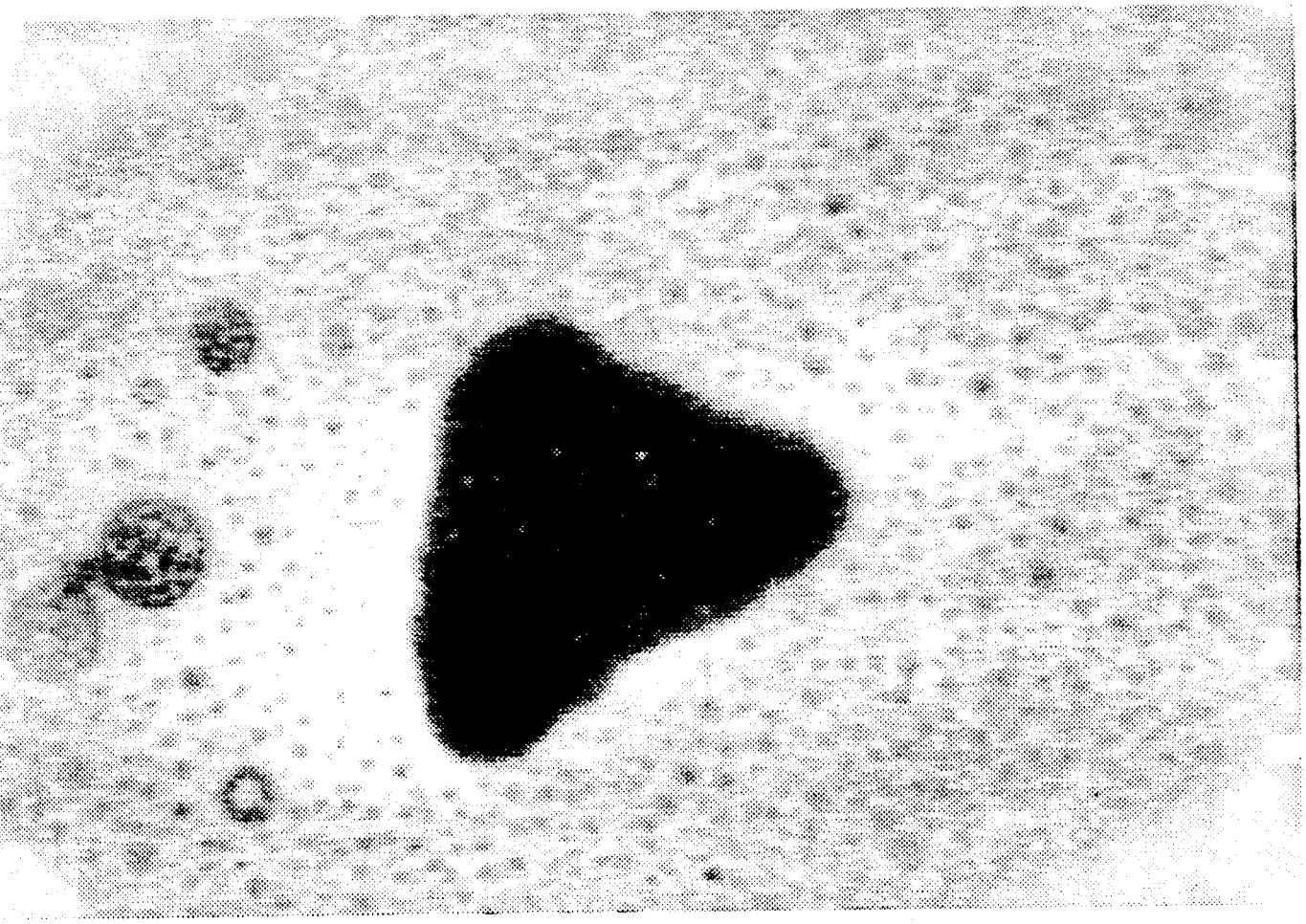

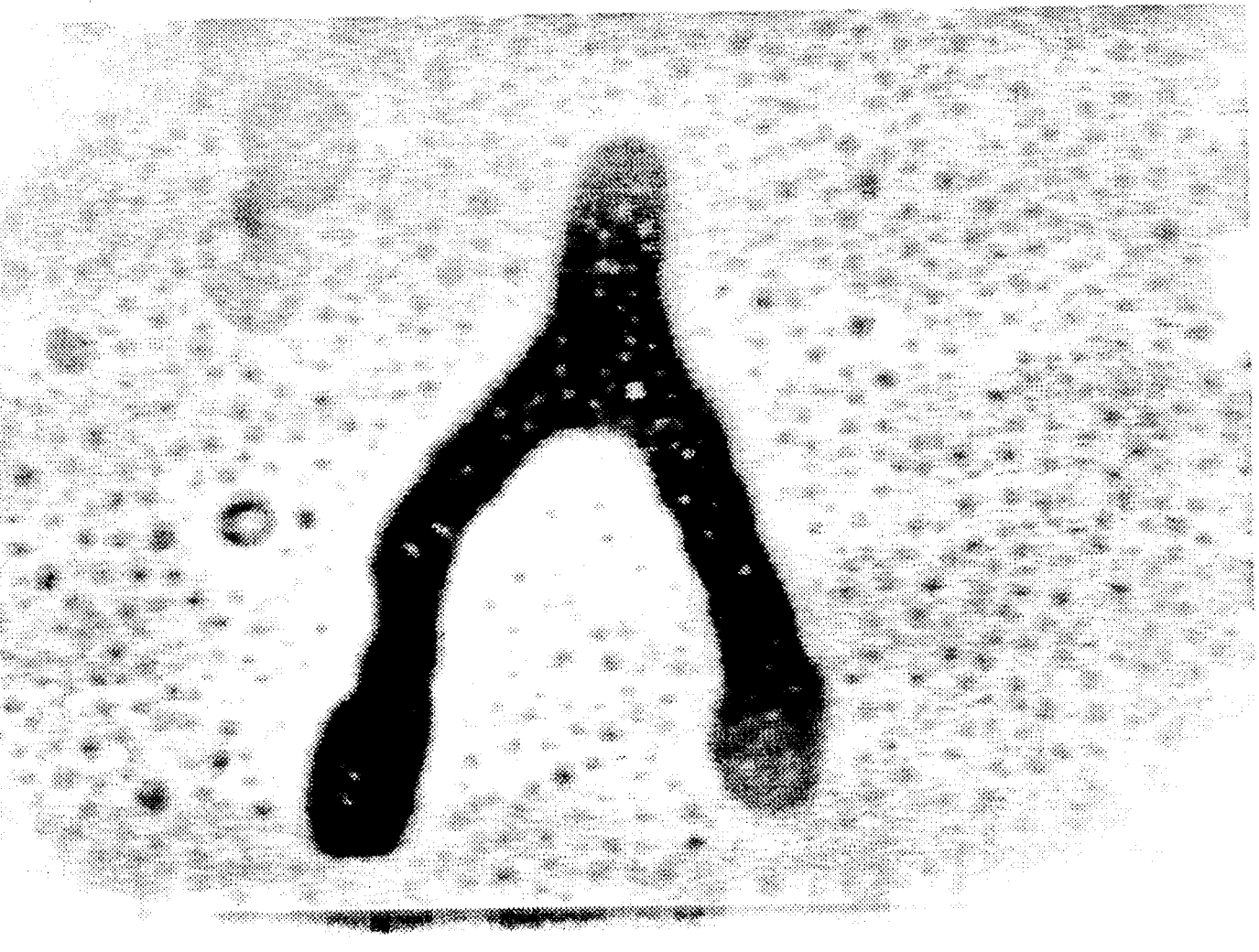

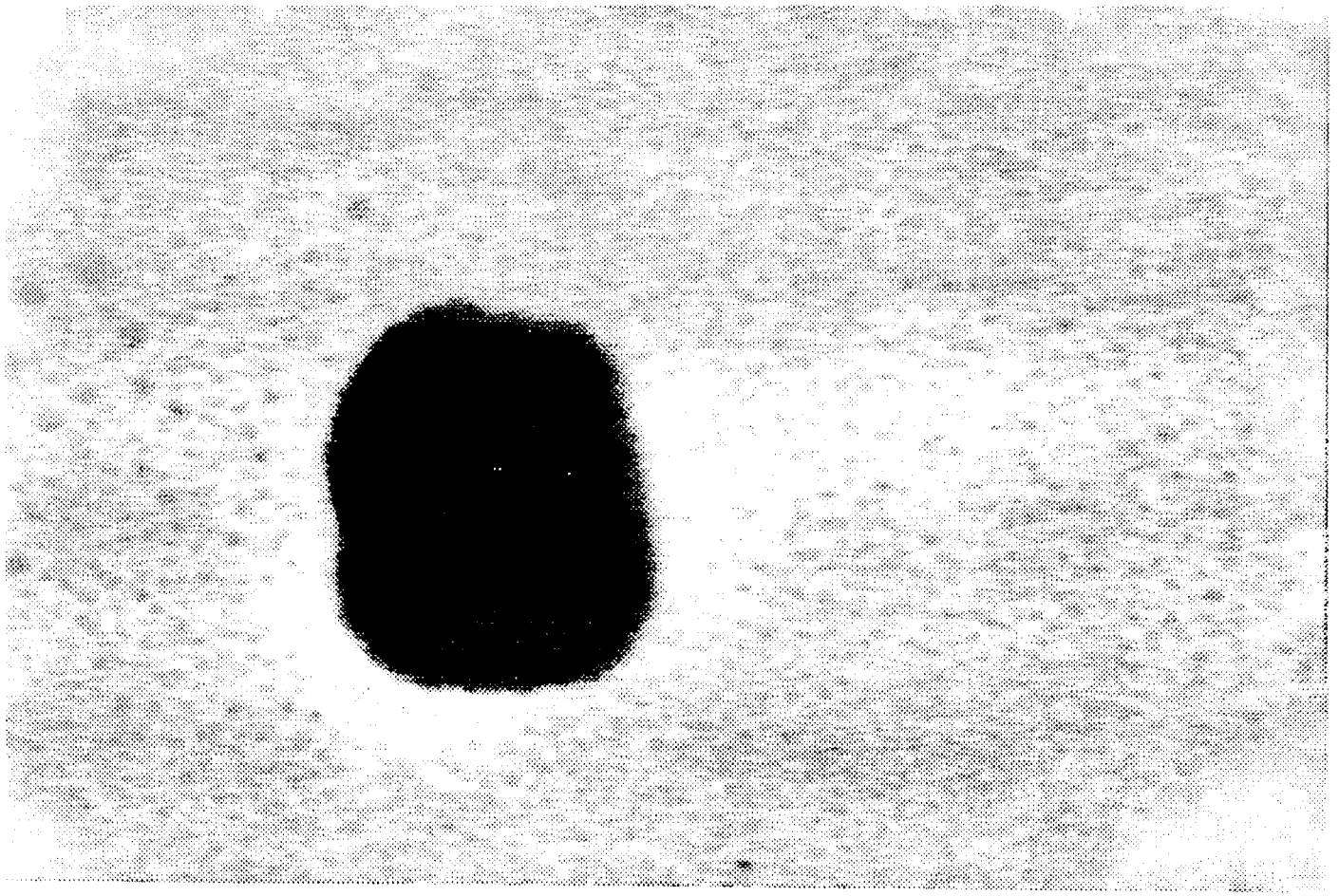

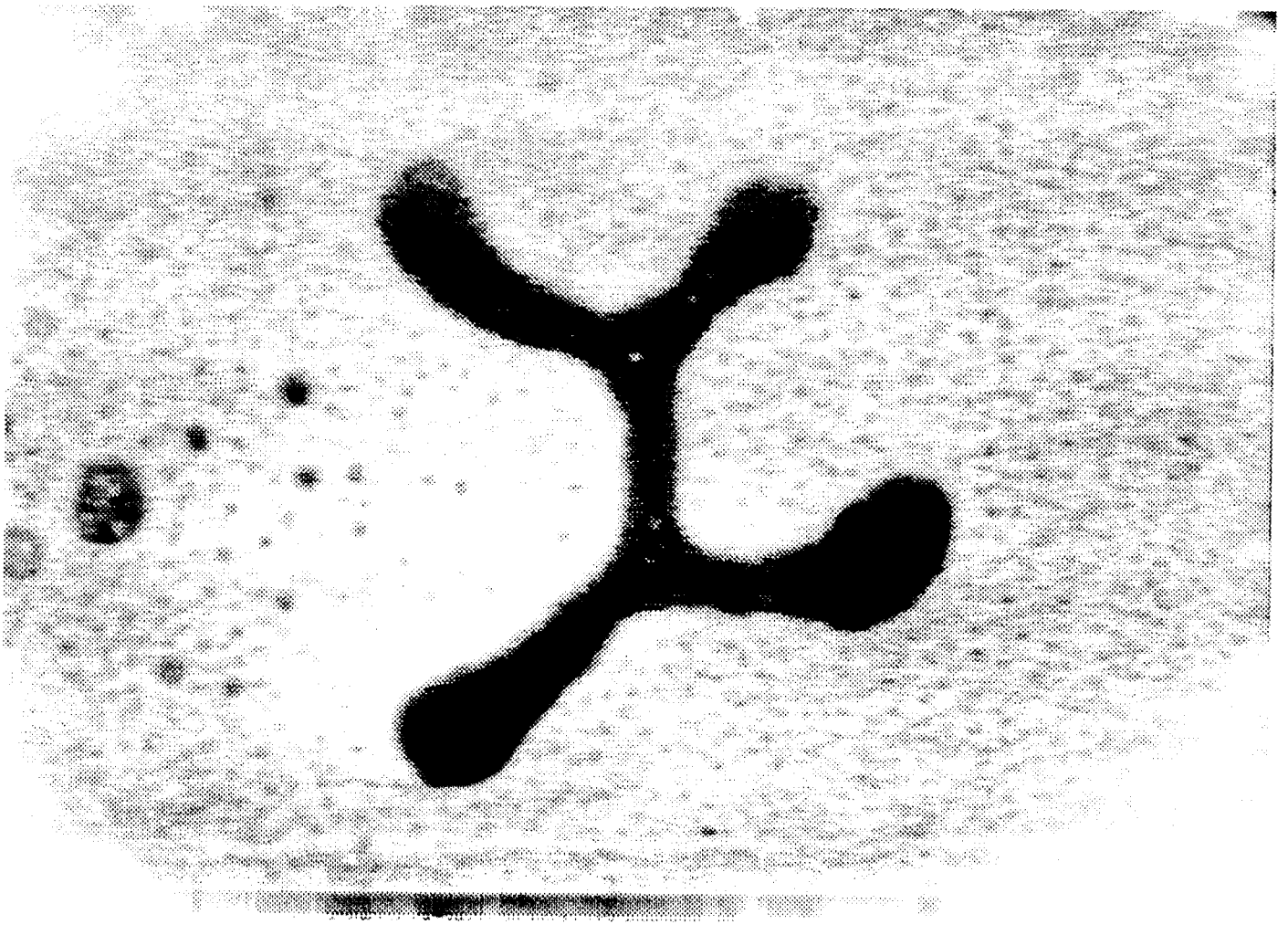

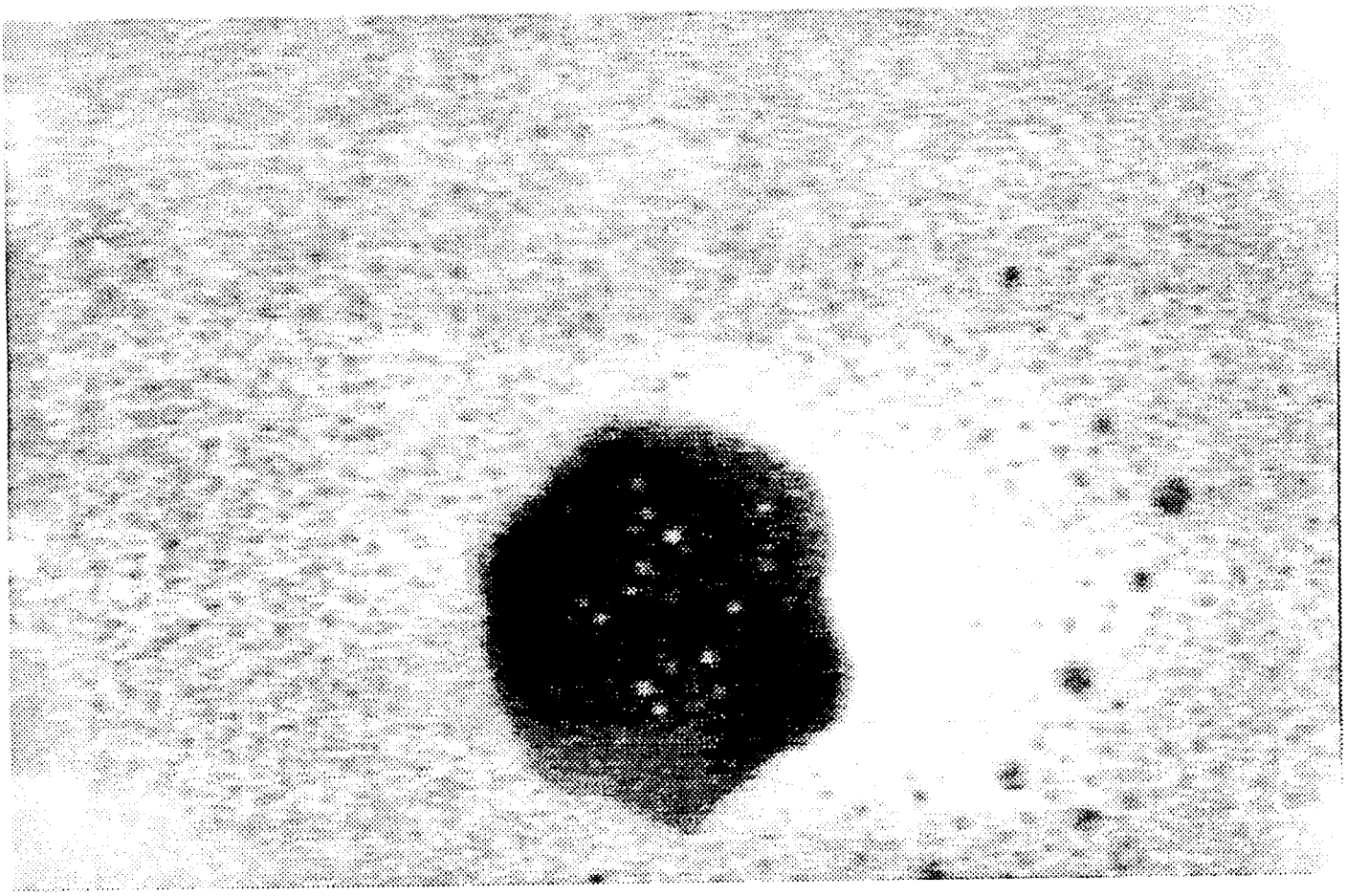

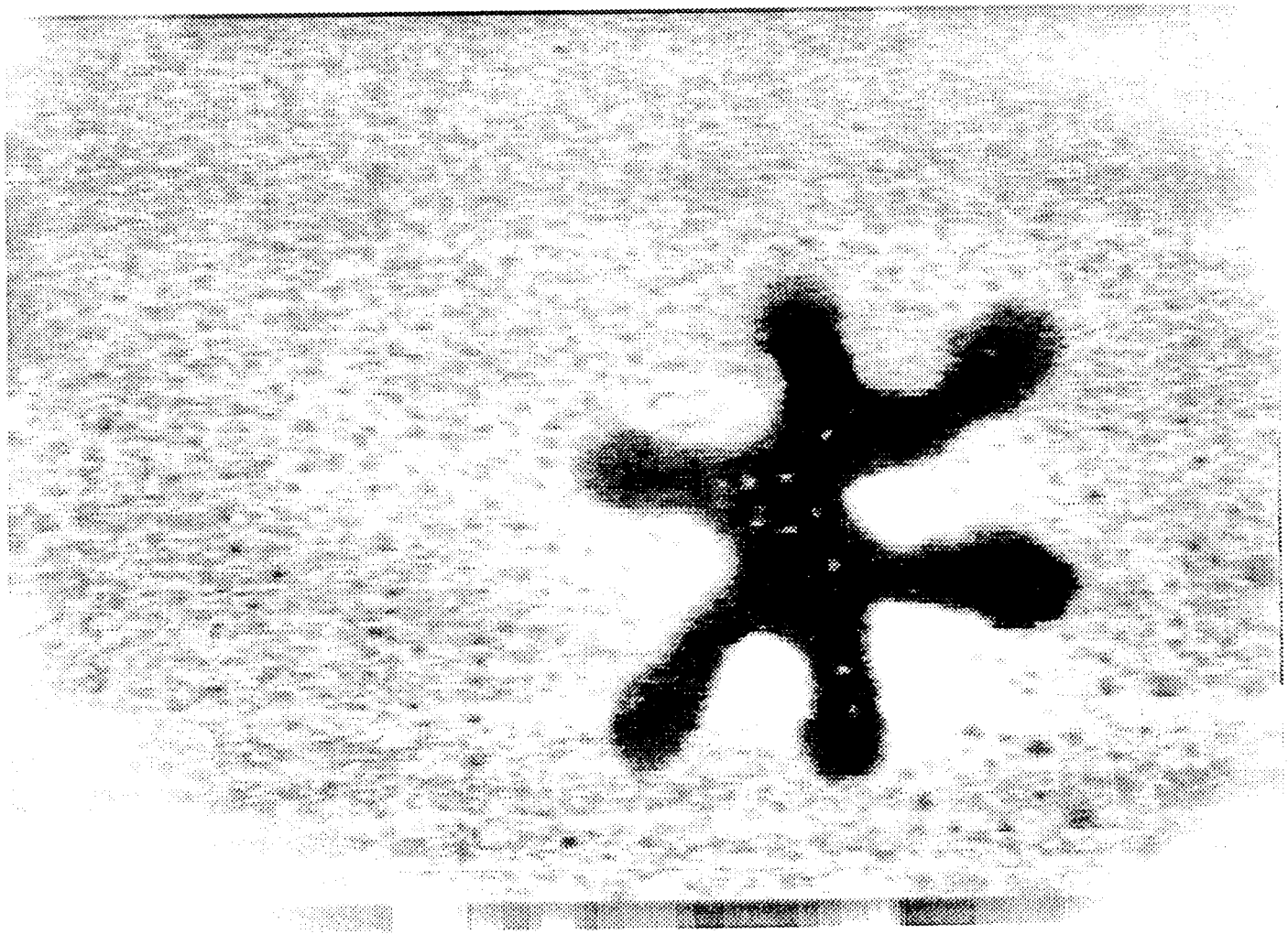

QUANTITATIVE EXPERIMENTAL RESULTS

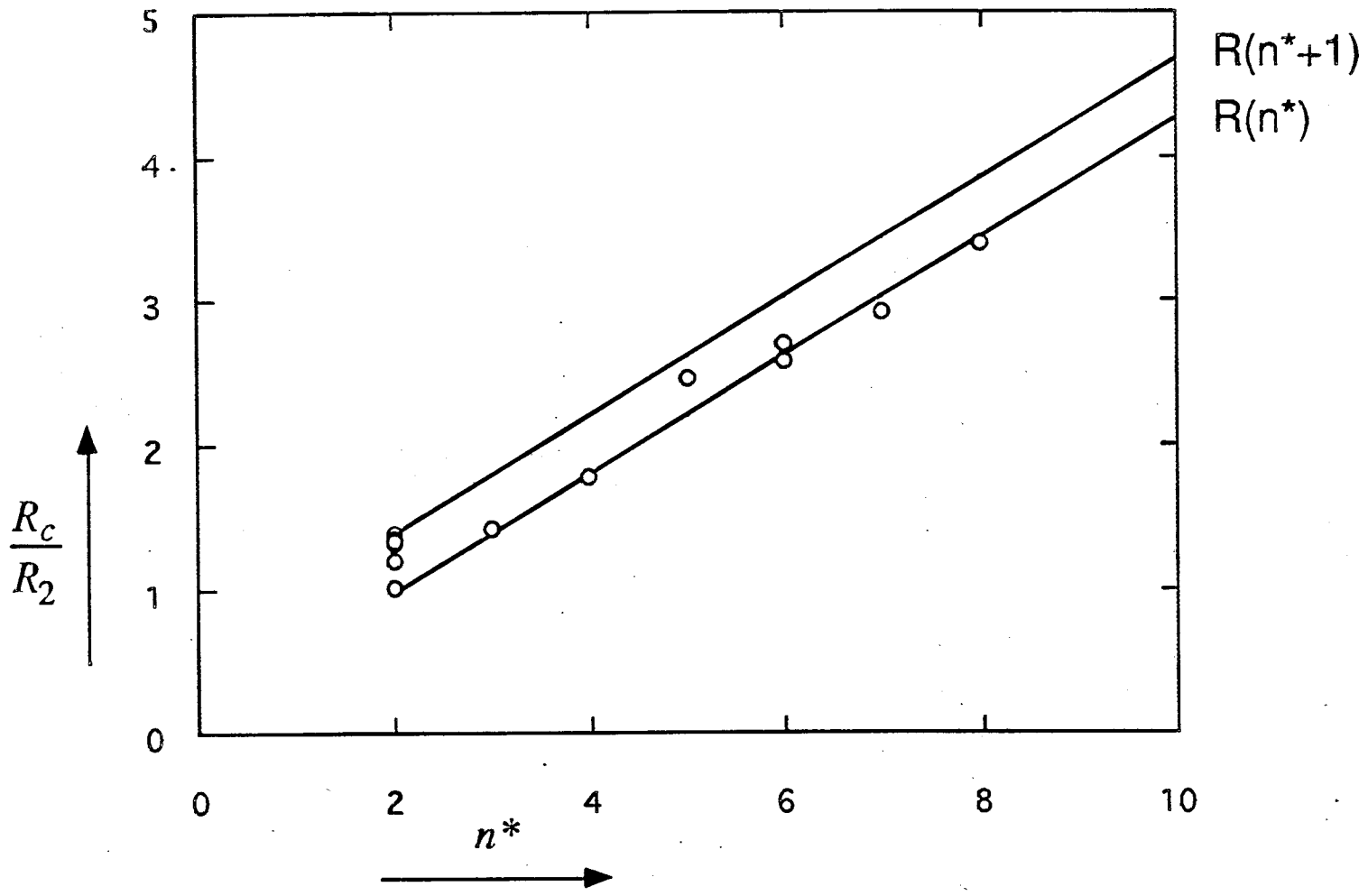

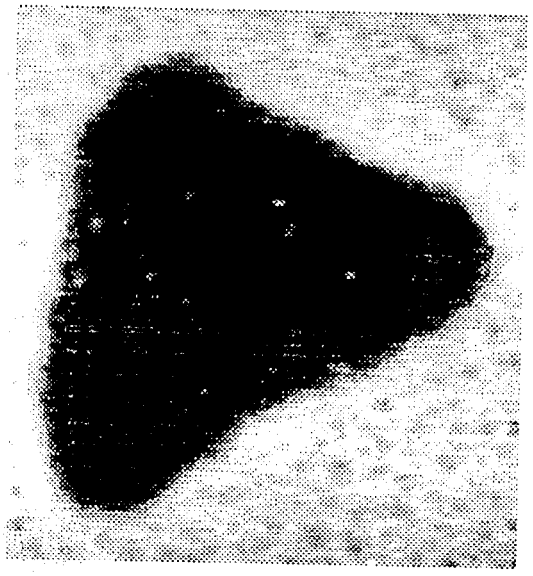

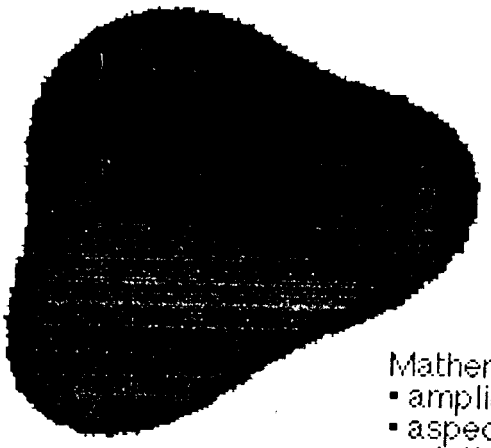

Mathematica version:
- amplitude 0.17
- aspect ratio: 1.3
- rotation left: 120°
- scaled down by 70%

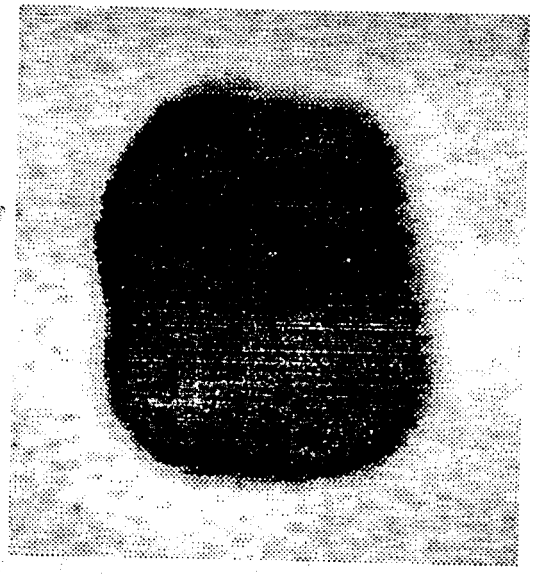

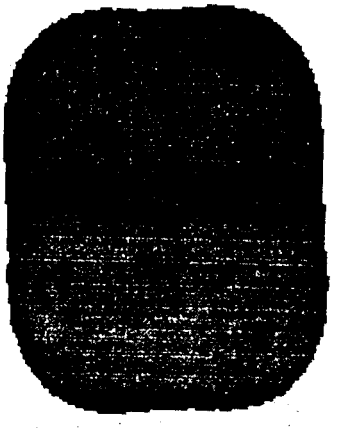

Mathematica version:
- amplitude: 0.085
- aspect ratio: 1.3
- rotate left: 3°
- scaled down by 57%

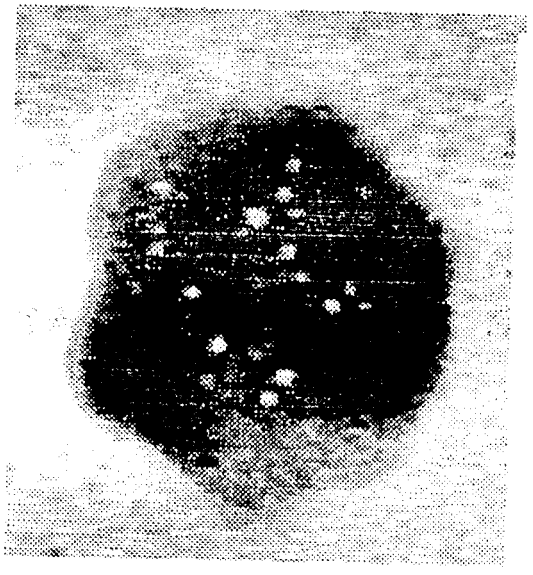

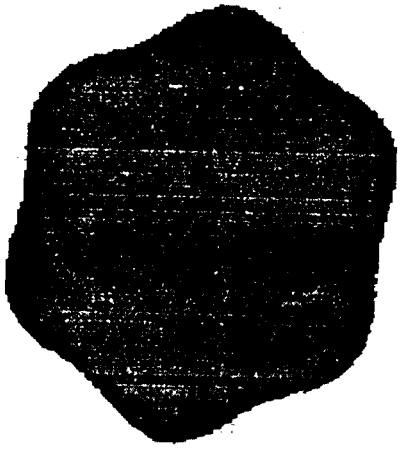

Mathematica version:
- amplitude: 0.07
- aspect ratio: 0.82
- rotate right: 98°
- scaled down by 63%

50µm

Figure 14

Line Tension

Benvegnu & McConnell, JPC (92) 96, 6820

Brownian Motⁿ

Klingler & McConnell, JPC (93) 97, 6096

Field-gradient

Klingler & McConnell, JPC (93) 97, 2962

Field induced core-grad.-expt

Lee, Klingler, McConnell

Science (94) 263, 655

Field induced core grad-theory

Lee & McConnell

BPJ (95) 68, 1740

Shape Transitn

Lee & McConnell

JPC (93) 97, 9532

Bleeding for Serum

- take blood, invert bottle w/ anticoagulants
- wash & pack cells 4x using diff. centrifuge speeds
  - dump blood in 50 ml tube (⅓)
  - fill 2 150 mM NaCl
  - spin @ 4°C 3 x 3000 rpm (5 min)
    1 x 6500 rpm " "
  - Suck out yellow liquid
- 5mM PBS → 5 min on ice
  - → lyse cell
  - → remove hemoglobin
- spin hard - 20-23K x g for 10-15 min
  - discard supernatant
  - Refill + resuspend

- Pipette membrane out
- add 1:2 $CHCl_3$: MeOH
  vortex violently
- take out E pipette.
  evaporate solvent under argon
  put in freezer under argon (-20°C)
- TLC plate

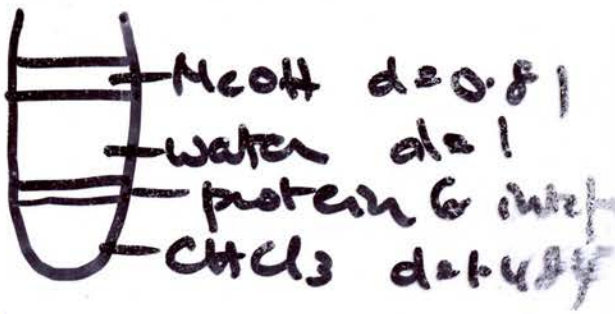

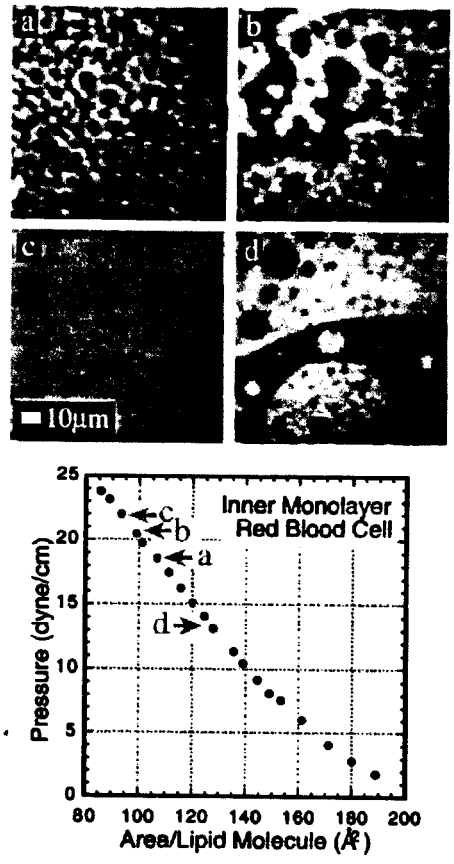

FIG. 1. Top: Epifluorescence micrographs of a monolayer simulating the erythrocyte membrane inner leaflet (Table I, expt 1) as it is laterally compressed at an air-water interface at room temperature (23 °C). At surface pressures below 1 dyn/cm (or mN/m), gas and liquid phases coexist (not shown). As the monolayer is compressed further, immiscible liquid phases appear. (a) 18.5 dyn/cm: 5–10 μm circular domains of dark, liquid phase within a bright, liquid phase. Domains exhibit Brownian motion. (b) 20.8 dyn/cm: fingering characteristic of critical point behavior. (c) 21.9 dyn/cm: homogeneous liquid. (d) 13.2 dyn/cm: circular domains reappear as the surface pressure decreases. Bottom: the pressure vs area/molecule isotherm is similar to those of cholesterol-phospholipid lipid monolayers [3]. Area/molecule errors are estimated to be less than a factor of 2. Errors in pressures are ±1 dyn/cm throughout. Experiments are standard [14] and concluded within ~10 min to minimize air oxidation. Because of this time constraint, it is virtually impossible to observe an inflection point in the isotherm near the critical point (point b). Even under ideal conditions, the inflection point is difficult to detect [3].

same critical pressure π_{13} as the binary mixture of 2 and 3, π_{23}. Joining these binary critical points is a calculated *line* of critical points. Thus critical properties hold for substantial variation in lipid composition along this critical line. A lipid mixture of $n > 3$ components with interactions described by Eq. (1) has an $n - 1$ dimensional surface of critical points. In this theoretical scenario,

TABLE I. Molar lipid compositions were mixed to approximate the compositions of the inner and outer leaflets of the red blood cell membrane. Concentrations are given for cholesterol (Chol), the four other major lipid species [sphingomyelin (SM), phosphatidylcholine (PC), phosphatidylethanolamine (PE), and phosphatidylserine (PS)], glycolipids (Gly), and the fluorescent probe Texas Red-DMPE (dimyristoylphosphatidylethanolamine). (See Ref. [15].) Experiments 1, 2, 3, and 4 displayed critical pressures, π_c (dyn/cm or mN/m) as in Figs. 1 and 2. Of these, experiments 1 and 4 were best estimates of the inner and outer red blood cell leaflet compositions. Experiments 2 and 3 were variations on the inner leaflet 1. Experiments 5 through 10 were variations on the outer leaflet 4. These six exhibited immiscible liquid phases and a transition at high pressure (>20 dyn/cm) to a homogeneous liquid, but no fingering or stripe phase (No). Lipids extracted [16] from the red blood cell membrane but not yet separated by headgroup contained the sum of all the cholesterol and the four major lipid species of the inner and outer leaflets, with no glycolipids. Monolayers of this "total" mixture also exhibited immiscible liquid phases and a transition at high pressure (>15 dyn/cm) to a homogeneous liquid, but no critical behavior.

Expt	Chol	SM	PC	PE	PS	Gly	TR	π_c
Inner red blood cell leaflet								
1	46.2	5.3	7.4	28.4	12.5	0	0.2	22
2	40.9	5.8	8.1	31.2	13.8	0	0.2	25
3	51.5	4.8	6.7	25.6	11.2	0	0.2	23
Outer red blood cell leaflet								
4	43.4	22.5	23.4	6.3	0	4.2	0.2	29
5	45.3	25.7	26.7	2.1	0	0	0.2	No
6	40.4	28.0	29.1	2.3	0	0	0.2	No
7	36.1	29.9	31.2	2.6	0	0	0.2	No
8	32.9	31.9	33.2	1.8	0	0	0.2	No
9	25.3	35.2	36.5	2.8	0	0	0.2	No
10	82.1	4.6	4.8	0.4	0	7.9	0.2	No

critical behavior is sensitive to cholesterol concentration and relatively insensitive to substantial variations in phospholipid composition (cf. Table I).

Figure 3(b) gives a theoretical phase diagram for a binary mixture of components 1, 3 or 2, 3. Superimposed on this phase diagram are the superstructure phases H and S. The hexagonal (H) and stripe (S) phases have length scales D set by a competition between long-range intermolecular dipolar repulsions and interdomain line tension λ.

$$D \approx d e^{\lambda/m^2}. \tag{3}$$

Here m is the difference in dipole density in the two phases and d is of the order of a nearest neighbor intermolecular distance. Near the critical point the widths of the stripes are equal to $de(\pi/2)e^{\lambda/m^2}$ [4]. The line tension λ and the dipole energy difference term m are related to the pressure difference $(\pi - \pi_c)$ by critical exponents $\mu \approx 1$ and $\beta \approx 0.25$, respectively [14,17,18]. Hence, as π approaches π_c, D decreases. D is the stripe width or circular domain radius. Indeed, in a binary mixture of cholesterol and phosphatidylcholine, we have observed that the stripe width approaches zero as the surface

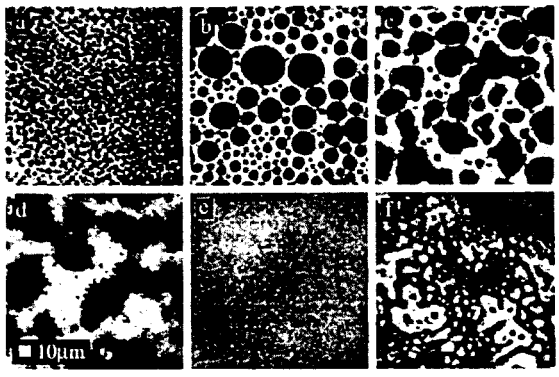

FIG. 2. Epifluorescence micrographs of a lipid monolayer simulating the erythrocyte membrane outer leaflet (Table I, expt 4). The phases and isotherm are similar to Fig. 1. (a) 12.1 dyn/cm (or mN/m): circular liquid domains <10 μm. (b) 26.1 dyn/cm: coalescence of domains. (c) 28.4 dyn/cm: fingering characteristic of critical point behavior. (d) 29.1 dyn/cm: critical point. (e) 34.5 dyn/cm: homogeneous liquid. (f) 28.8 dyn/cm: immiscible liquid phases reappear as pressure decreases. The domains exhibit fingering characteristic of proximity to a critical point. At lower pressures, the domains are circular.

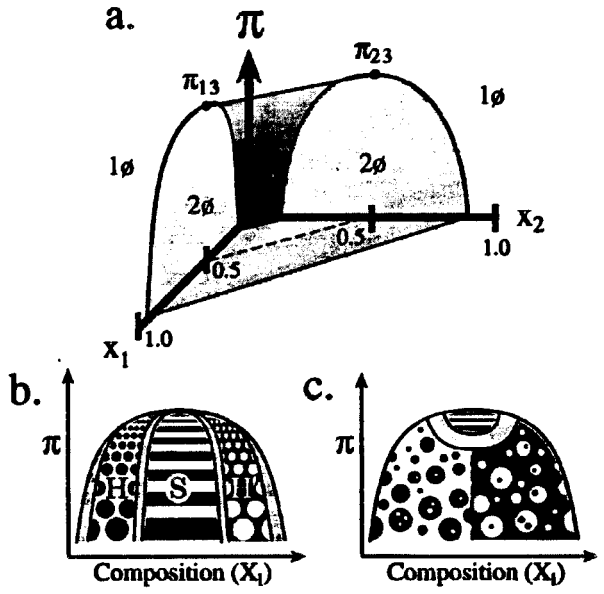

FIG. 3. (a) Schematic ternary phase diagram with mole fractions X_1, X_2, and X_3, where $X_1 + X_2 + X_3 = 1$. Components 1 and 2 are phospholipids and 3 is cholesterol. At pressures $\pi < \pi_{13} = \pi_{23}$, two immiscible liquid phases (2ϕ) coexist under the surface shown. Above this surface, there is one homogeneous liquid phase (1ϕ). In this model, all pure components are assumed to have equal chemical potentials μ_i^0, and surface areas, with area contraction parameters $\alpha_{13} = \alpha_{23}, \alpha_{12} = 0$. Binary phase diagrams for 1,3 and 2,3 appear above the X_1 and X_2 axes. Both pairs are assumed to have equal critical pressures $\pi_{13} = \pi_{23}$. A line of critical points connects the two binary critical points. (b) Schematic theoretical phase diagram of cholesterol-phospholipid binary mixture. Below the critical pressure and within the two phase region three superstructure morphologies are expected, two hexagonal phases (H and H') and a stripe phase (S) [31]. The boundary between the stripe phase and the hexagonal phase is adapted from [32]. Coexistence regions of adjacent phases are in grey. The equilibrium widths of the stripes and the radii of circles depend on the proximity to the critical point, as sketched. (c) Schematic experimental phase diagram of cholesterol-phospholipid binary mixture. Stripes are observed only within a few dyn/cm of the critical point [19]. At lower surface pressures, domains are primarily black circles on a white background or reversed. Fingering is observed in the grey region, at the transition between circular domains and stripes.

pressure is raised to the critical pressure. As the critical pressure is approached from below, preexisting circular domains show fingering and then transform to the stripe phase when the composition is close to the critical composition (data not shown). At low monolayer pressures $\lambda \approx 1.8 \times 10^{-7}$ dyn and $m^2 \approx 10^{-8}$ cgs esu and D is extremely large [18]. Theoretically, at equilibrium a stripe phase should appear over a large region of the phase diagram [Fig. 3(b)]. In contrast, stripe phases are experimentally observed only within 1–2 dyn/cm of the critical point [Fig. 3(c)] [19]. This is related to the fact that the rate of domain size equilibration is slow and that stripes produced experimentally are limited in length [20]. In our experience, these conclusions apply equally well to multicomponent mixtures. Figure 3(c) illustrates the experimental relations between circular domains, fingering domains, and the stripe phase.

The erythrocyte lipid bilayer may be near a critical point since stripe phase fingering is observed in erythrocyte lipid monolayers at comparable molecular densities. We observe critical behavior at molecular areas of ~60 Å^2 for the simulated erythrocyte outer leaflet and ~100 Å^2 for the inner leaflet. (A transition from two liquid phases to one liquid phase is found at ~40 Å^2 for the total lipid mixture.) Uncertainties in these areas due to the chemical assay used [21] are estimated to be less than a factor of 2. The average area of a lipid in an erythrocyte membrane of a phospholipid bilayer is comparable, ~40 or ~60 Å^2, respectively [22,23].

Additional comparison between monolayers and the erythrocyte membrane is provided by the work of Demel *et al.* [24]. These investigators compared the activity of phospholipases on erythrocyte membranes to their activity on lipid monolayers at various pressures. They concluded that a monolayer pressure between 31 and 34.8 dyn/cm yields a susceptibility to this lipase activity equivalent to the susceptibility of erythrocyte membranes to lipase activity. This surface pressure is slightly higher than the pressure at which we observe critical behavior in the simulated inner and outer red blood cell leaflets.

The proximity of red blood cell lipids to a liquid-liquid immiscibility critical point should play a significant role in the cellular physical properties. For example, theoretically, membrane lipid composition and curvature

FOLDING TRANSITIONS ALSO OBSERVED IN PURE PHOSPHOLIPID SYSTEMS

DPPG

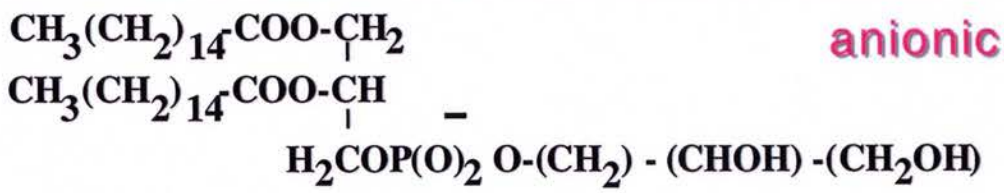

anionic

DPPE

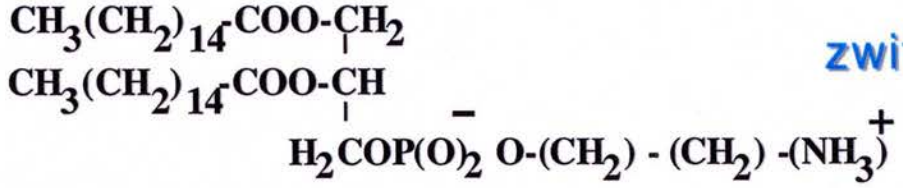

zwitterionic

Both have comparable head-to-tail ratio and collapse via folds in 2 mM Ca^{2+}, 150 mM NaCl, 0.2 mM $NaHCO_3$, pH 6.9

DPPC

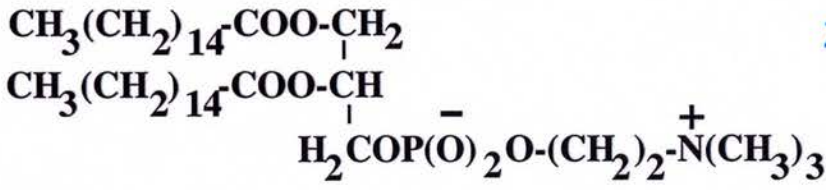

zwitterionic

DPPC has a large head compared to the tails and does not form folds under any experimental condition

Can we make DPPC form folds like DPPG and DPPE by adding another surfactant to DPPC?

STRATEGY

What can be the cause for the folding transition?

- Both DPPG (anionic) and DPPE (zwitterionic) fold
  -> electrostatics cannot be the controlling factor

- In some systems, folds are observed on pure water subphase, they do not occur when 150 mM NaCl is added, but reoccurred when small amount of divalent ions are added
  -> divalent ions may act to dimerize the lipids, helping them pack tighter

- The main difference between DPPG or DPPE and DPPC is the presence of the head/tail size mismatch in DPPC
  -> the ability to pack tightly may allow the film to have enough rigidity for the folding transition

To rectify the head/tail size mismatch in DPPC

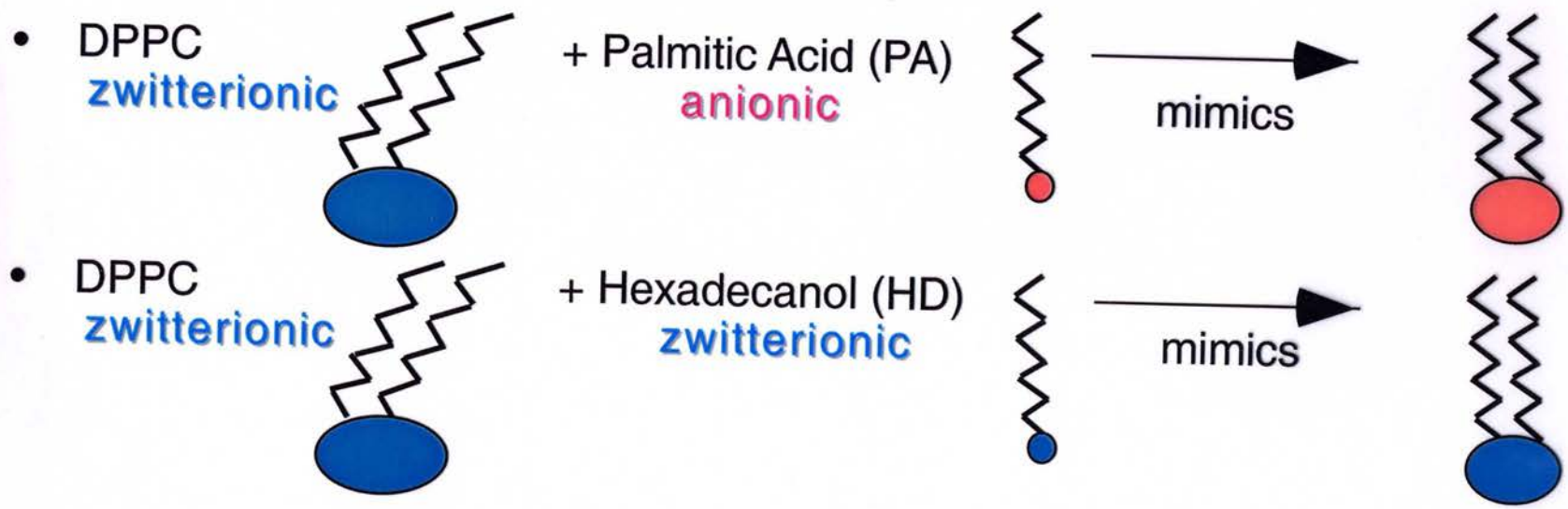

ISOTHERMS OF BINARY MIXTURES AT 30° ON PURE WATER

DPPC/PA

DPPC/HX

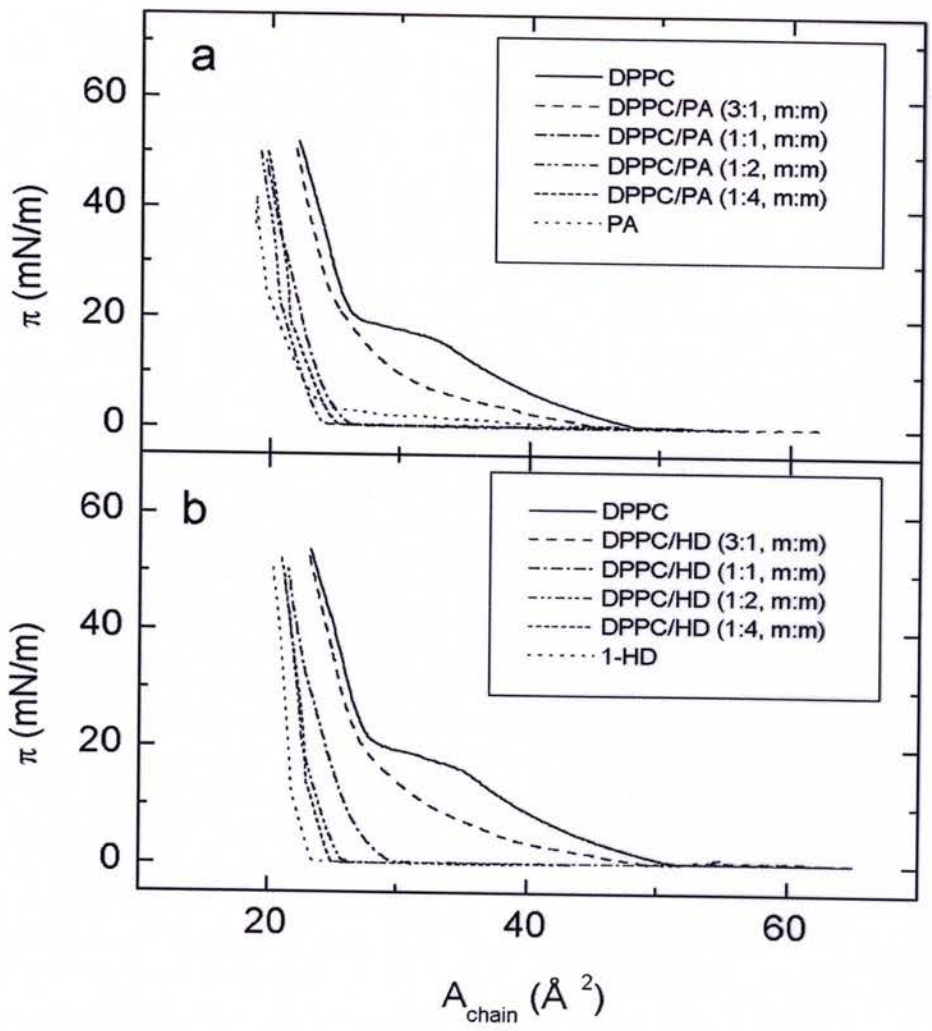

Folding does occur in some of these mixed binary systems!

Synchrotron X-ray Expt

High Intensity

- SLAC
- ANL (APS)
- ALS
- BNL
- ESRF
- DESY
- Berlin
- ⋮

$\lambda \sim 1.3$ Å

Incident angle $\alpha_i = 0.11^\circ = 0.85\,\alpha_c$

- total ext. reflection
- evanescent wave
- max surface intensity

Large footprint

- 5 mm x 50 mm
- 1 mm x 50 mm

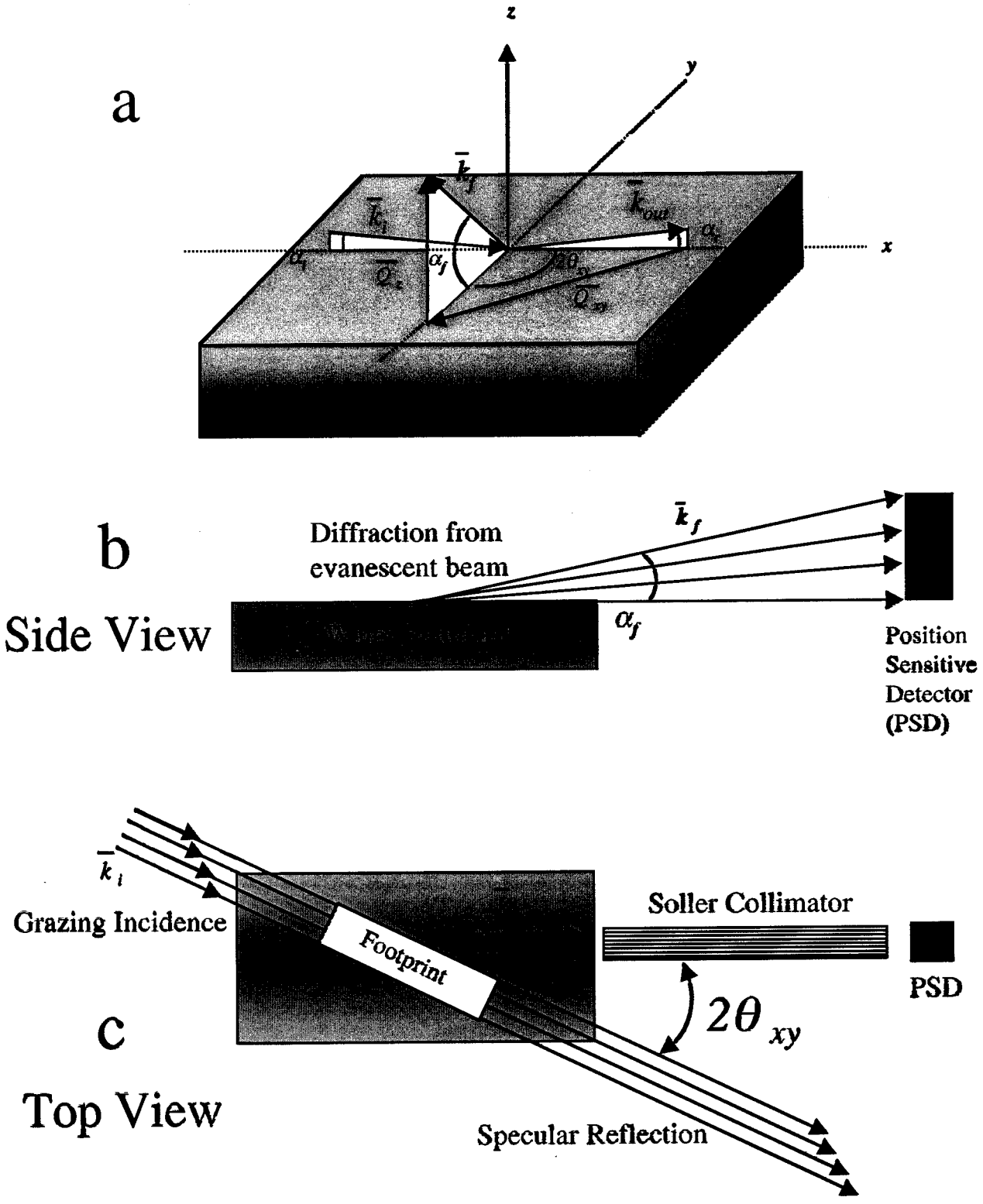

169 Expt setup

Fig. 2 (Ka Yee C. Lee et al.)

170

Grazing Incident Diffraction (GIXD)

3D : Bragg spots

2D : Bragg rods

(Lack of vertical crystalline repeat)

$$Q_{xy} \sim \frac{4\pi}{\lambda} \sin\frac{2\theta_{xy}}{2}$$

Bragg peak → ∫ over Q_z

Bragg rod profile → ∫ PSD channel

d spacing of 2D lattice

$$d = \frac{2\pi}{Q_{xy}}$$

Line shape of peak

2D coherence Length . L

Intensity distribution along Bragg rod

direction + mag of molec. tilt.

out of plane coherence L_c

surface roughness

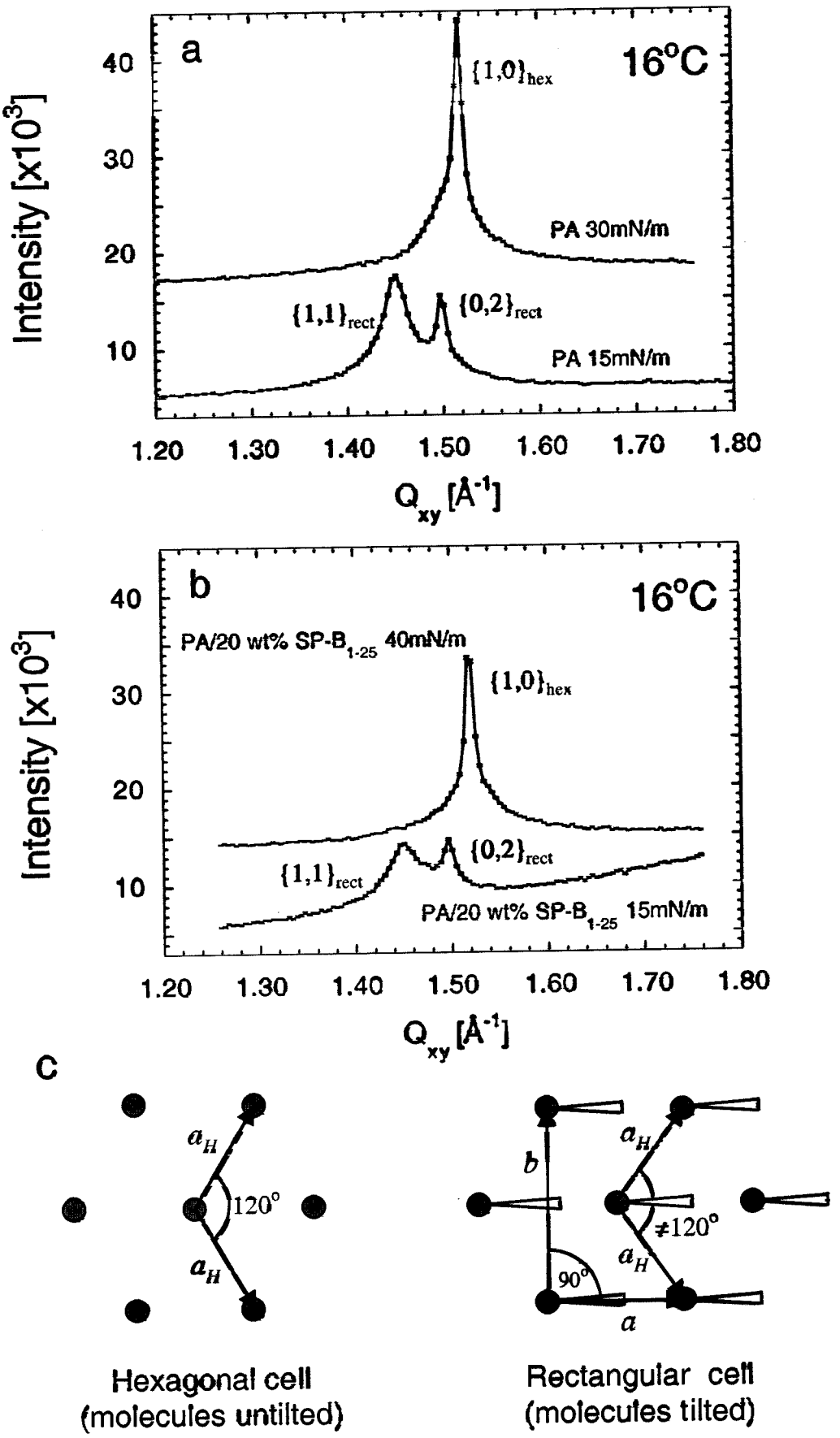

Fig. 3 (Ka Yee Lee et al.)

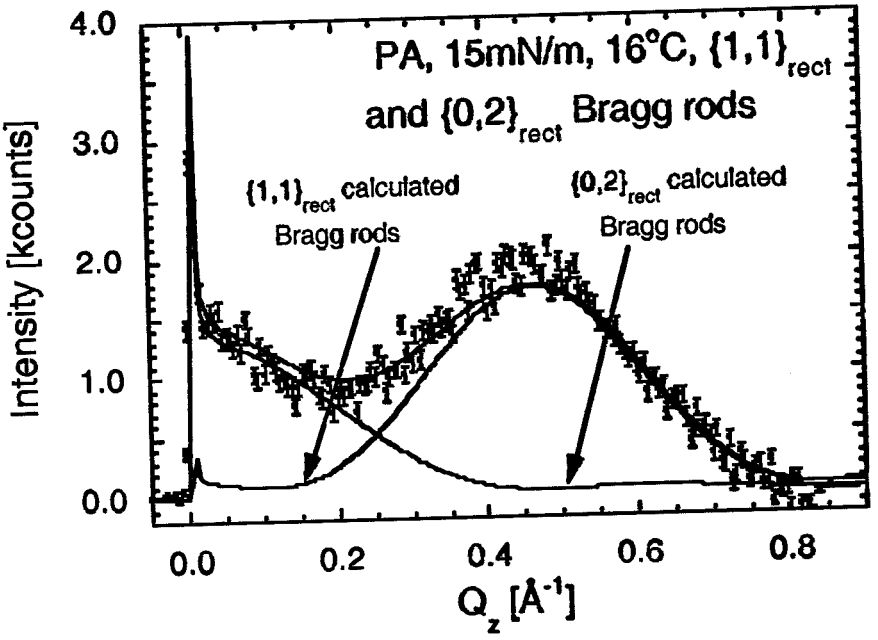

Fig. 4 (Ka Yee C. Lee et al.)

PA/SP-B$_{1-25}$ ON PURE WATER @ 16 °C - GIXD DATA

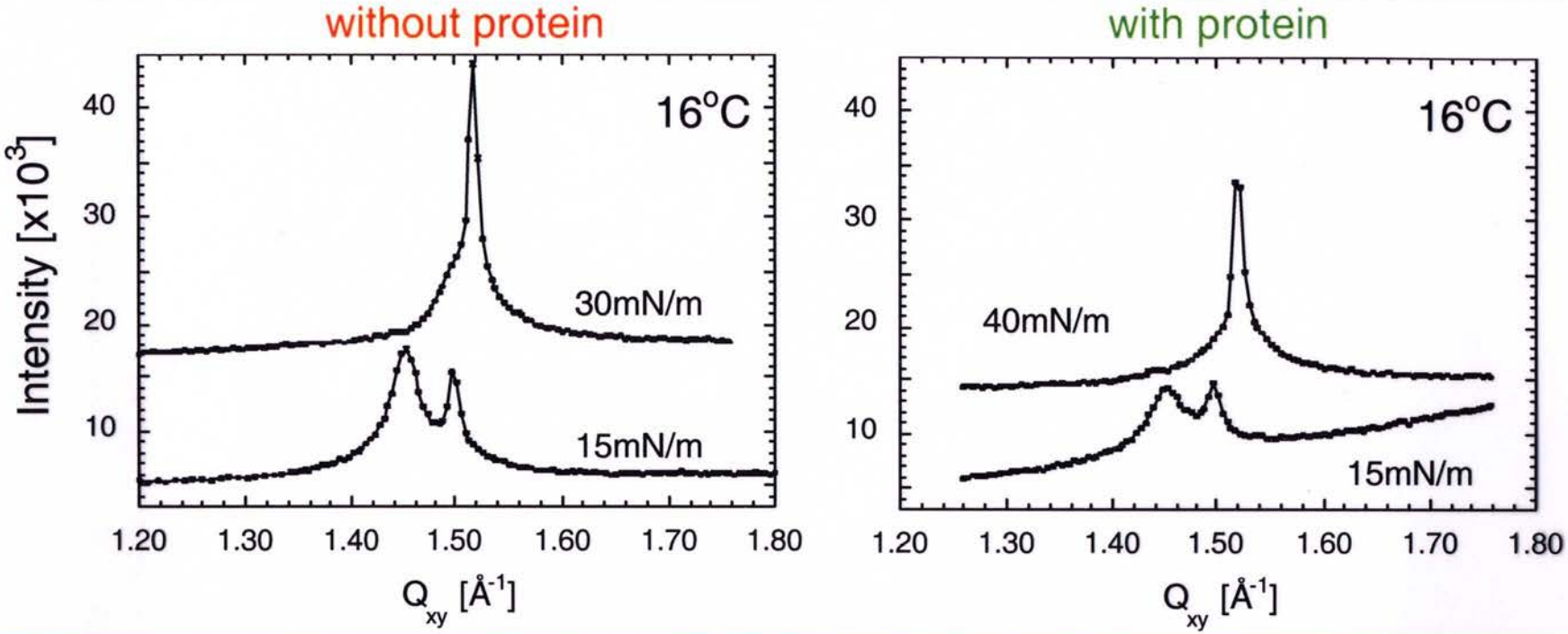

	Observed d-spacing (Å)	Area per molecule (Å^2)	Unit cell axis (Å)	Coherence length (Å)
PA 15 mN/m)	d11=4.33	21.2	a=5.06	L11=155
	d02=4.19		b=8.38	L02=447
PA/SP-B (15 mN/m)	d11=4.33	21.2	a=5.06	L11=129
	d02=4.20		b=8.40	L02=425
PA (30 mN/m)	4.14	19.8	4.78	468
PA/SP-B (40 mN/m)	4.13	19.7	4.77	451

- Reduction in scattering intensity in the presence of protein is due to the creation of a disordered phase in the surface film (agrees with microscopy results)
- Protein resides in the disordered phase

essentially identical for both the cases with and without protein

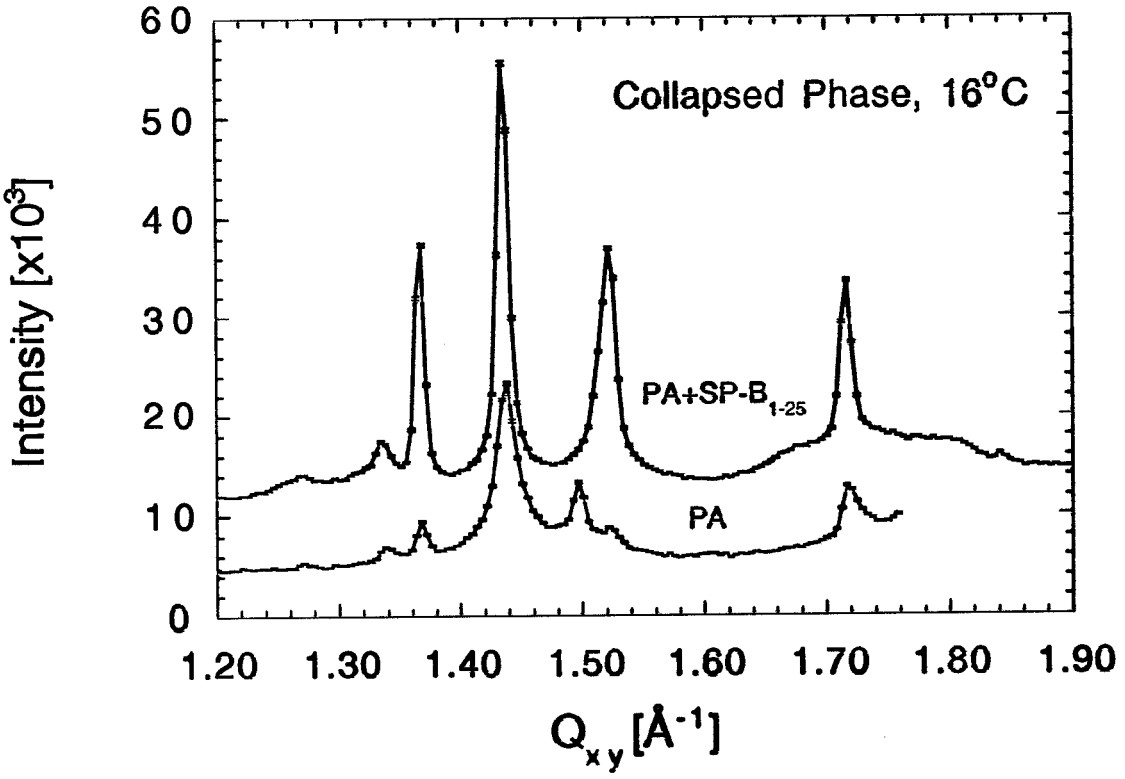

Fig. 10 (Ka Yee C. Lee et al.)

X-ray Reflectivity (XR)

Electron density distribution in the direction normal to the interface

Analysis using slab model

Each slab → const. e^- density & thickness

Interface → smeared out z gaussian f(z). of std. deviation σ

Unit Cell

$$\frac{1}{|a|^2} = \frac{1}{d_H^2} + \frac{1}{(2d_{02})^2}$$ rectangular

$$a_H = \frac{d}{\cos 30^\circ}$$ hexagonal

Orthorhombic : 2 molecules / cell

chains in herringbone structure

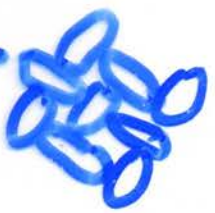

Triclinic : 1 molecule / cell

174
175 SFB/IR XR
176 Munich of SFB/P1

PA/SP-B1-25 ON PURE WATER @ 16 °C - X-RAY REFLECTIVITY DATA

without protein
15 mN/m

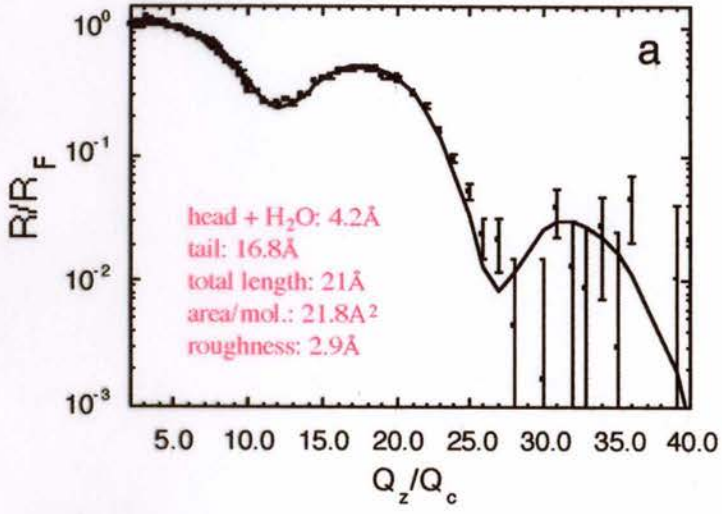

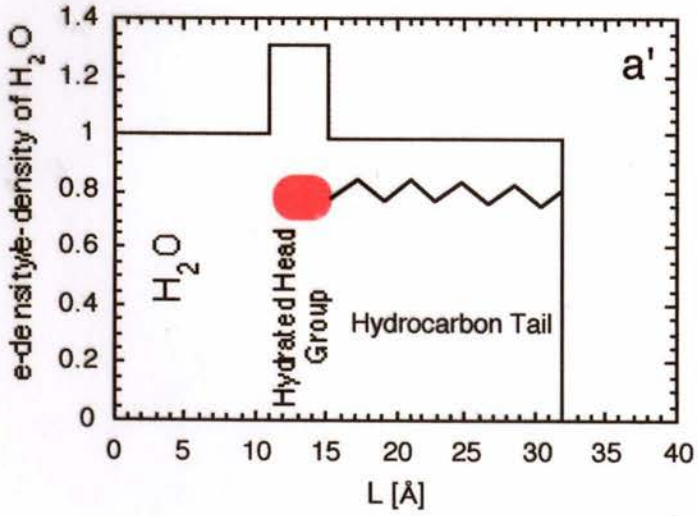

with protein
40 mN/m

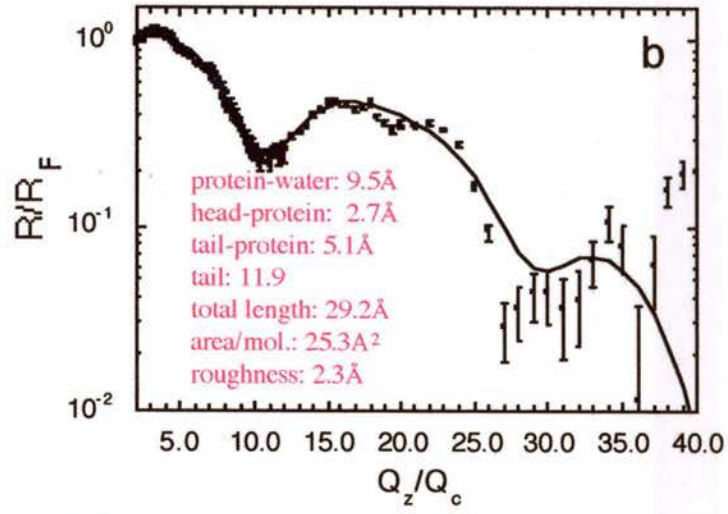

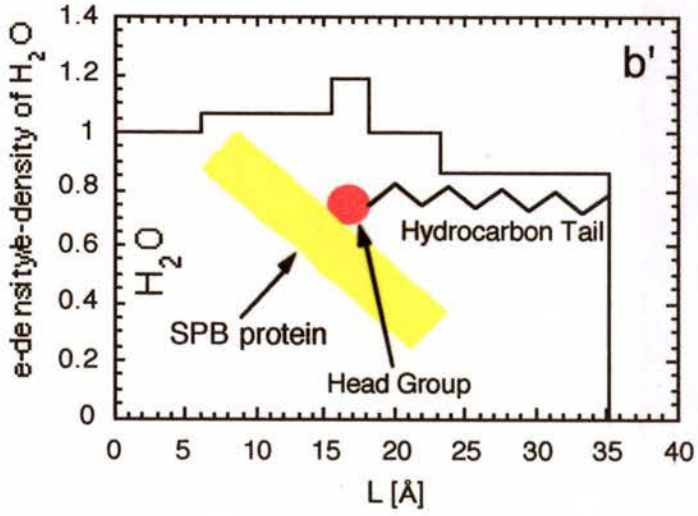

INSERTION OF SP-B$_{1-25}$ INTO LIPID MATRIX

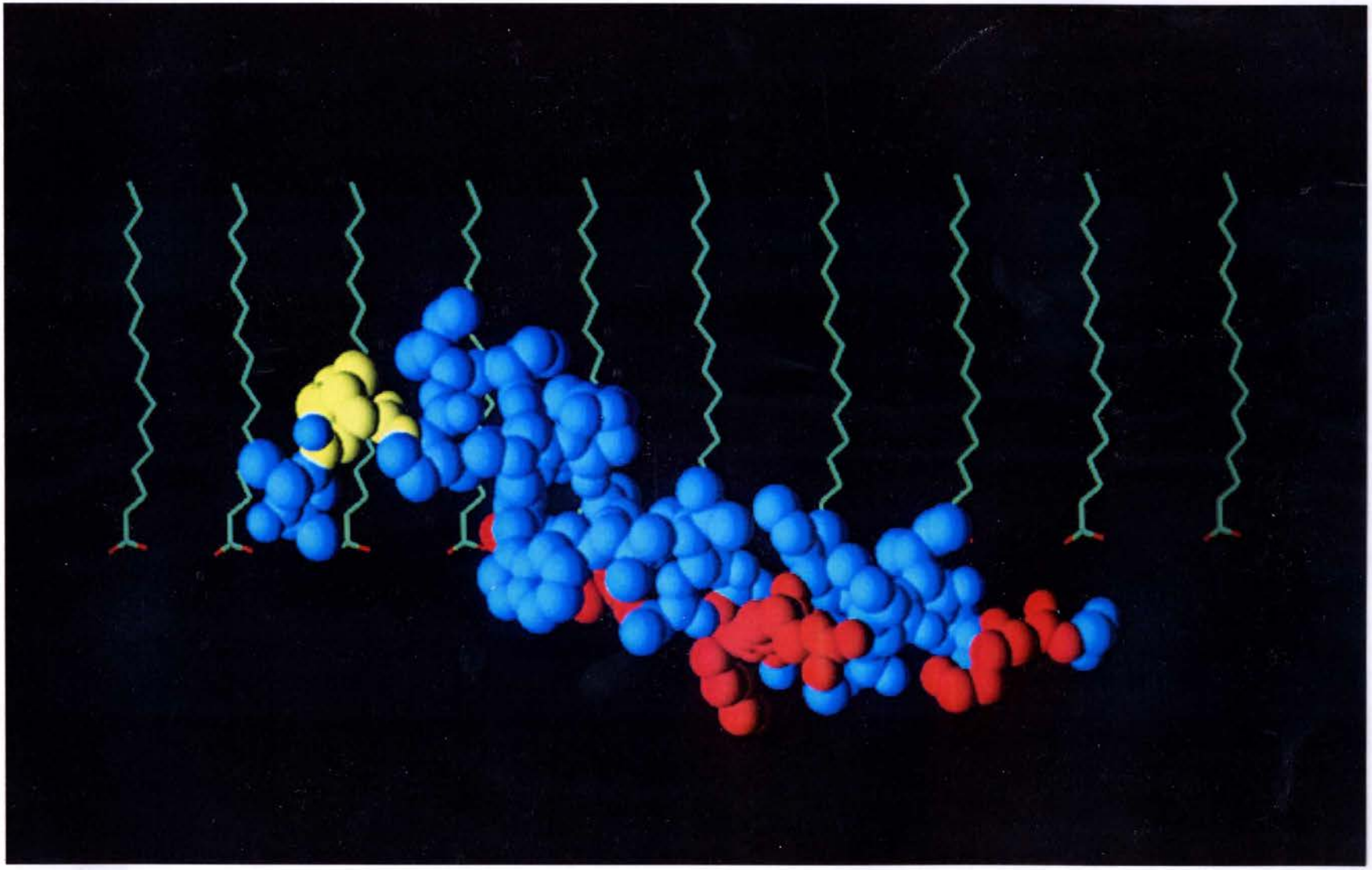

angle of insertion = 34 °relative to the interface

Biophys. J. 81 (2001) 572-585

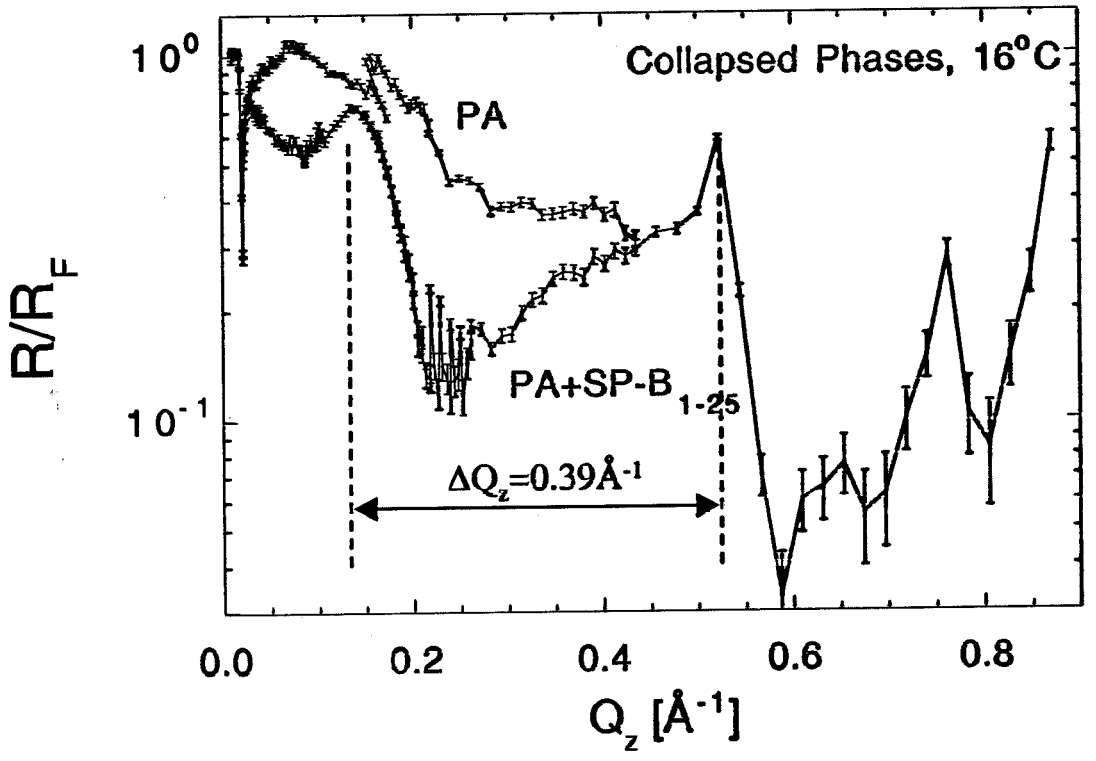

Fig. 15 (Ka Yee C. Lee et al.)

178 Next: DPPC/PA ~ 1 HD spacing

GIXD DATA ON PURE WATER

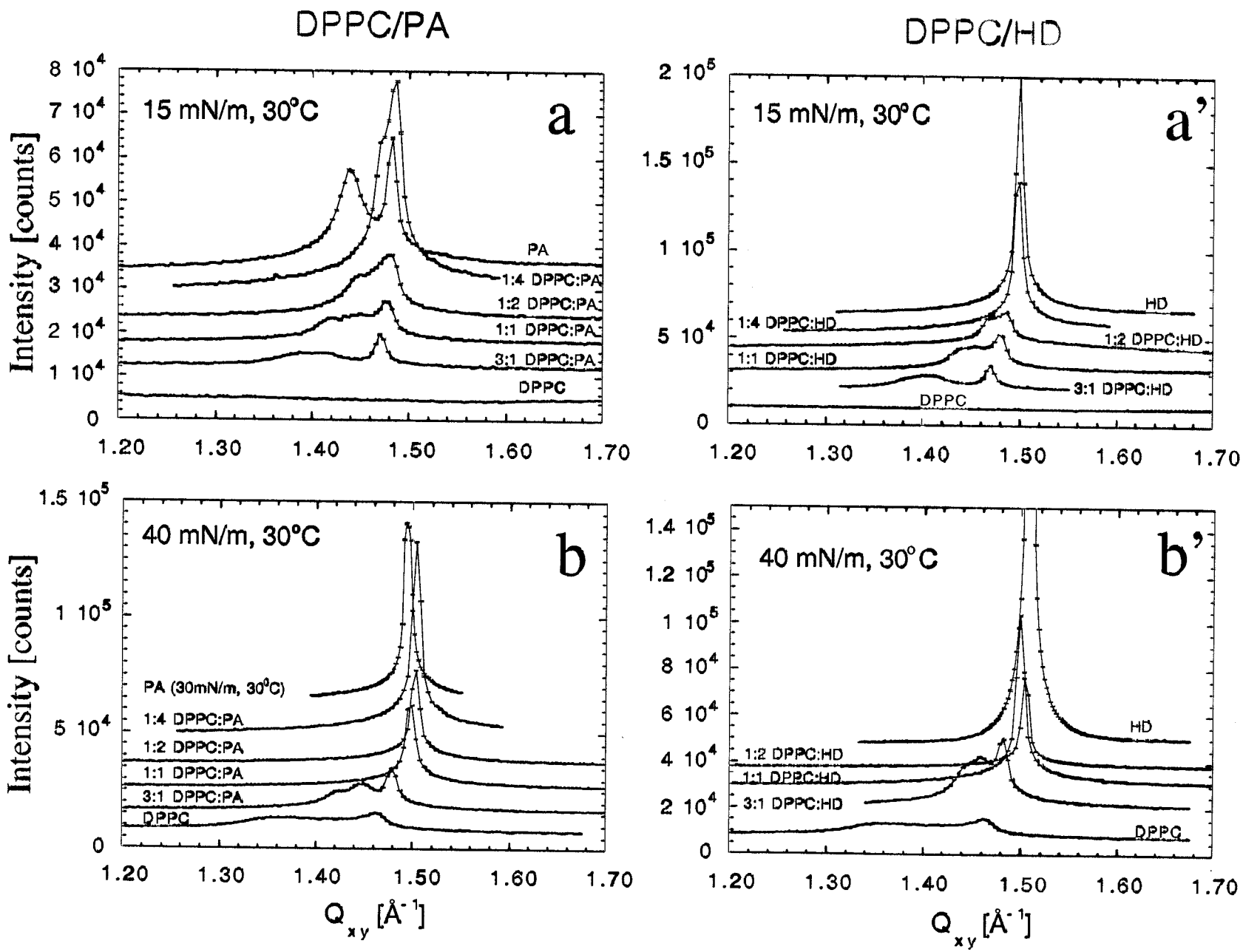

DPPC:PA MIXTURES at 15mN/m at 30°C														
	In-Plane Bragg Peaks												Out-of-Plane Bragg Rods	
Compo-sition	observed d-spacing (Å)			Area per chain ($Å^2$)	Projected area per chain ($Å^2$)	Unit cell (Å)	Coherence length, L (Å)						Tilt angle, *t* (degrees)	Tilt direction (degrees)
DPPC	No in-plane diffraction observed → no in-plane order													
PA	d_{11} 4.37	d_{02} 4.24		21.56	20.07	rectangular a=5.09, b=8.47	L_{11} 140	L_{02} 560					21.4°	13.2° from NN, non-symmetry
3:1 DPPC:PA	d_{11} 4.49	d_{02} 4.27		22.50	20.31	rectangular * a=5.27 b=8.54	L_{11} 66	L_{02} 540					25.5°	9.8° from NN, non-symmetry
1:1 DPPC:PA	d_{10} 4.22	d_{01} 4.35	d_{11} 4.26	21.79	20.19	oblique** a=5.01, b=4.93 γ=118.1°	L_{10} 95	L_{01} 250	L_{11} 200				22.1°	15.5° from NN, non-symmetry
1:2 DPPC:PA	d_{11} 4.35	d_{02} 4.26		21.53	20.32	rectangular a=5.06 b=8.51	L_{11} 105	L_{02} 200					19.3°	17.6° from NN, non-symmetry
1:4 DPPC:PA	d_{11} 4.26	d_{02} 4.23		20.85	19.70	rectangular a=4.93 b=8.47	L_{11} 150	L_{02} 440					19.1°	18.6° from NN, non-symmetry

* small oblique distortion

** very close to a rectangular cell: a = 5.10Å, b = 8.52Å.

DPPC:PA MIXTURES at 40mN/m at 30°C									
	In-Plane Bragg Peaks							Out-of-Plane Bragg Rods	
Compo-sition	Observed d-spacing (Å)			Area per chain ($Å^2$)	Projected area per chain ($Å^2$)	Unit cell (Å)	Coherence length, L (Å)			Tilt angle, *t* (degrees)	Tilt direction (degrees)
DPPC	d_{11} 4.57	d_{02} 4.31		23.27	21.00	rectangular* a=5.40, b=8.62	L_{11} 50	L_{02} 150		25.5°	13° from NN, non-symmetry
PA 25mN/m	d_{10} 4.20			20.37	20.28	hexagonal a_H=4.85	L_{10} 720			5.3°	NN
3:1 DPPC:PA	d_{10} 4.35	d_{01} 4.33	d_{11} 4.25	21.43	19.97	oblique a=4.95, b=4.93 γ=118.6°	L_{10} 70	L_{01} 160	L_{11} 700	21.3°	14.9° from NN, non-symmetry
1:1 DPPC:PA	d_{10} 4.19			20.28	20.22	hexagonal a_H=4.84	L_{10} 490			4.3°	NN
1:2 DPPC:PA	d_{10} 4.18			20.19	20.15	hexagonal a_H=4.83	L_{10} 560			3.8°	NN
1:4 DPPC:PA	d_{10} 4.18			20.19	20.13	hexagonal a_H=4.83	L_{10} 600			4.5°	NN

OPTIMAL PACKING AND POSSIBLE ARRANGEMENTS IN 2D

Data

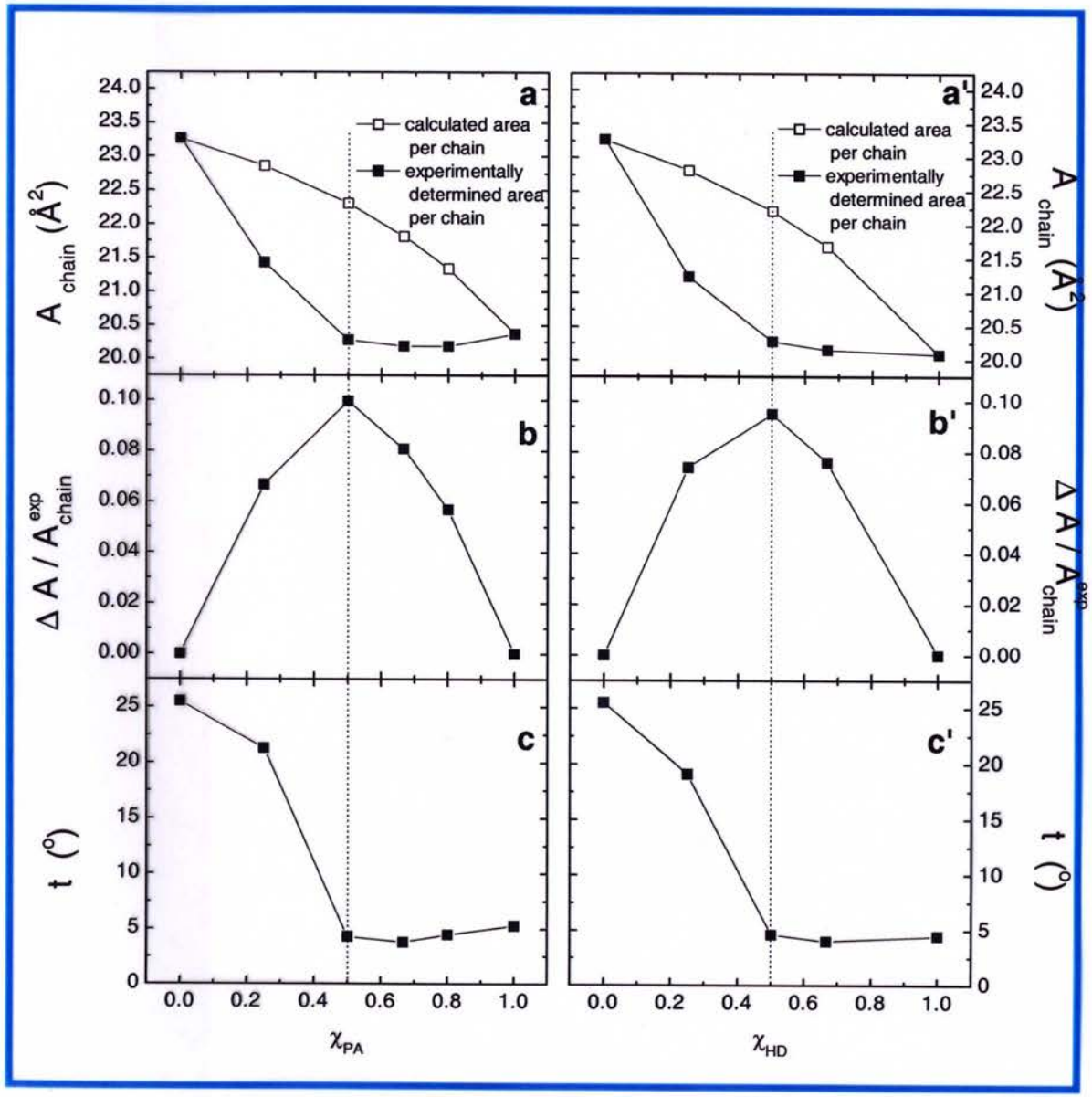

Model

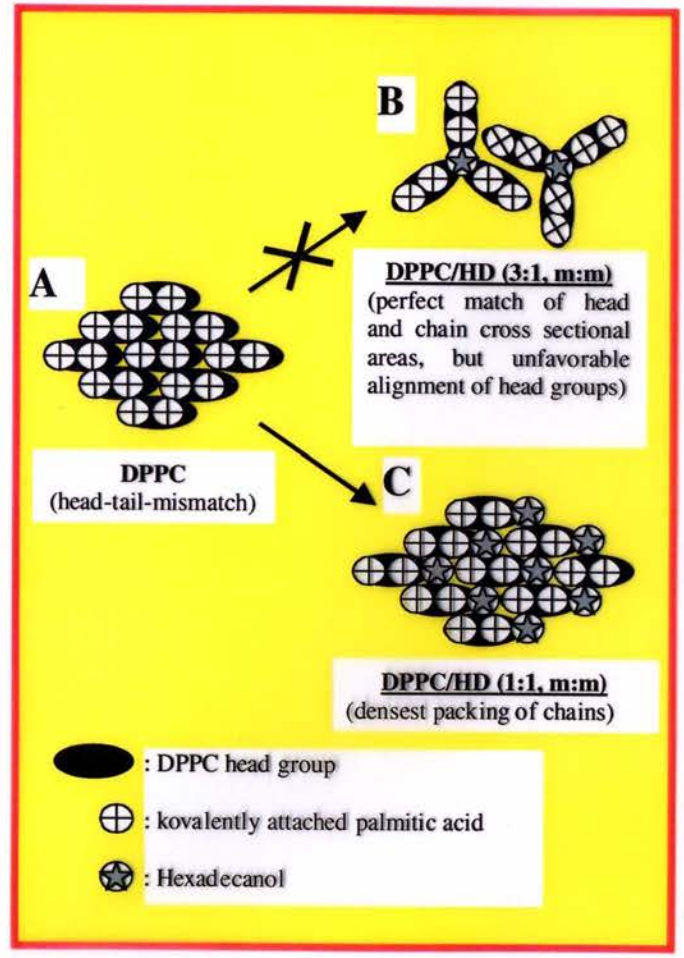

J. Chem. Phys., in press

Isotherm and Morphology at 25°C

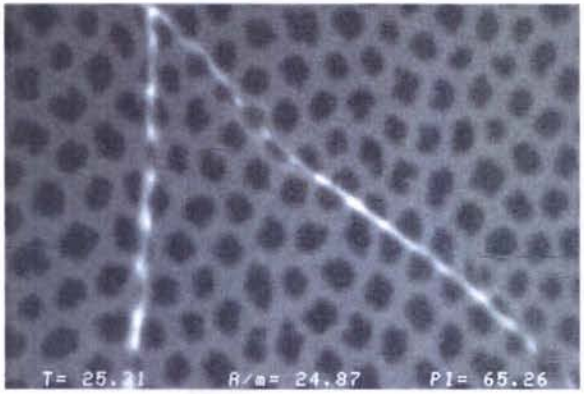

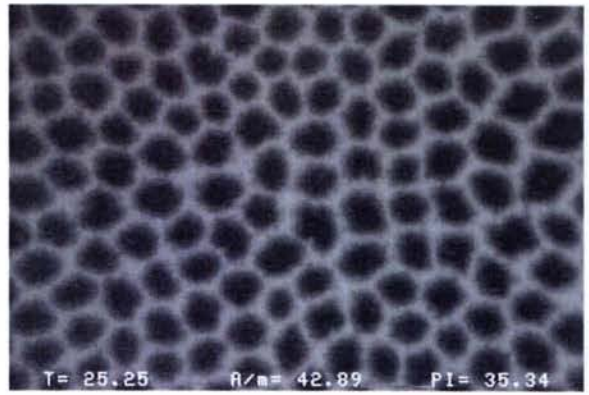

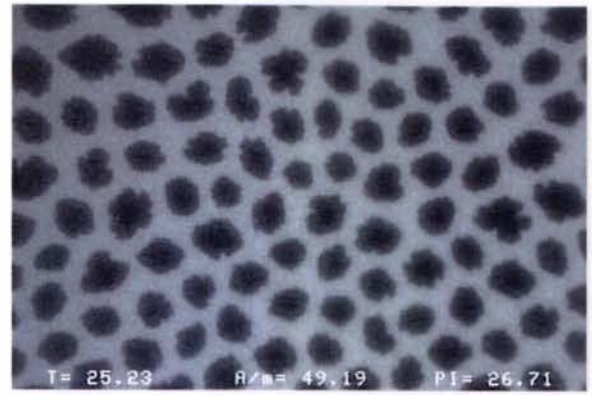

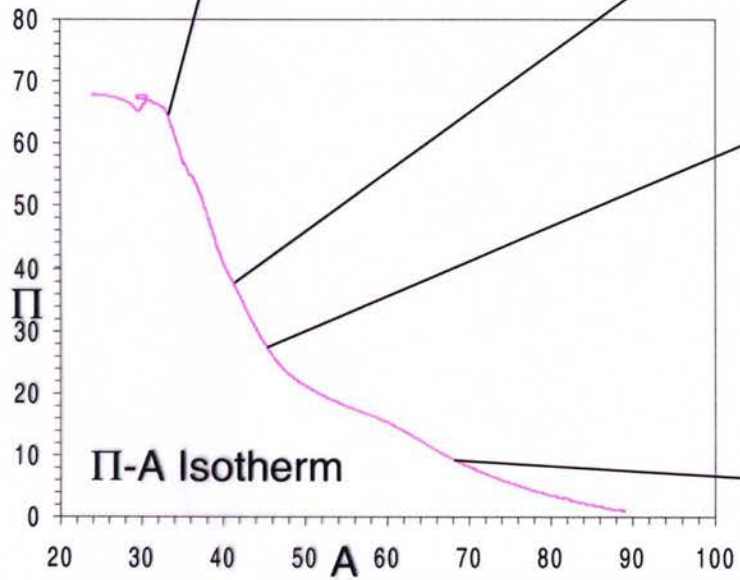

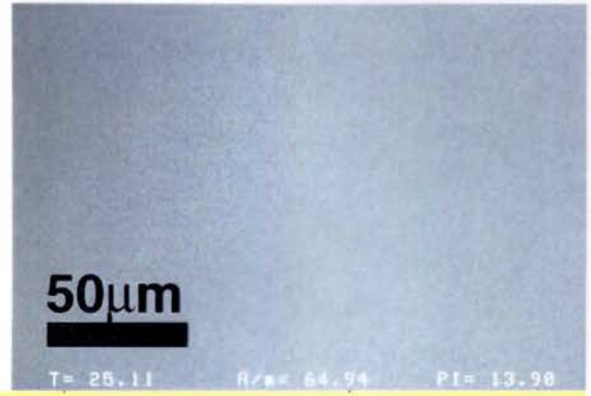

- Reversible Folded Structures coexist with the monolayer.

Isotherm and Morphology at 37°C

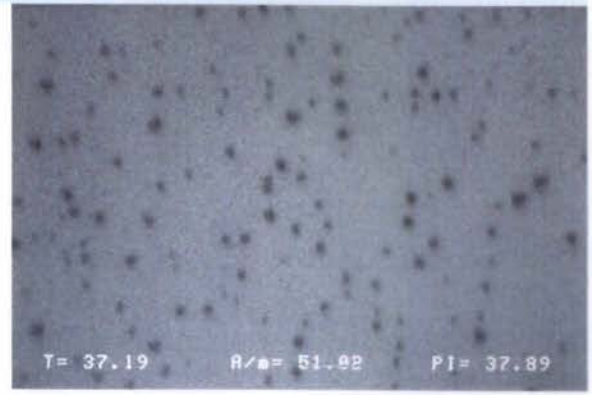

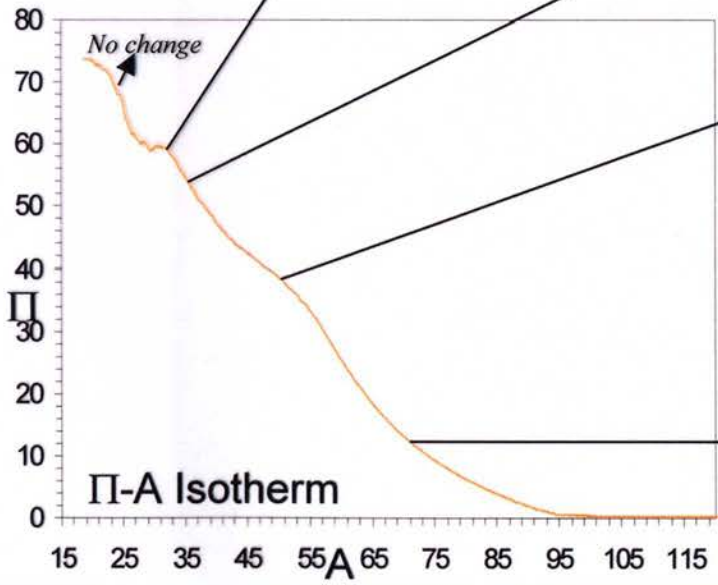

- Collapse is predominantly by formation of either surface bound tubular vesicles or unbound vesicles.

The monolayer is not biphasic at collapse.

Isotherms and Phase Diagram

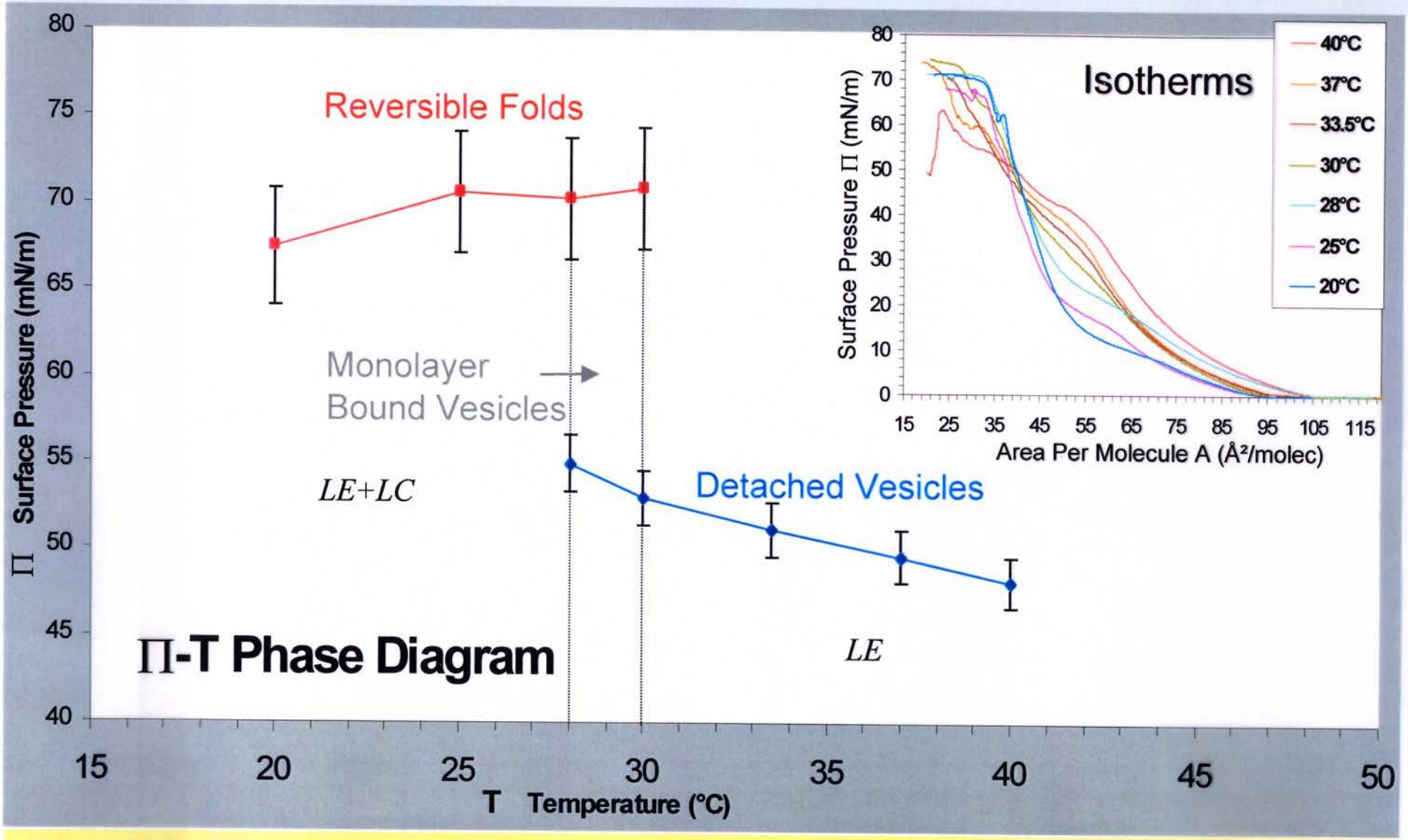

- T< 28°C collapse takes place primarily by large scale reversible folding.
- T =28°, 30°C bimodal collapse with both vesiculation and folding observed.
- T ≥ 33.5°C monolayer is monophasic and only vesiculation is observed.

Temperature Jump Experiment

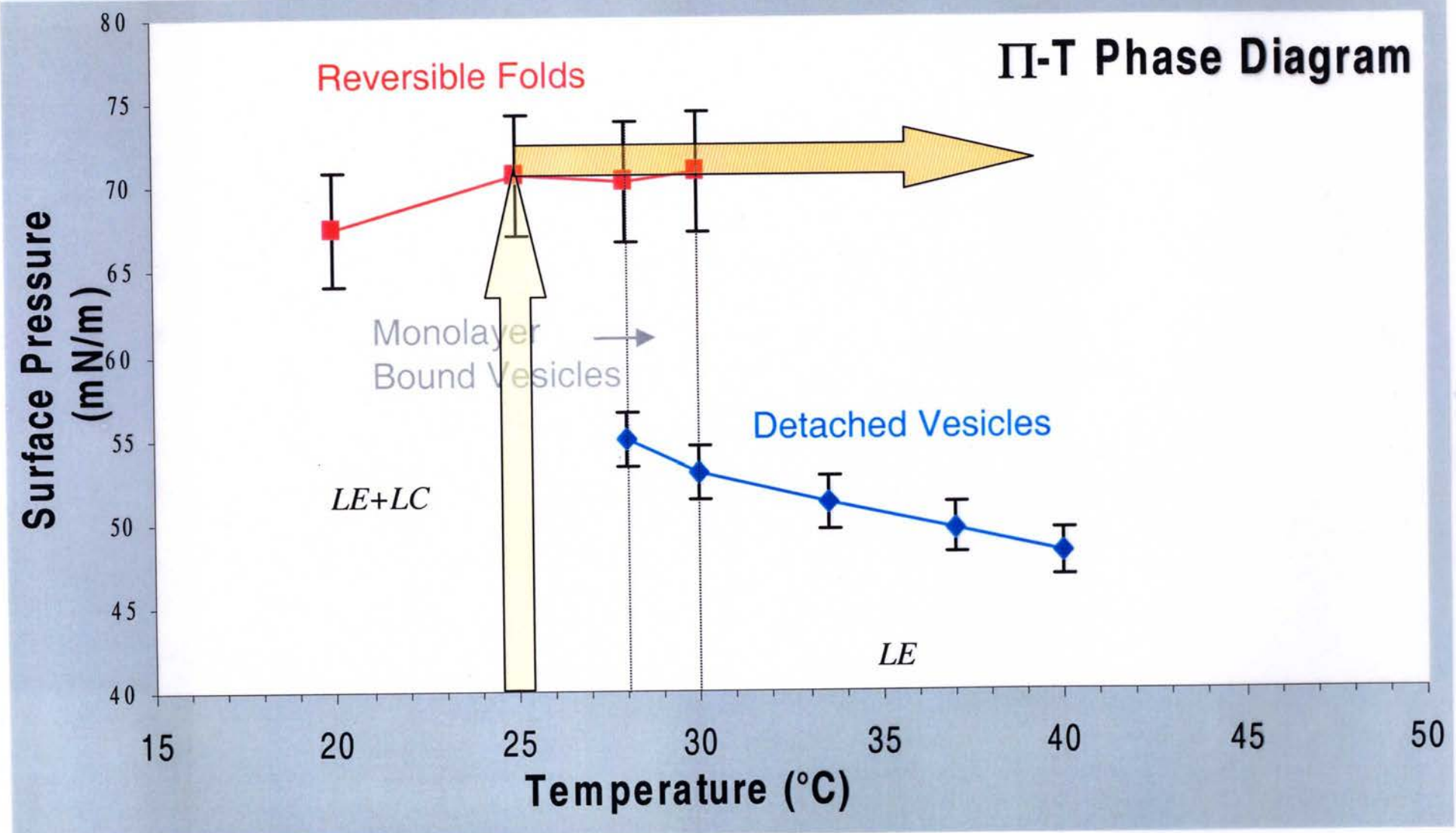

1. Compress the monolayer at a low temperature up to the folding point
2. Heat the subphase and watch the changes in phase and morphology

- To verify the existence of the Fold to Vesicle Boundary and Transition

Temperature Jump Morphology

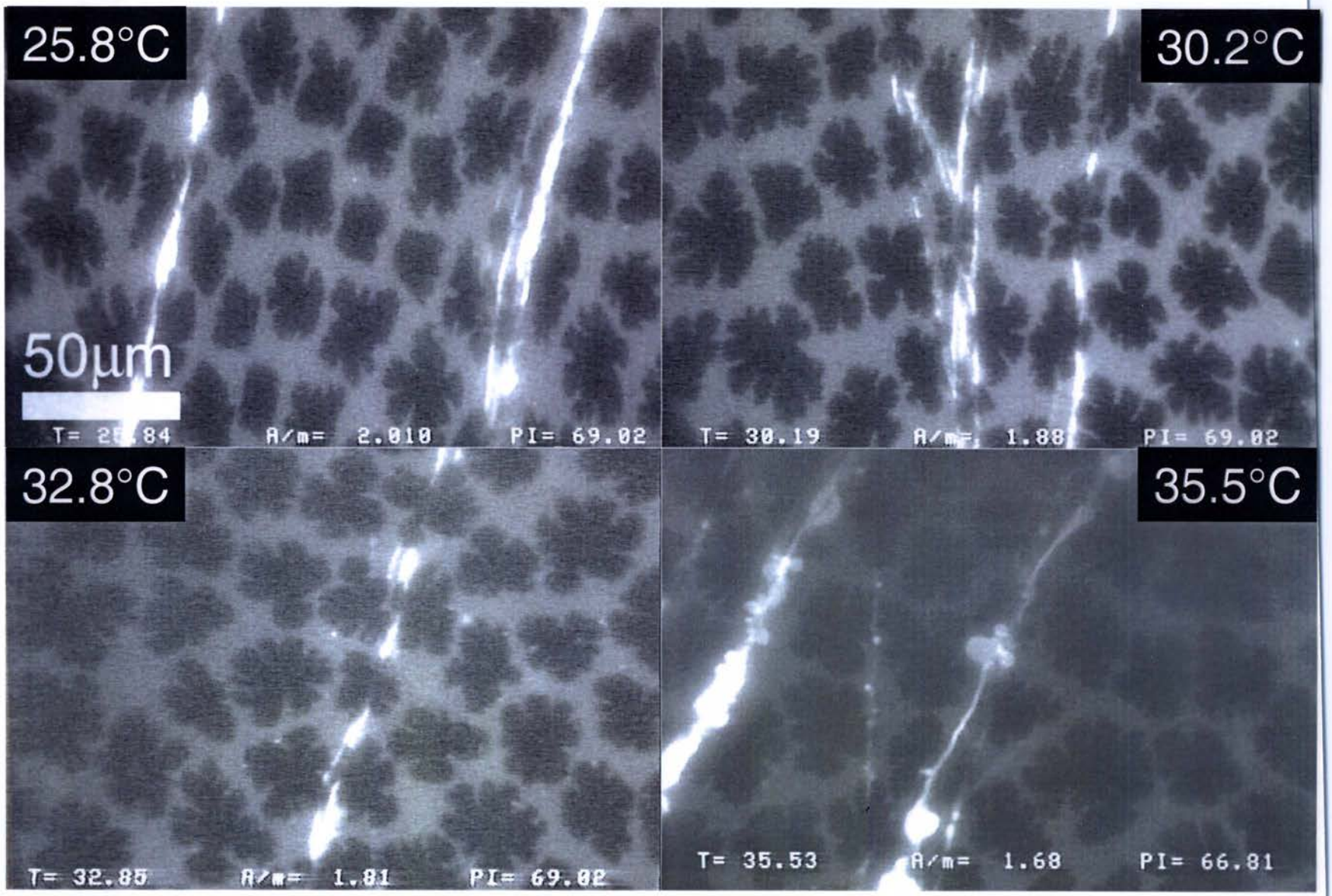

J. Phys. Chem. B (2001) in press











Model

- domain size $L \simeq 10\ \mu$m
- domain boundary width $\xi \simeq 1$ nm
- elastic length $\lambda = (K/\gamma)^{1/2} \simeq 1$–$10$ nm
- spontaneous radius of curvature $c_0^{-1} \simeq 1$–10 nm.

$\Rightarrow$ We focus on the vicinity of an isolated straight boundary.

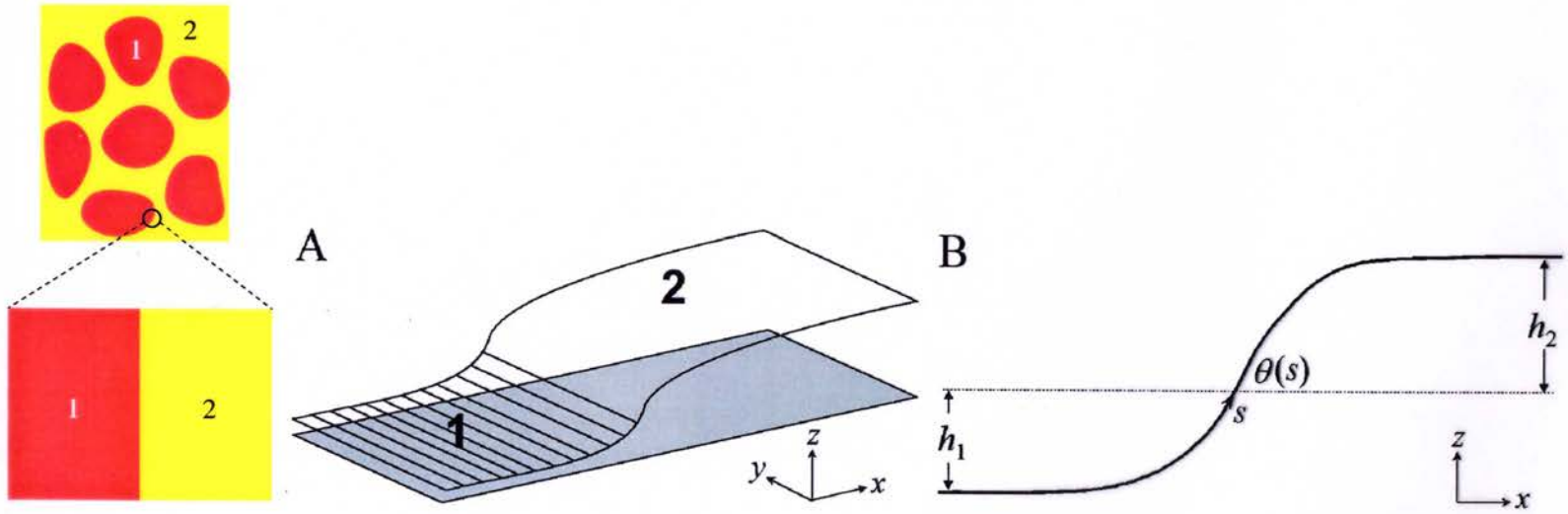

$$G = \int_A \mathrm{d}A \left(\frac{1}{2}Kc^2 - Kc_0c\right) + \gamma \int_A \mathrm{d}(A - A_\mathrm{p}) + \tau \int_R \mathrm{d}(R - y)$$

$$g \equiv G/L = \int_{-\infty}^{\infty} \mathrm{d}s \left[\frac{1}{2}K\dot{\theta}^2 - Kc_0\dot{\theta} + \gamma(1 - \cos\theta)\right]$$